

# Simultaneous laser cooling of multiple atomic species using a frequency comb

---

**Buhin, Danijel**

**Doctoral thesis / Disertacija**

**2022**

*Degree Grantor / Ustanova koja je dodijelila akademski / stručni stupanj:* **University of Zagreb, Faculty of Science / Sveučilište u Zagrebu, Prirodoslovno-matematički fakultet**

*Permanent link / Trajna poveznica:* <https://urn.nsk.hr/urn:nbn:hr:217:069742>

*Rights / Prava:* [In copyright](#) / [Zaštićeno autorskim pravom.](#)

*Download date / Datum preuzimanja:* **2024-04-16**



*Repository / Repozitorij:*

[Repository of the Faculty of Science - University of Zagreb](#)





University of Zagreb  
Faculty of Science  
Department of Physics

Danijel Buhin

# **SIMULTANEOUS LASER COOLING OF MULTIPLE ATOMIC SPECIES USING A FREQUENCY COMB**

DOCTORAL DISSERTATION

Zagreb, 2022



University of Zagreb  
Faculty of Science  
Department of Physics

Danijel Buhin

# **SIMULTANEOUS LASER COOLING OF MULTIPLE ATOMIC SPECIES USING A FREQUENCY COMB**

DOCTORAL DISSERTATION

Supervisor:  
dr. sc. Damir Aumiler

Zagreb, 2022



Sveučilište u Zagrebu  
Prirodoslovno-matematički fakultet  
Fizički odsjek

Danijel Buhin

**ISTOVREMENO LASERSKO HLAĐENJE  
VIŠE VRSTA ATOMA FREKVENTNIM  
ČEŠLJEM**

DOKTORSKI RAD

Mentor:  
doc. dr. sc. Damir Aumiler

Zagreb, 2022

# **Supervisor information**

Doc. dr. sc. Damir Aumiler was born in Zagreb, Croatia on the 28th of March 1977. He graduated from the Faculty of Science in Zagreb in 2002. with a Master's thesis titled "The influence of perturbations on the structure of atomic and molecular transitions in rubidium vapor". He received his PhD in physics in 2006. with the doctoral thesis titled "Resonant interaction of atoms and molecules with the femtosecond laser frequency comb". He is currently employed at the Institute of Physics as a senior scientist. His main scientific interests are in experimental and theoretical studies of the interaction of atoms with an optical frequency comb. Currently, he is the head of the Center for advanced laser techniques.

# Acknowledgements

First I would like to thank doc. dr. sc. Damir Aumiler for being such a great and inspiring supervisor, for his determination and unprecedented knowledge. You made my job and research possible, and you motivate me and everyone around.

I am very grateful to have a wonderful supervisor like Damir, but it is hard to find words for how lucky I am to have dr. sc. Ticijana Ban as my co-advisor. Your will and determination, to push even harder when it is the hardest made everything look easy.

I would like to thank dr. sc. Neven Šantić who was a great colleague from the beginning of my work at the Institute and an even better supervisor at the end. To dr. sc. Ivor Krešić I'd like to thank you for many funny and happy hours we spent together.

Many thanks go to my colleagues, I am very happy to have you all around me. To Domagoj Kovačić, with whom I shared many many lab hours, from early in the morning, until late in the night, to Mateo Kruljac, for his composure and measured panic at moments, to Vjekoslav Vulić, who stayed with me during the hardest period, to Ivana Puljić, who entertained us all with her comments, and last but not least I would like to thank Ana Cipriš, who was a very good friend at every conference we attended together and for your support. Here I would like to thank Marin Đujić for your short but productive stint during your Master's.

I am very grateful to dr. sc. Thomas Udem and dr. sc. Alexey Grinin from whom I learned a great deal during my stay in Garching.

I am indebted to dr. sc. Nataša Vujičić and dr. sc. Silvije Vdović for lending me ever-missing equipment and always giving great bits of advice. I would like to thank Damir Altus, who shared a lot of his time and knowledge to give me short lectures about electronics. To Ivan and Franjo from the mechanical workshop, I owe many many thanks for making all of the parts.

I would like to thank my parents and friends for your support which means a lot to me.

And last, but not least I would like to thank Patricija Okić. You are the love of my life and you make everything perfect. Support you gave me over the last few years I can only hope to give you back. There are no words for how much you mean to me and how happy I am to have you in my life. I am excited to share my life with you and with our son Alexander.

# Abstract

I present the results of the theoretical calculation of the interaction of two counter-propagating pulse trains with six-level atoms. In the model, we calculate the radiation pressure force and the diffusion coefficient exerted on the atoms. The temperature of atoms is calculated using a Fokker-Planck equation. I present how frequency comb (FC) parameters affect the process of laser cooling. Results of the calculation suggest that the laser cooling with an FC is most effective when the single comb mode is red detuned from the cooling transition, and another comb mode is near-resonant with repumping transition in an atom.

I report on the experimental demonstration of the simultaneous cooling of two atomic species using a single frequency comb source in 1D. The repetition frequency is tuned so the comb modes are red detuned from cooling transitions of  $^{85}\text{Rb}$  and  $^{87}\text{Rb}$  atoms simultaneously. We generated dual-species MOT using standard cw laser cooling techniques and then in an additional cooling phase demonstrated simultaneous cooling with an FC.

Finally, I present the results of the electromagnetically induced transparency (EIT) and quantum memory (QM) measurements in  $^{85}\text{Rb}$  vapor. In the experiment, we used three different glass cells with different coatings and buffer gas filling. We measured the ground state decoherence rate for these three cells by measuring the width of the EIT resonance. Decoherence rate affects the properties of the QM storage time and efficiency. The best-achieved efficiency is 20.5 % and the longest achieved storage time is 1.2 ms.

Keywords: laser cooling, frequency comb, Doppler temperature, dual-species MOT, EIT, quantum memories, ground state decoherence

# Prošireni sažetak

U ovom radu predstavljam rezultate istraživanja napravljenih na Institutu za fiziku u Zagrebu pod mentorstvom doc. dr. sc. Damira Aumilera. Tijekom mog istraživanja, bio sam član Grupe za kvantne tehnologije na institutu. Tijekom prve godine rada sudjelovao sam na projektu "Optomehanika uzrokovana frekventnim češljem" voditeljice dr. sc. Ticijane Ban. Glavni dio istraživanja napravljen je u sklopu projekta Hlađenje atoma frekventnim češljem voditelja dr. Damira Aumilera. Zadnji dio istraživanja bio je dio bilateralnog Hrvatsko-Slovenskog projekta "Razvoj gradivnih blokova za novu europsku kvantnu komunikacijsku mrežu", gdje je voditelj hrvatske strane dr. sc. Mario Stipčević s Instituta Ruđer Bošković u Zagrebu.

Glavna tema mog doktorskog rada je simultano hlađenje dvije vrste rubidijevih izotopa pomoću frekventnog češlja. Druga tema je teorijski račun interakcije atoma i frekventnog češlja te hlađenje atoma s frekventnim češljem. Rezultati teorijskog modela potkrepljuju rezultate eksperimenta i daju uvid za izgradnju budućih eksperimenata. Zadnja predstavljena tema vezana je uz efekt elektromagnetski inducirane transparencije (EIT) i realizacija kvantne memorije bazirane na EIT efektu.

Doktorski rad je organiziran na način prikazan kroz sljedećih nekoliko odlomaka.

U prvom poglavlju predstavljeno je područje istraživanja iz obje tematike predstavljene u doktorskom radu.

U drugom poglavlju ukratko je objašnjeno lasersko hlađenje i zarobljavanje atoma kao uvod u područje istraživanja predstavljeno u radu. Ukratko je objašnjen princip rada frekventnog češlja te njegov doprinos u eksperimentima laserskog hlađenja.

U trećem poglavlju predstavljen je teorijski model interakcije frekventnog češlja s atomima sa šest energijskih razina. Atomi interagiraju s dvije suprotno propagirajuće zrake frekventnog češlja. U modelu se rješavaju optičke Blochove jednadžbe koje opisuju vremensku evoluciju elemenata matrice gustoće. Iz stacionarnog rješenja optičkih Blochovih jednadžbi računamo radijativnu silu kojom zrake frekventnog češlja utječu na atome te koeficijent difuzije. Također, računamo temperaturu atoma u stacionarnom stanju pomoću Fokker-Planck jednadžbe. U modelu proučavamo kako parametri frekventnog češlja, frekvencija repeticije i frekventni pomak

češlja, utječu na dinamiku hlađenja atoma. Predstavljani su rezultati tri različita skupa parametara frekventnog češlja te je objašnjeno kako utječu na lasersko hlađenje. Iz teorijskog računa proizlazi kako je hlađenje s frekventnim češljem efikasno u slučaju kada je frekvencija  $n$ -tog moda frekventnog češlja crveno pomaknuta u odnosu na frekvenciju prijelaza za hlađenje, dok je neki drugi mod frekventnog češlja blizu rezonancije prijelaza za naseljavanje. Temperature su bliske Dopplerovoj temperaturi, kao što je očekivano u hlađenju s laserima kontinuirane emisije.

U četvrtom poglavlju je opisan eksperimentalni postav potreban za realizaciju simultanog hlađenja dvije vrste atoma s frekventnim češljem. Opisan je proces stvaranja hladnog oblaka dva izotopa atoma rubidija istovremeno. Kako bi frekventni češalj istovremeno mogao međudjelovati s atomima oba izotopa, potrebno je ugoditi njegovu frekvenciju repeticije na 80.495 MHz. Predstavljani su rezultati mjerenja simultane radijativne sile frekventnog češlja, koji su uspoređeni s teorijskim predviđanjem. Radijativna sila izračunata je iz mjerenja pomaka centra mase oblaka nakon određenog vremena interakcije. Teorijsko predviđanje kvalitativno opisuje izmjerenu silu, no postoje male kvantitativne razlike za koje je opisan razlog nastajanja. Konačno, prikazani su rezultati istovremenog hlađenja dvije vrste atoma s frekventnim češljem. Frekventni češalj međudjeluje s dvije vrste atoma u jednoj dimenziji, s  $\sigma^+\sigma^-$  polariziranim zrakama. Temperatura je određena tehnikom mjerenja vremena proleta. Izmjerene temperature slažu se s teorijskim predviđanjem te je minimalna izmjerena temperatura bliska Dopplerovoj temperaturi.

U petom poglavlju predstavljeno je istraživanje efekta elektromagnetski inducirane transparencije (EIT) te realizacija kvantne memorije bazirane na EIT efektu. Ukratko je predstavljena teorijska pozadina efekta te je objašnjen eksperimentalni postav. Istraživanje je temeljeno na proučavanju efekta dekoherencije osnovnog stanja te njegovom utjecaju na svojstva kvantne memorije. Koristili smo tri različite kivete s atomima  $^{85}\text{Rb}$  koje imaju različite premaze i punjenja plemenitim plinom. Ti premazi i punjenja smanjuju dekoherenciju koja negativno utječe na svojstva kvantne memorije. Za kivetu s najmanjom dekoherencijom izmjerena je najveća efikasnost kvantne memorije i najdulje vrijeme pohranjivanja pulseva u mediju.

U posljednjem poglavlju izloženi su glavni rezultati predstavljeni u doktorskom radu te je dan uvid u buduća istraživanja koja su bazirana na rezultatima prikazanim u ovom radu.

Ključne riječi: lasersko hlađenje, frekventni češalj, Dopplerova temperatura, magneto-optička stupica s dvije vrste atoma, elektromagnetski inducirana transparentnost, kvantne memorije, dekoherencija osnovnog stanja

# Table of contents

<b>1</b>	<b>Introduction</b>	<b>1</b>
1.1	Laser cooling and trapping . . . . .	1
1.2	Quantum memories . . . . .	3
1.3	Thesis outline . . . . .	4
<b>2</b>	<b>Laser cooling a with frequency comb</b>	<b>6</b>
2.1	Atom-light interaction . . . . .	6
2.1.1	Optical Bloch equations for two-level atom . . . . .	6
2.1.2	Light forces . . . . .	10
2.2	Laser cooling and trapping . . . . .	12
2.2.1	Doppler cooling . . . . .	13
2.2.2	Magneto-optical trap . . . . .	15
2.3	Frequency comb laser cooling . . . . .	18
2.3.1	Generation of ultrashort laser pulses . . . . .	18
2.3.2	Frequency comb cooling . . . . .	21
<b>3</b>	<b>Theoretical study of Doppler cooling with a FC</b>	<b>26</b>
3.1	Comb-atom interaction . . . . .	26
3.1.1	The influence of comb parameters on FC laser cooling . . . . .	28
3.2	Density matrix evolution . . . . .	31
3.3	Force and diffusion . . . . .	35
3.4	FC laser cooling . . . . .	39
3.5	Conclusion . . . . .	44
<b>4</b>	<b>Simultaneous dual-species laser cooling using an optical frequency comb</b>	<b>47</b>
4.1	FC laser cooling experiments . . . . .	48
4.2	Rubidium atom . . . . .	50
4.3	Experimental setup . . . . .	53
4.3.1	Laser system . . . . .	53
4.3.2	Frequency comb . . . . .	55
4.3.3	Magneto-optical trap . . . . .	57
4.3.4	Optics setup for laser cooling and trapping . . . . .	59
4.4	Dual MOT generation . . . . .	62
4.4.1	Imaging of cold clouds and temperature measurement . . . . .	63

4.4.2	Experiment control . . . . .	66
4.4.3	Experimental protocol . . . . .	67
4.5	FC radiation pressure force . . . . .	70
4.6	Simultaneous cooling with an FC . . . . .	75
4.7	Conclusion . . . . .	79
<b>5</b>	<b>EIT quantum memories with rubidium vapor</b>	<b>80</b>
5.1	Theory of EIT and QM . . . . .	80
5.1.1	Electromagnetically induced transparency . . . . .	81
5.1.2	Slow light and quantum memories . . . . .	84
5.2	Experimental setup . . . . .	86
5.2.1	Filtering cavity . . . . .	90
5.2.2	Rubidium glass cells . . . . .	91
5.2.3	Glass cell heater . . . . .	93
5.3	Decoherence measurement . . . . .	95
5.4	QM storage time and efficiency . . . . .	101
5.5	Conclusion . . . . .	106
<b>6</b>	<b>Thesis summary</b>	<b>108</b>
	<b>References</b>	<b>110</b>
	<b>Curriculum vitae</b>	<b>114</b>

# List of Figures

1.1	Table of laser cooled atomic species. . . . .	2
2.1	Radiation pressure force dependence on the laser detuning and intensity. . . . .	12
2.2	Radiation pressure force for a two-level atom . . . . .	14
2.3	Rubidium atoms Doppler temperature as a function of laser detuning . . . . .	15
2.4	Principle of the magneto-optical trap . . . . .	16
2.5	Principle of ultrashort pulse generation. . . . .	19
2.6	A pulse train of a mode-locked laser and the frequency comb spectrum . . . . .	21
2.7	Two principles of frequency comb laser cooling . . . . .	23
2.8	An example of the time evolution of the excited state population. . . . .	24
2.9	An example of the radiation pressure force from two counter-propagating pulse trains. . . . .	25
3.1	Relative positions of the comb modes with respect to the atomic transitions in $^{87}\text{Rb}$ for three sets of FC parameters. . . . .	29
3.2	Temporal evolution of the density matrix elements in four steps. . . . .	31
3.3	Transient temporal evolution of the excited state populations. . . . .	33
3.4	Effect of the pulse delay on the temporal evolution of the density matrix elements. . . . .	33
3.5	Stationary state populations of the ground and excited state . . . . .	34
3.6	Radiation pressure force for three sets of comb parameters. . . . .	36
3.7	Diffusion coefficient as a function of atomic velocity for three different sets of comb parameters. . . . .	37
3.8	Examples of atomic velocity distributions for two different temperatures. . . . .	40
3.9	Time evolution of the atomic velocity distribution under the influence of FC beams. . . . .	41
3.10	The temperature of atoms as a function of detuning of the $n$ -th comb mode from the cooling transition. . . . .	43
4.1	$^{85}\text{Rb}$ and $^{87}\text{Rb}$ hyperfine energy level structure. . . . .	51
4.2	Setup for injection locking . . . . .	53
4.3	Frequency comb laser . . . . .	55
4.4	Frequency comb spectrum . . . . .	56
4.5	Frequency comb stabilization scheme . . . . .	57
4.6	Photograph of a vacuum chamber with gradient coils and optics. . . . .	58

4.7	Schematic experimental setup for the dual species MOT and FC laser cooling .	60
4.8	Schematic setup of the optics around vacuum chamber for dual-species cooling	61
4.9	Simultaneous loading of two Rb isotopes MOT . . . . .	63
4.10	Images of the cloud expansion and 2D Gaussian fit images . . . . .	65
4.11	Width of the atomic spatial distribution as a function of free expansion time. . .	66
4.12	Temperature stability measurement for both Rb isotopes . . . . .	66
4.13	Window of the self-written program for experiment control . . . . .	68
4.14	Experimental protocol of measurement. . . . .	69
4.15	Scheme of the frequency comb modes with respect to $^{85}\text{Rb}$ and $^{87}\text{Rb}$ atomic transitions. . . . .	70
4.16	Displacement of the clouds center of mass due to the FC beam interaction. . . .	72
4.17	FC radiation pressure force exerted on atoms of both Rb isotopes simultaneously	73
4.18	Fluorescence images of cold clouds of $^{85}\text{Rb}$ and $^{87}\text{Rb}$ isotopes when laser cooled with an FC in 1D. . . . .	76
4.19	Simultaneously measured temperatures of cold atoms as a function of FC detuning. . . . .	77
4.20	Simultaneous temperatures of cold clouds as a function of the FC interaction time.	78
5.1	Energy level structure for a three-level atom. . . . .	81
5.2	Absorption of the probe beam and refractive index in the EIT conditions. . . . .	83
5.3	Saturation spectroscopy signal for $^{85}\text{Rb}$ $D_1$ transition. . . . .	87
5.4	Schematic setup for EIT and QM experiment and schematic energy level diagram.	88
5.5	Photograph of the experimental setup for EIT and QM . . . . .	89
5.6	Photograph of the setup for filtering cavity . . . . .	90
5.7	Side of resonance cavity locking principle . . . . .	91
5.8	Cavity transmission signal. . . . .	92
5.9	Home-built glass cell heater without magnetic component. . . . .	94
5.10	EIT transmission signal and the calculated EIT absorption signal . . . . .	95
5.11	Ground state decoherence rate as function of beam angle. . . . .	97
5.12	EIT lineshapes for cells with different coatings and fillings. . . . .	98
5.13	EIT linewidth and contrast as functions of control beam intensity. . . . .	99
5.14	Ground state decoherence of the EIT signals dependence on the beams angle. .	100
5.15	Measurement protocol for QM experiment. . . . .	101
5.16	Maximum measured QM efficiency . . . . .	102
5.17	QM efficiency as a function of storage time for different glass cells. . . . .	103
5.18	QM parameters for different input pulses. . . . .	105
5.19	QM efficiency for offresonant excitation . . . . .	106

# Chapter 1

## Introduction

In the thesis, I present the results of my work at the Institute of Physics in Zagreb, under the supervision of doc. dr. sc. Damir Aumiler. During my doctoral studies, I have been a member of the Quantum technologies group at the institute. In the first year of my study, work was done as a part of the "Frequency-Comb-induced OptoMechanics" project led by dr. sc. Ticijana Ban. The main part of my study was done as a part of the "Frequency comb cooling of atoms" project led by Damir Aumiler. The last part of my work at the institute was done as a part of the Croatian-Slovenian bilateral project "Development of building blocks for new European quantum communication network", with the Croatian side PI dr. sc. Mario Stipčević from Ruđer Bošković Institute in Zagreb.

The main topic of the thesis is the simultaneous cooling of two Rb isotopes using a single frequency comb laser source. The second topic of the thesis is the theoretical calculation of the comb-atom interaction and cooling. Results of this model, corroborate the experimental results and give insights for new experiments. The topic presented in the last part of the thesis is the electromagnetically induced transparency effect on the realization of the quantum memory based on the EIT.

### 1.1 Laser cooling and trapping

After the advent of the laser in 1960. based on the work by Townes and Schawlow [1], laser cooling and trapping is one of the most revolutionary discoveries in the field of atomic and optical physics. After the discovery of the laser cooling techniques in the 1980s, the field opened up to a broad spectrum of research, from the atom interferometry [2], optical atomic clocks [3], cold chemistry [4], quantum simulators [5] and many other.

Still, laser cooling is very limited to only a few atomic and ionic species [6] and are pre-

sented in Fig. 1.1. The main limitations of the laser cooling techniques are either due to the complexity of the energy level structure or the unavailability of the laser light to excite the cooling transitions. Most essential atomic species that have not yet been laser-cooled are hydrogen, carbon, nitrogen, and oxygen. Generation of the cold atomic samples of these species would bring a new revolution in the field. Laser cooling of hydrogen atoms would lead to new fundamental research, research on the interactions between atoms, and many others. Simultaneous cooling of these atoms could bring new insight to the field of organic chemistry since these atoms are most abundant in nature.

Periodic table of elements showing laser-cooled species (blue boxes):

- Hydrogen (1)**, **Helium (2)**
- Lithium (3)**, **Beryllium (4)**
- Sodium (11)**, **Magnesium (12)**
- Potassium (19)**, **Calcium (20)**
- Rubidium (37)**, **Strontium (38)**
- Cesium (55)**, **Barium (56)**
- Francium (87)**, **Radium (88)**
- Lanthanide series (57-70)**: Lanthanum (57), Cerium (58), Praseodymium (59), Neodymium (60), Promethium (61), Samarium (62), Europium (63), Gadolinium (64), Terbium (65), Dysprosium (66), Holmium (67), Erbium (68), Thulium (69), Ytterbium (70)
- Actinide series (89-102)**: Actinium (89), Thorium (90), Protactinium (91), Uranium (92), Neptunium (93), Plutonium (94), Americium (95), Curium (96), Berkelium (97), Californium (98), Einsteinium (99), Fermium (100), Mendelevium (101), Nobelium (102)

Figure 1.1: Periodic system of elements, where laser cooled species are marked in blue box. Taken from [7].

With the emergence of the optical frequency combs, the field of metrology thrived [8]. This laser source connected the RF spectrum to the optical frequencies which greatly simplified arduous frequency chains [9]. Its importance is awarded a Nobel prize in 2005 to Hall and Hänsch[10].

The properties of a frequency comb make it a viable candidate to solve some of the problems of laser cooling [11]. Frequency combs are usually produced from the mode-locked femto- or picosecond lasers. Due to the high peak powers of the pulses, non-linear effects such as second-harmonic generation, sum-frequency generation, and high-harmonic generation are much more efficient than using the continuous-wave lasers with the same average power. This makes a frequency comb a perfect candidate to cool atomic species with cooling transitions in the vacuum-ultraviolet spectrum [11, 12, 13]. To cool atoms with complex energy level structures many cooling and repumping lasers are required. Frequency comb spectrum

has many phase-coherent equidistant modes with narrow linewidth which could excite necessary atomic transitions. Frequency comb could be used for direct cooling of molecules, where multiple molecular transitions have to be excited simultaneously [14].

Usage of a frequency comb in laser cooling experiments can be extended beyond cooling of single atomic, molecular or ionic species. A frequency comb is proposed as a laser source for cooling multiple atomic species simultaneously [15]. In the proposal, single comb modes are used as cooling (and/or repumping) lasers for different atomic species simultaneously. This can have big implications if the field of atom interferometers. Multi-species interferometers would benefit from increased dynamic range, which improves the sensitivity and the resolution of the device [16]. Usage of the frequency comb (FC) would greatly simplify the experiments, where instead of several cw lasers, one FC laser is required. One of the most fascinating application of the atom interferometry experiments is for space application experiment, which is used for tests of the free fall universality [17]. Other potential applications of the simultaneous multi-species cooling with a frequency comb are generation of the hetero-nuclear molecules [18], and generation of quantum-degenerate-mixtures [19].

In literature, there are reports of the laser cooling of atomic and ionic species using a frequency comb. A brief description of the experiments on these species is presented in section 4.1.

## 1.2 Quantum memories

The long-term goal of quantum communications and quantum technologies is the establishment of a quantum network. One of the most important properties of the quantum network is the security, where an eavesdropping attempt would result in the collapse of the quantum information so the sender and the receiver of the information would notice it. The quantum information is transferred to a remote location using an optical fiber. The flaw of the quantum network is the complexity of information transfer over long distances. Quantum information is attenuated very rapidly over long distances so we have to build quantum repeater devices to send quantum information over long distances [20]. In the quantum network, information would be sent from node to node, where the attenuation of the information between two consecutive nodes is acceptable. In the nodes, a process of entanglement-swapping would occur [21], and the newly swapped information would be sent to the next node.

Quantum memories play a big role in the process of entanglement-swapping. They are instruments where quantum information can be stored for some time, and then be released on-demand so the timing of arrival of two photons can be synchronized.

Quantum memories can be produced in many different samples, atomic vapor [22], cold atoms [23], or solid-state samples [24]. Memories based on the cold atoms and solid-state samples have great performances but have big disadvantages over the memories based on the atomic vapor. Experiments with solid-state samples required cooling to cryogenic temperatures to reduce noise and the experiments with cold atoms are complex and cumbersome. This makes the quantum memories based on the atomic vapor good candidates for real-life applications.

There are many different protocols of storage and retrieval processes. Some of these protocols are based on the electromagnetically induced transparency [22], gradient-echo methods [25], Raman memories [26], atomic frequency comb [27] and hybrid protocols [28].

Electromagnetically induced transparency (EIT) is a relatively simple protocol to create quantum memory with relatively long storage times [29]. EIT is an effect where the probe laser beam is transmitted through the medium prepared by the control laser beam, where in the usual condition it would be absorbed [30]. The first experimental demonstration of the EIT was on strontium vapor [31]. Another important effect of the EIT is the change of the refraction index. Pulse propagating through the EIT medium is slowed because of reduced group velocity. This effect is called slow light and it is crucial for the EIT-based quantum memories [32].

## 1.3 Thesis outline

In the first chapter, I present a brief introduction to the field of laser cooling and quantum memories.

A brief description of the laser cooling and trapping is presented in chapter 2. Here I present only the essential results necessary for an understanding of the topic. A short description of the principle of work of a frequency comb is also presented.

In the third chapter, I present the theoretical model of the comb-atom interaction in 1D. Two counter-propagating pulse trains are interacting with a six-level atom. From the time dynamics of the density matrix elements, radiation pressure force and diffusion coefficient are calculated. Also, the stationary state temperature of atoms is calculated.

Three sets of comb parameters are presented and the effect of different comb parameters on the cooling process is analyzed.

In the fourth chapter experiment on simultaneous laser cooling with a frequency comb is presented. I present the experimental setup necessary for the generation of a dual-species magneto-optical trap. The repetition rate of the frequency comb pulses enabled simultaneous interaction with two Rb isotopes. Simultaneous radiation pressure force measurements are presented, where radiation pressure force is calculated from the displacement of the cloud's

center of mass. Here I present the results of the simultaneous laser cooling with a frequency comb in 1D. The temperature of the cooled clouds for both Rb isotopes is close to the Doppler temperature.

The fifth chapter is dedicated to the recent experiment where we demonstrated quantum memories based on electromagnetically induced transparency. EIT is used to measure the ground state decoherence rate for three glass cells with different coatings and buffer gas fillings. We measured quantum memory efficiency and storage time for these three cells, where for the cell with the lowest decoherence rate longest storage time was measured and the best efficiency.

In the last chapter, I summarize the results presented in the thesis and give an outlook on the plans and future experiments.

# Chapter 2

## Laser cooling a with frequency comb

In this chapter, I will present the basics of laser cooling and trapping. A detailed description of laser cooling and trapping is common in literature, even in undergraduate literature. The theory presented here is based on the popular book in the field, *Laser cooling and trapping* by Metcalf and van der Straten [33]. The description is also following the notes by H. Perrin [34, 35].

In this chapter I also present the theoretical description of frequency combs, based on the book chapter *Short and ultrashort laser pulses* in [36] and [37]. In the chapter, there is a brief description of the frequency comb laser cooling.

### 2.1 Quantum mechanical description of atom-light interaction

#### 2.1.1 Optical Bloch equations for two-level atom

Atom's time dynamics is described using a time-dependent Schrödinger equation

$$\hat{H}\Psi(\mathbf{r}, t) = i\hbar \frac{\partial \Psi(\mathbf{r}, t)}{\partial t}. \quad (2.1)$$

For a time-independent and field-free atom Hamiltonian  $\hat{H}_0$ , eigenfunctions  $\phi_n(\mathbf{r})$  are solutions of the Schrödinger equation. To describe the laser cooling, addition of the electromagnetic field is necessary and it modifies the atom's Hamiltonian to be  $\hat{H} = \hat{H}_0 + \hat{H}'$ . Solutions of the Eq. (2.1) can be expanded in terms of eigenfunctions  $\phi_n(\mathbf{r})$ :

$$\Psi(\mathbf{r}, t) = \sum_k c_k(t) \phi_k(\mathbf{r}) e^{i\omega_k t}. \quad (2.2)$$

Inserting this solution into the Schrödinger equation yields:

$$i\hbar \frac{dc_j(t)}{dt} = \sum_k c_k(t) H'_{jk}(t) e^{i\omega_{jk}t}, \quad (2.3)$$

where  $H'_{jk} = \langle \phi_j | \hat{H}'(t) | \phi_k \rangle$  and  $\omega_{jk} = \omega_j - \omega_k$ .

In this brief theory overview, the case of the two-level atom will be studied. This model provides a general description of the laser cooling concept, but is not applicable in experiments, since atomic energy level structure is more complex. In this approximation, only nonzero off-diagonal elements are  $\hat{H}_{ge}(t) = \hat{H}_{eg}^*(t)$ , where index  $g$  represents the ground state and  $e$  the excited state of an atom. The interaction Hamiltonian is described with:

$$\hat{H}'(t) = -e\mathbf{E}(\mathbf{r}, t) \cdot \mathbf{r}. \quad (2.4)$$

The electric field operator for a plane wave traveling in  $+z$  direction is  $\mathbf{E}(\mathbf{r}, t) = E_0 \hat{\epsilon} \cos(kz - \omega_L t)$ , where  $E_0$  is the electric field amplitude,  $\hat{\epsilon}$  is the polarization vector and  $k$  and  $\omega_L$  are electric field wavenumber and frequency, respectively. Here we have introduced the dipole approximation, where we neglect the spatial variation of the electric field. The approximation is valid since the wavelength of the electric field is typically hundreds of nanometers, and atom size is generally  $< 1$  nm. Term  $\hat{H}_{eg}(t)'$  now becomes  $\hat{H}_{eg}(t)' = \hbar\Omega \cos(kz - \omega_L t)$ , where  $\Omega$  is the Rabi frequency defined as:

$$\Omega = -\frac{eE_0}{\hbar} \langle e | r | g \rangle. \quad (2.5)$$

Hamiltonian  $\hat{H}_{eg}(t)'$  oscillates at two frequencies,  $\omega_L + \omega_{ge}$  and  $\delta = \omega_L - \omega_{ge}$ . The latter frequency  $\delta$  is called detuning and is defined as the difference between the laser frequency and the atomic resonance frequency. If the detuning is negative, it is usually called *red* detuning and if it is positive it is called *blue* detuning. In the case of the near-detuned field, which will be considered in this thesis,  $\omega_L + \omega_{ge}$  is much larger than the detuning, so terms that oscillate at this frequency will be neglected. This approximation is called the rotating-wave approximation.

The equation (2.3) now becomes:

$$\frac{dc_g}{dt} = -\frac{i}{2}c_e\Omega^*e^{i\delta t}, \quad (2.6a)$$

$$\frac{dc_e}{dt} = -\frac{i}{2}c_g\Omega e^{-i\delta t}. \quad (2.6b)$$

This set of equations describes the coherent evolution of the amplitudes in the two-level atom in the radiation field. To describe a realistic system, it is necessary to include the effects of the spontaneous emission. This is done using the density matrix formalism, where density matrix is defined as  $\rho = |\Psi\rangle\langle\Psi|$ , where matrix elements are:

$$\rho_{ij} = \langle\phi_i|\rho|\phi_j\rangle = \langle\phi_i|\Psi\rangle\langle\Psi|\phi_j\rangle = c_ic_j^* \quad (2.7)$$

Density matrix formalism enables not only the description of pure states and mixed states, but it also enables the calculation of the expectation values of the quantum mechanical operators:

$$\begin{aligned} \langle\hat{A}\rangle &= \langle\Psi|\hat{A}|\Psi\rangle = \left\langle\sum_i c_i\phi_i\left|\hat{A}\right|\sum_j c_j\phi_j\right\rangle = \sum_{i,j} c_i^*c_j\langle\phi_i|\hat{A}|\phi_j\rangle \\ &= \sum_{i,j} \rho_{ji}\hat{A}_{ij} = \sum_j \left(\rho\hat{A}\right)_{jj} = Tr\left(\rho\hat{A}\right). \end{aligned} \quad (2.8)$$

The time evolution of the density matrix is described with von Neumann equation

$$i\hbar\frac{d\rho}{dt} = [\hat{H}, \rho]. \quad (2.9)$$

Generally, for a system of N-level atoms, the size of the density matrix is  $N\times N$ , so in the case of the two-level model described in this chapter density matrix is

$$\rho = \begin{pmatrix} \rho_{ee} & \rho_{eg} \\ \rho_{ge} & \rho_{gg} \end{pmatrix} = \begin{pmatrix} c_e c_e^* & c_e c_g^* \\ c_g c_e^* & c_g c_g^* \end{pmatrix}. \quad (2.10)$$

Diagonal elements of the density matrix are called *populations* and the off-diagonal elements are called *coherences*. From the evolution equations for amplitudes (2.6), time evolution equations for the  $\rho_{ij}$  terms can be easily found. For example, the time evolution of the  $\rho_{gg}$  term is:

$$\frac{d\rho_{gg}}{dt} = \frac{dc_g}{dt}c_g^* + c_g\frac{dc_g^*}{dt} = i\frac{\Omega^*}{2}\tilde{\rho}_{eg} - i\frac{\Omega}{2}\tilde{\rho}_{ge}, \quad (2.11)$$

where  $\tilde{\rho}_{ge} = \rho_{ge}e^{-i\delta t}$ . This and other equations for  $\rho_{ij}$  terms are not describing a realistic system since they do not describe effects such as spontaneous emission. Spontaneous emission effects are included by introducing decays to the density matrix terms describing populations and coherence. Coherence terms decay exponentially with the rate of  $\gamma/2$ . Decay of the excited state population with the exponential rate of  $\gamma$  increases population in the ground state at the same rate. Inclusion of the spontaneous emission terms in the density matrix time evolution equations leads to the known Optical Bloch equations (OBEs):

$$\frac{d\rho_{gg}}{dt} = +\gamma\rho_{ee} + \frac{i}{2}(\Omega^*\tilde{\rho}_{eg} - \Omega\tilde{\rho}_{ge}), \quad (2.12a)$$

$$\frac{d\rho_{ee}}{dt} = -\gamma\rho_{ee} + \frac{i}{2}(\Omega\tilde{\rho}_{ge} - \Omega^*\tilde{\rho}_{eg}), \quad (2.12b)$$

$$\frac{d\tilde{\rho}_{ge}}{dt} = -\left(\frac{\gamma}{2} + i\delta\right)\tilde{\rho}_{ge} + \frac{i}{2}\Omega^*(\rho_{ee} - \rho_{gg}), \quad (2.12c)$$

$$\frac{d\tilde{\rho}_{eg}}{dt} = -\left(\frac{\gamma}{2} - i\delta\right)\tilde{\rho}_{eg} + \frac{i}{2}\Omega(\rho_{gg} - \rho_{ee}). \quad (2.12d)$$

It is worth mentioning that the decay of the coherences and populations are described with a single parameter  $\gamma$ . This is true in the case of laser cooling, but in the case where collisions play a role, decay of coherences and populations are described using different decay parameters.

The steady-state solution of the OBEs is calculated by setting the time derivative of the density matrix elements to zero, and by using the properties that coherence terms are complex conjugates  $\rho_{eg} = \rho_{ge}^*$  and that the total population is conserved  $\rho_{gg} + \rho_{ee} = 1$ . Steady-state solution for the excited state population is:

$$\rho_{ee} = \frac{s}{2(1+s)} = \frac{s_0/2}{1+s_0+(2\delta/\gamma)^2}, \quad (2.13)$$

where saturation parameter  $s$  is defined as:

$$s = \frac{s_0}{1+(2\delta/\gamma)^2}, \quad (2.14)$$

and  $s_0$  is the on-resonance saturation parameter:

$$s_0 = 2|\Omega|^2/\gamma^2 = I/I_s. \quad (2.15)$$

Here  $I$  is the laser intensity and  $I_s$  is the saturation intensity. The steady-state solution for one

of the coherence terms is:

$$\rho_{eg} = \frac{i\Omega}{2(\gamma/2 - i\delta)(1 + s)}. \quad (2.16)$$

The atomic line associated with  $|g\rangle \rightarrow |e\rangle$  transition is obtained by scanning the laser frequency i.e. detuning in the Eq. (2.13). This is a Lorentzian lineshape curve with full width at half-maximum (FWHM) of  $\gamma$  for  $s_0 \ll 1$ . By increasing the laser intensity, i.e. laser power, linewidth is broadened and equal to  $\gamma_P = \gamma\sqrt{1 + s_0}$ . This is a power broadening mechanism and is crucial in measuring the linewidth of the excited state. In the usual stationary-state laser cooling conditions, other broadening mechanisms like Doppler and pressure broadening are negligible but can play a significant role in special circumstances.

### 2.1.2 Light forces

Forces exerted on the atoms by the laser light field are calculated using the Ehrenfest theorem.

$$\mathbf{F} = \langle \hat{F} \rangle = \frac{d}{dt} \langle \hat{p} \rangle = \frac{i}{\hbar} \langle [\hat{H}, \hat{p}] \rangle = - \langle \nabla \hat{H} \rangle. \quad (2.17)$$

This theorem is the quantum mechanics analogue of the classical expression stating that the force is equal to the negative gradient of the potential,  $\mathbf{F} = -\nabla U$ . Only the interaction part of the Hamiltonian is relevant, and using the dipole approximation the light force becomes:

$$\mathbf{F} = e \langle \nabla (\mathbf{E}(\mathbf{r}, t) \cdot \mathbf{r}) \rangle = e \nabla (\langle \mathbf{E}(\mathbf{r}, t) \cdot \mathbf{r} \rangle). \quad (2.18)$$

In the dipole approximation spatial variation of the electric field over the size of an atom is neglected so we can interchange the gradient with the expectation value operations. Using the definition of the Rabi frequency (2.5) and the definition of the expected value of an arbitrary quantum mechanical operator  $\langle \hat{A} \rangle = \text{Tr}(\rho \hat{A})$ , expectation value of the force is:

$$\mathbf{F} = \hbar (\nabla \Omega \rho_{eg}^* + \nabla \Omega^* \rho_{eg}). \quad (2.19)$$

Now, by evaluating the gradient operator and splitting the force into the real and imaginary parts, for the electric field  $\mathbf{E}(\mathbf{r}) = \mathbf{E}_0(\mathbf{r}) \exp(i\phi(\mathbf{r})) + c.c.$ , the expression for the force becomes:

$$\mathbf{F} = \hbar \frac{\nabla \Omega}{\Omega} (\Omega \rho_{eg}^* + \Omega^* \rho_{eg}) + i \hbar \nabla \phi (\Omega \rho_{eg}^* - \Omega^* \rho_{eg}) \quad (2.20)$$

This general expression can be evaluated for any situation where OBEs can be solved for  $\rho_{eg}$ . For the case presented in this chapter, we use the expression (2.16) to get the force exerted on a two-level atom:

$$\mathbf{F} = -\frac{\hbar s}{1+s} \left( \delta \frac{\nabla \Omega}{\Omega} + \frac{\gamma}{2} \nabla \phi \right). \quad (2.21)$$

Force here has two terms, where the former is proportional to the laser detuning and the gradient of the field amplitude, and the latter is proportional to the gradient of the field phase. The first term leads to the conservative force called dipole force, while the second term leads to the dissipative force called radiation pressure force. In the laser cooling experiment detuning of the laser electric field is small and beams are approximated with plane waves, so the dipole force is negligible in comparison to the radiation pressure force.

In the process of the absorption of light, momentum from the photon is transferred to the atom. In the case that atom decays by spontaneous emission, atomic recoil is in a random direction, so the net change of the atom's momentum is zero. The average force exerted on the atom in the process of absorption and spontaneous emission is:

$$\mathbf{F}_{sp} = \hbar \mathbf{k} \gamma \rho_{ee}. \quad (2.22)$$

Inserting the solution of the OBEs for excited state population (2.13), the force exerted on the atom is:

$$\mathbf{F}_{sp} = \frac{\hbar \mathbf{k} s_0 \gamma / 2}{1 + s_0 + (2\delta/\gamma)^2}. \quad (2.23)$$

We identify this as the latter term in the Eq. (2.21). The phase of the plane wave is equal to  $\phi = -\mathbf{k}_L \cdot \mathbf{r}$ , and the gradient of the phase is  $\nabla \phi = -\mathbf{k}_L$ . For high laser intensities the force saturates to  $F_{max} = \hbar k \gamma / 2$ . Force dependence on the laser intensity and detuning is presented in the Fig. 2.1

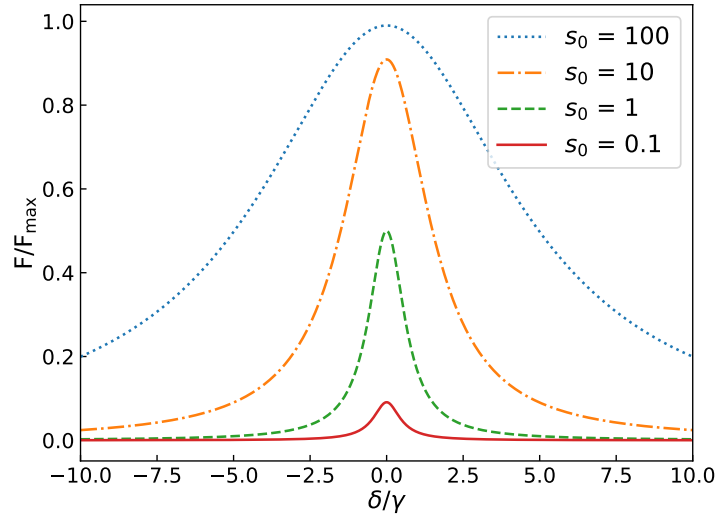


Figure 2.1: Radiation pressure force dependence on the laser detuning and intensity. The force is in units of  $F_{max} = \hbar k \gamma / 2$ .

## 2.2 Laser cooling and trapping

Laser cooling is an experimental technique where atoms are cooled to temperatures near the absolute zero temperature. Atoms are interacting with an environment through processes of absorption and spontaneous emission so the environment is changing consistently. This kind of system can be in a steady-state, but it is not in thermal equilibrium so the usual thermodynamic definition of temperature is inappropriate. In this kind of system temperature is defined as the average kinetic energy of atoms in one dimension:

$$\frac{1}{2} k_B T = \langle E_k \rangle. \quad (2.24)$$

There are several characteristic temperatures in laser cooling. The first one is the Doppler temperature, which is the temperature limit for some laser cooling processes. It is defined as

$$k_B T_D = \frac{\hbar \gamma}{2}. \quad (2.25)$$

For alkali metals, which are the usual elements in the laser cooling experiments, Doppler temperature is in the range of several hundred  $\mu\text{K}$ , and for the  $^{85}\text{Rb}$  and  $^{87}\text{Rb}$  it is  $T_D = 145.57 \mu\text{K}$  [38, 39].

Another characteristic temperature is the recoil temperature. This is the temperature associ-

ated with the energy of a single photon recoil. It is defined as:

$$k_B T_R = \frac{\hbar^2 k^2}{m}, \quad (2.26)$$

where  $k$  is the wavenumber of the atomic transition, and  $m$  is the atom's mass. Typical recoil temperature is around a few  $\mu\text{K}$ . In the experiments, it is possible to cool the atomic samples below the recoil temperature, by using the evaporative cooling methods.

### 2.2.1 Doppler cooling

The radiative force exerted on atoms at rest by a single laser beam is defined in Eq. (2.23). If there are two counter-propagating laser beams that interact with an atom, radiative force is cancelled. Atoms that are moving experience the Doppler effect, which shifts the frequency of the laser beams. Doppler shift  $\omega_D = -\mathbf{k} \cdot \mathbf{v}$  changes the radiation force so it becomes velocity dependent.

For the Doppler cooling scheme in one dimension, two counter-propagating laser beams have to be red detuned with respect to the atomic resonance. In this case, the total force exerted on atoms is dissipative, so when the velocity is negative, the force is positive and the atom's velocity is reduced. Analogously, when the atom's velocity is positive, the force is negative and again reduces the atom's velocity. The force as a function of the atom's velocity is presented in Fig. 2.2. for the detuning of  $\delta = -0.5\gamma$ . The total force exerted on the atoms is  $\mathbf{F}_{OM} = \mathbf{F}_+ + \mathbf{F}_-$ , where:

$$\mathbf{F}_{\pm} = \pm \frac{\hbar \mathbf{k} \gamma}{2} \frac{s_0}{1 + s_0 + [2(\delta \mp |\omega_D|)/\gamma]^2}. \quad (2.27)$$

For the range of velocities near zero, the total force can be approximated with a linear force with a negative slope, which behaves like the viscous damping of the velocity. Neglecting the terms of the order  $v^4$  and higher, the damping force is:

$$\mathbf{F}_{OM} = \frac{8\hbar k^2 \delta s_0 \mathbf{v}}{\gamma(1 + s_0 + (2\delta/\gamma)^2)^2} = -\beta \mathbf{v}. \quad (2.28)$$

where  $\beta$  is the damping coefficient. It is easy to see that this force leads to the reduction of the atom's velocity to zero, and consequentially to zero temperature, which is not physically possible. In reality, this is prevented by the heating that is caused by the spontaneous emission, i.e. photon recoil in a random direction. This limits the lowest achievable temperature in the Doppler cooling to the Doppler temperature (2.25). By equating the cooling and heating rates,

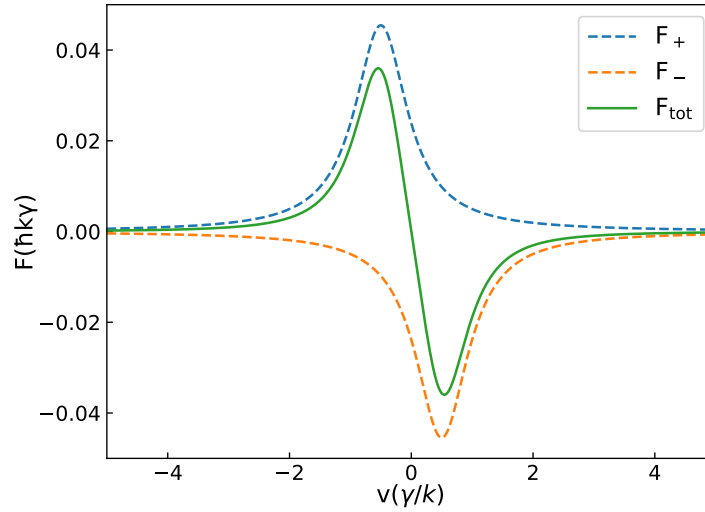


Figure 2.2: Radiation pressure force for a two-level atom in 1D laser cooling as a function of atomic velocity. Contributions from individual laser beams,  $\mathbf{F}_+$  and  $\mathbf{F}_-$  components of the force, as well as the total force on the atom are presented. Near  $v = 0$  the radiation force can be approximated as a linear viscous force. Detuning of the laser beams from the atomic resonance is  $\delta = -0.5\gamma$ .

one can find the Doppler temperature profile as a function of detuning in the limit of low laser intensity [40]:

$$k_B T = \frac{\hbar\gamma}{4} \frac{1 + (2\delta/\gamma)^2}{2|\delta|/\gamma}, \quad (2.29)$$

The temperature minimum is achieved for the detuning of  $\delta = -\gamma/2$  and is equal to  $T_D = \frac{\hbar\gamma}{2k_B}$ . Doppler temperature limit is therefore only the function of the atomic linewidth. For  $^{85}\text{Rb}$  and  $^{87}\text{Rb}$  Doppler temperature is  $T_D \approx 145.57 \mu\text{K}$  [38, 39]. In the usual experimental conditions, temperatures below the Doppler limit are routinely achieved, using the sub-Doppler cooling techniques [41].

In the real experiments atoms have energy level structure that is more complex than the simple two-level scheme we used to describe the laser cooling process. Most experiments use alkali atoms, which have only one valence electron. These atoms are called hydrogen-like atoms since their energy level structure is analogous to the hydrogen's level structure. In order to cool the atoms it is necessary to red detune the cooling laser with respect to the cooling transition. Despite the near-resonant excitation of the closed cooling transition, there is slight possibility of the off-resonant excitation of some other excited level, from which the atom can relax into the ground level which is not resonant with the cooling beam. These atoms are then lost from the cooling cycle and can not be cooled any more. To prevent this, in the experiments

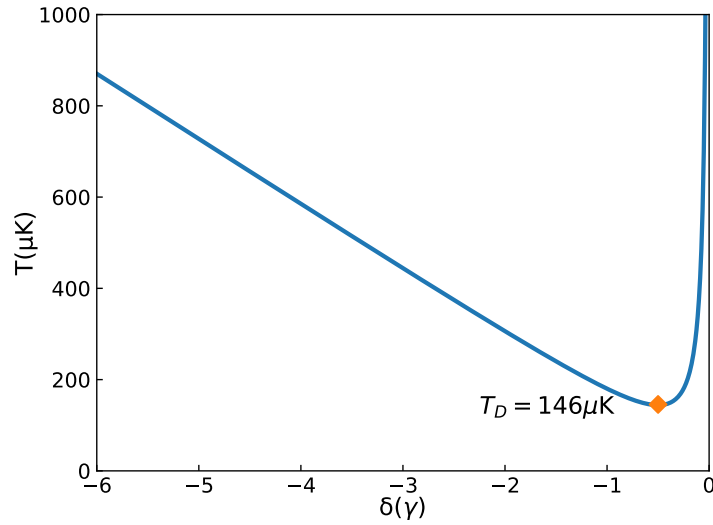


Figure 2.3: Doppler temperature as a function of the laser detuning from the cooling transition. Minimum temperature is achieved at  $\delta = -\gamma/2$ , and for Rb atoms is  $T_D = 145.57 \mu\text{K}$  [38, 39].

additional lasers are used to keep atoms in the cooling process. These lasers are conveniently called repumping lasers. In usual experiments, there is at least one repumping laser, whereas for atoms with more complex energy level structure multiple repumping lasers are needed.

### 2.2.2 Magneto-optical trap

To achieve 1D laser cooling, it is necessary to setup two counter-propagating laser beams that are red detuned from the cooling transition. In 3D situation is similar, it is necessary to have three orthogonal pairs of counter-propagating beams, one for each dimension. However, atoms cooled to only few  $\mu\text{K}$  are still moving with velocity around 10 cm/s, and can escape the cooling region. In order to keep the atoms in the cooling region, it is necessary to trap the atoms in the area by introducing the spatially dependent trapping force. This is achieved by using the gradient of the magnetic field and circularly polarized laser beams [42]. This method is called Magneto-optical trap (MOT) and is commonly used in cold atoms experiments.

The idea behind the magneto-optical trap is the interaction of atoms with spin  $\mathbf{J} = \mathbf{L} + \mathbf{S}$ , and spatially varying magnetic field  $\mathbf{B}(\mathbf{r})$ . This interaction  $\hat{V}_m = -\hat{\mathbf{J}} \cdot \mathbf{B}(\mathbf{r})$  Zeeman shifts the magnetic sublevels  $|F, m_F\rangle$  by  $m_J g_J \mu_B B$ , where  $g_J$  is the Landé factor for spin state  $J$ , and  $\mu_B$  is Bohr magneton.

For simplicity, let us discuss a situation for an atom with ground state  $J = 0$  and excited state  $J' = 1$ , presented in Fig. 2.4. The resonant frequency for transition  $|J = 0, m_J = 0\rangle \rightarrow |J' = 1, m'\rangle$  is now  $\omega_0 + m' g_J \mu_B B$ . In the case of linear gradient of magnetic field  $B(z) = b'z$ ,

where  $b'$  is the magnetic field gradient, detuning from the transition frequency with respect to the driving frequency equals:

$$\delta' = \delta - \frac{m' g_J \mu_B b' z}{\hbar}, \quad (2.30)$$

where  $\delta = \omega_L - \omega_0$ . The consequence of this effect is that for  $z > 0$ , for a transition with  $\Delta m = +1$ , the detuning will increase, and thus tuning the transition further from the resonance, whereas for the transition with  $\Delta m = -1$ , detuning will decrease, which makes the transition closer to the resonance. The transition frequency  $|J = 0, m = 0\rangle \rightarrow |J' = 1, m_J\rangle$  can be written as

$$\omega_{m'} = \omega_0 + m' \gamma' b' x, \quad (2.31)$$

where  $\gamma' = g_J \mu_B / \hbar$  is the gyromagnetic ratio for the transition.

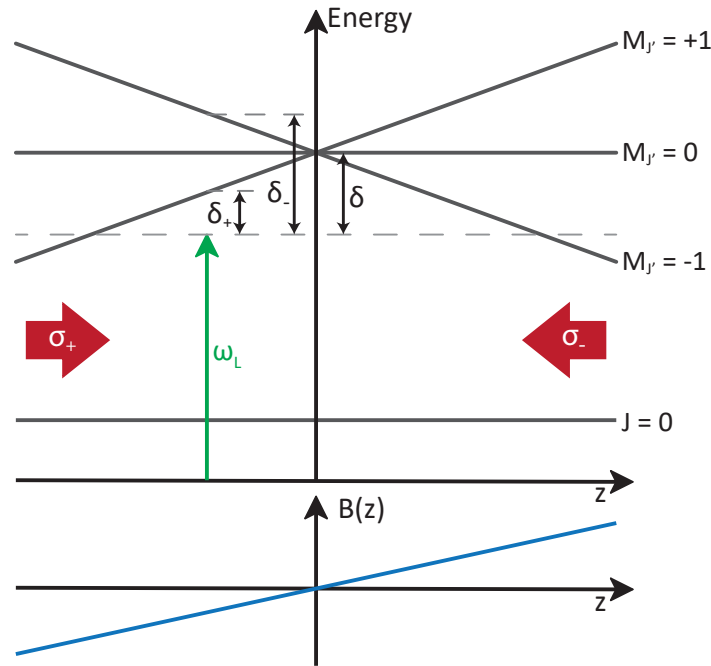


Figure 2.4: Energy level diagram for an atom with ground state  $|J = 0\rangle$  and  $J' = 1$  excited state. Due to the magnetic field gradient, displayed in bottom part of the figure, excited states are Zeeman shifted.  $\sigma^+$  beam propagating towards  $+z$  direction is preferentially absorbed by atoms at  $z < 0$ , whereas  $\sigma^-$  beam is preferentially absorbed by atoms at  $z > 0$ . This preferential absorption creates a spatially dependent force which pushes atoms to the center of the trap, thus creating a magneto-optical trap.

To create a spatially dependent force, we setup the laser beams to be circularly polarized,

where the beam that propagates towards  $+z$  direction is  $\sigma^+$  polarized, and the beam that propagates towards  $-z$  direction is  $\sigma^-$  polarized. In this case, due to the selection rules,  $\sigma^+$  beam can only drive the  $|J = 0, m = 0\rangle \rightarrow |J' = 1, m' = 1\rangle$  transition and the  $\sigma_-$  beam can only drive the  $|J = 0, m = 0\rangle \rightarrow |J' = 1, m' = -1\rangle$  transition. At  $z < 0$ ,  $\sigma^+$  beam is preferentially absorbed, due to the smaller detuning than the  $\sigma^-$  beam with respect to the transitions these beams can drive. This imbalance pushes the atom towards the  $z = 0$ . For  $z > 0$  situation is analogous, and the atom preferentially absorbs the  $\sigma^-$  beam and is again pushed towards the  $z = 0$ .

This principle of magneto-optical trap is extendable to states with a higher number of magnetic sub-states and three dimensions. In the experiments magnetic field gradient is usually created using an anti-Helmholtz configuration of coils, which creates a quadrupole magnetic field in all dimensions and is linear near the center of the trap:

$$\mathbf{B}(\mathbf{r}) = b'(x\mathbf{e}_x + y\mathbf{e}_y - 2z\mathbf{e}_z). \quad (2.32)$$

The total force exerted on the atoms is a sum over all contributions, given by the expression (2.27). With the introduction of the magnetic field gradient, detuning becomes spatially dependent and is equal to:

$$\delta_{\pm} = \delta \mp \mathbf{k} \cdot \mathbf{v} \mp \gamma' b' z / \hbar. \quad (2.33)$$

For small  $v$  and  $z$ , which produce small Doppler shift and Zeeman shift in comparison to  $\delta$ , we can expand the force expression. In the  $z$  direction force is then equal to

$$F_z = -\beta v_z - \kappa z, \quad (2.34)$$

where  $\beta$  is the damping coefficient introduced in Eq. (2.28), and the  $\kappa = \frac{\gamma' b'}{\hbar k}$  is the spring constant.

The quadrupole magnetic field given in Eq. (2.32) is twice as strong in one dimension, in comparison to the other two dimensions, as a consequence of the requirement of vanishing divergence of the magnetic field  $\nabla \cdot \mathbf{B} = 0$ . The trapping force in the case of equal intensities of laser beams is then  $\mathbf{F}(\mathbf{r}) = -\kappa x \hat{x} - \kappa y \hat{y} - 2\kappa z \hat{z}$ , where  $z$  is the direction of coils symmetry. To get the isotropic restoring force, the intensity of beams propagating in  $z$  direction is reduced by a factor of two.

## 2.3 Frequency comb laser cooling

Continuous-wave (cw) lasers are commonly used for the generation of cold and ultra-cold atomic clouds. Still, laser cooling is limited to a few atomic and ionic species due to the unavailability of cw laser light required to drive the cooling transitions, especially in the VUV spectrum, or due to the complex energy level structure of atoms. The proposed solutions to these problems is the use of a frequency comb (FC) as the cooling laser [11]. The advantage of the FC is the richness of its spectrum which enables the usage of many comb modes to simultaneously cool multiple atomic species [15].

Frequency comb light is a crucial tool in any atomic physics laboratory. Its importance has been awarded with Nobel prize in physics in 2005. to J. H. Hall and T. W. Hänsch for the development of the optical frequency comb spectroscopy [10]. The importance of a frequency comb lies in its spectrum, which bridges the gap between RF frequencies and optical frequencies. A spectrum of a FC is defined as:

$$f_n = n \cdot f_{rep} + f_{ceo}, \quad (2.35)$$

where  $f_n$  is the frequency of the  $n$ -th comb mode,  $f_{rep}$  is the pulse repetition frequency and  $f_{ceo}$  is the carrier-envelope offset frequency. Repetition frequency and carrier-envelope frequency are frequencies in the RF spectrum, typically several to few hundred MHz, and  $f_n$  is the optical frequency of a few hundreds of THz. Index  $n$  is an integer number around  $10^5$  and is connecting the RF spectrum and the optical spectrum.

### 2.3.1 Generation of ultrashort laser pulses

A frequency comb is the spectrum of a mode-locked ultrashort pulse laser. In the laser cavity mode-locking is achieved by creating a fixed phase relation between the longitudinal modes. As a consequence, the longitudinal modes interfere constructively at specific moment and position within the cavity, creating a short laser pulse. This phenomenon is illustrated in Fig. 2.5 for four cavity modes.

The longitudinal modes of a laser cavity are standing waves given with:

$$\nu_m = \frac{mc}{2nL}, \quad (2.36)$$

where  $\nu_m$  is the frequency of the  $m$ -th cavity mode,  $c/n$  is the speed of light in the medium with refraction index  $n$  and  $L$  is the length of the cavity. However, only longitudinal modes that are within the gain bandwidth  $\delta\nu_g$  of the laser medium are supported, which limits the laser

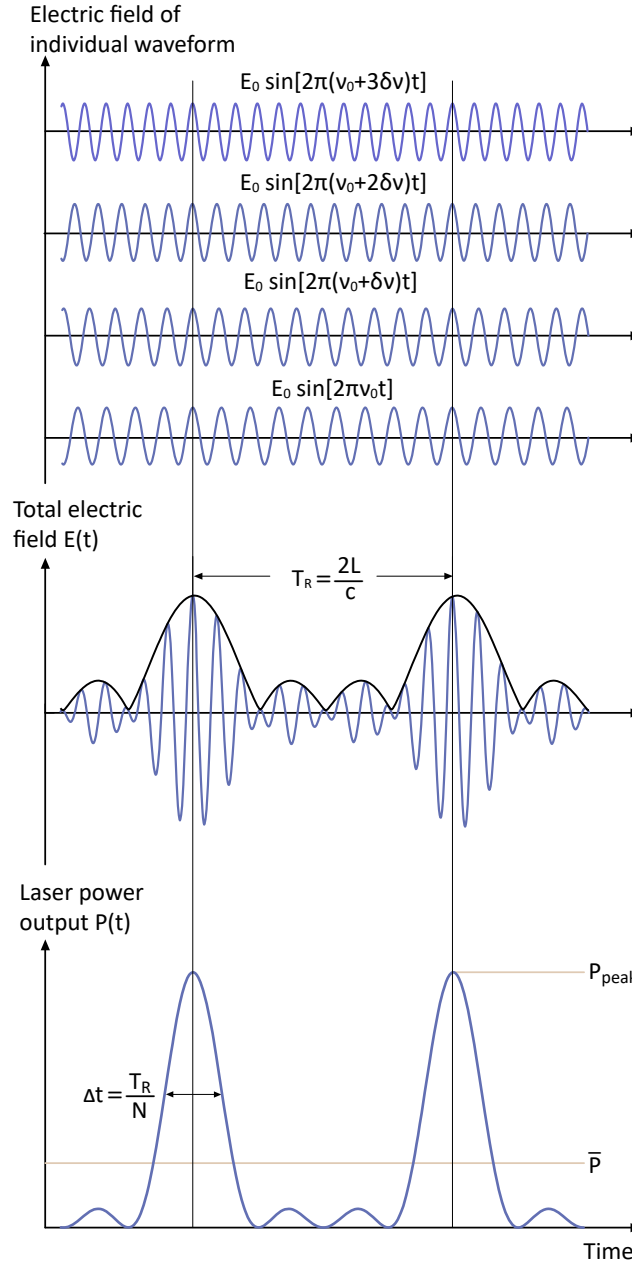


Figure 2.5: Superposition of the electric field modes in a laser cavity of a mode-locked ultrashort pulse laser. The frequency difference of the modes presented is  $\delta\nu$ . The modes interfere constructively at a specific position and moment, and a pulse is created. The peak power of the output pulse grows and the pulse duration shortens by increasing the number of coherently superimposed longitudinal modes. Adapted from [36].

output spectrum. The number of modes is also dependent on the spacing between the modes  $\Delta = \nu_m - \nu_{m-1} = c/2nL$ , so for the case of a strong pump laser it is approximately  $\delta\nu_g/\Delta$ . To

create ultrashort laser pulses the number of supported modes has to be very high, around  $10^6$ , which is possible in a laser medium with broad gain bandwidth.

Suppose that  $M$  is the number of supported longitudinal modes of frequency  $\omega_m = 2\pi\nu_m = \omega_l + 2\pi m\Delta$ . Here  $\omega_l$  is the central laser frequency. The electric field of the modes is then:

$$\tilde{E}(t) = \sum_m \varepsilon_0 e^{i(\omega_m t + \Phi_m)} = \varepsilon_0 e^{i\omega_l t} \sum_{m=-(M-1)/2}^{m=(M-1)/2} e^{i(2m\pi\Delta t + \Phi_m)}. \quad (2.37)$$

$\varepsilon_0$  is the amplitude of the electric field of longitudinal modes. To generate strong pulses we require that the phase is the same for all modes  $\Phi_m = \Phi_0$ , i.e. the laser is mode-locked. In that case, the total electric field is [43]:

$$\tilde{E}(t) = \varepsilon_0 e^{i\Phi_0} e^{i\omega_l t} \frac{\sin(M\pi\Delta t)}{\sin(\pi\Delta t)}. \quad (2.38)$$

For a large number of modes  $M$ , pulses are repeated with the time  $T_R = 1/\Delta = 2nL/c$ , and pulse duration is around  $\tau_p \approx 1/M\Delta$ . With this, we conclude that the repetition period of pulses is defined by the laser cavity length, and the pulse duration is shorter if the number of locked modes is higher. The ratio between the pulse repetition period and pulse duration gives the approximate number of modes that are phase-locked in the cavity.

A more intuitive way of defining the total electric field of a pulse train with a repetition period of  $T_R$  is [43]:

$$\tilde{E}(t) = \sum_{n=0}^{\infty} \varepsilon(t - nT_R) e^{i\omega_l t} e^{in\Phi_R}. \quad (2.39)$$

Here  $\varepsilon(t)$  is the envelope of the laser pulse,  $\omega_l$  is the central laser frequency,  $\Phi_R$  is the carrier-envelope phase offset and  $n$  is the index of a pulse. A train of such ultrashort pulses is presented in Fig. 2.6(a).

The spectrum of the pulse train with a repetition period of  $T_R$  and carrier-envelope phase offset  $\Phi_R$  is called a frequency comb. It is presented in Fig. 2.6 (b) and is defined with the simple expression:

$$f_n = nf_R + f_{ceo}. \quad (2.40)$$

Spacing between the comb modes is called repetition frequency and is defined as  $f_R = 1/T_R$ , and other important frequency is called the carrier-envelope frequency  $f_{ceo} = \Phi_R/2\pi T_R$ . The frequency of the  $n$ -th comb mode is connected with these two RF frequencies by a high index

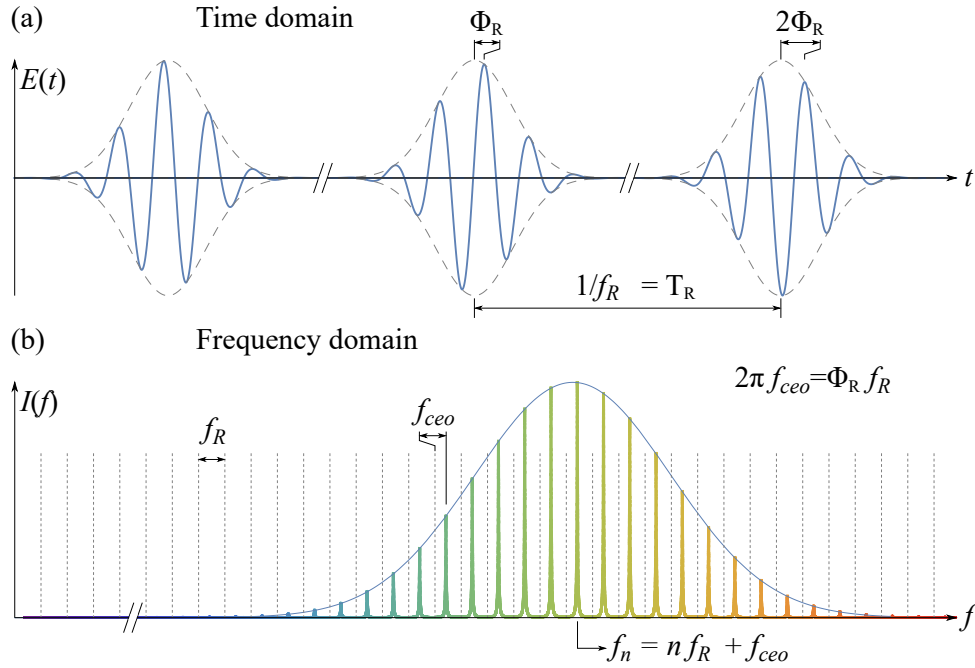


Figure 2.6: (a) Pulse train of a mode-locked laser, where the period between pulses is  $T_R$  and carrier-envelope offset between two consecutive pulses is  $\Phi_R$ . (b) Spectrum of the pulse train presented in (a). Comb spectrum is defined with  $f_{ceo}$  and the repetition frequency  $f_{rep}$ . Adapted from [44].

number  $n$ , which is in the range of  $10^5 - 10^6$ . By measuring and controlling these two RF frequencies, the whole spectrum is determined exactly, which is an important property of the frequency combs.

### 2.3.2 Frequency comb cooling

In comparison to continuous-wave laser, the spectrum of a frequency comb laser consists of many spectral modes. By precise manipulation of an FC spectrum, many of these modes can be used to excite cooling or repumping transitions in atoms. Using the FC light could help to overcome the limitations of the laser cooling imposed by using the cw lasers.

Today only a limited number of atomic species have been laser cooled [6]. Many other species are not laser cooled due to the unavailability of the laser light required to drive the cooling transitions, mostly in the vacuum ultraviolet spectral range (VUV). The most significant species that has not been cooled yet is hydrogen. Laser cooling of hydrogen would bring an exciting prospect in the research of the interaction between atoms, measurements of fundamental constants such as the Rydberg constant and many others. Currently, there are no laser sources that directly emit light with frequencies required for laser cooling of hydrogen. Light

at these frequencies is generated using different nonlinear processes such as second-harmonic generation (SHG), sum-frequency generation (SFG) and others. Frequency conversion using these nonlinear effects is very dependent on the laser power and here pulsed laser sources are preferred. Due to their pulsed nature, their peak powers are several orders of magnitude higher than the standard cw lasers, and then the nonlinear effects are more efficient.

Another limitation of laser cooling is due to the complexity of the energy level structure of atoms. When such atoms are excited, they can relax to many different states and are lost from the cooling cycle. To cool these atoms many repumping lasers are required so the experiments are complex and cumbersome. In this case, frequency comb spectrum can be used to excite the cooling transition as well as repumping transitions. The most exciting examples of such atoms are carbon, nitrogen and oxygen. Together with hydrogen, these atoms are the most interesting from the chemical and biological viewpoint, since they are the building blocks for most organic molecules.

Forming cold molecules consisting of carbon and hydrogen atoms could provide us with a better understanding of the chemical bonds in the molecules and we could study how these molecules interact. In comparison to atoms, molecules exhibit a very complex energy level structure, due to the existence of vibrational and rotational modes. There are several methods how to get cold samples of molecules. One method is to laser cool the atoms that form the selected molecule, and then by the process of photoassociation create cold molecules. Frequency comb light can also be used in this kind of experiment, where different comb modes can be used to simultaneously excite cooling and repumping transitions for the selected atoms, as well as to drive the photoassociation. Another method of cooling molecules is direct cooling. This experiment is complex due to the complexity of the molecular energy level structure, and here modes of the frequency comb can be employed as cooling and repumping lasers and to drive the molecules into the low ro-vibrational levels.

Frequency comb light can be used not only for cooling species that can not be cooled using cw lasers, but also to simplify the existing experiments. Many experiments would benefit from simplification of a laser system, for example, multiple species atomic interferometer experiments. By introducing multiple species in the experiment, these atomic interferometers would benefit from extending the dynamic range of a measurement, which would increase the sensitivity and accuracy of these atomic sensors. Another notable application would be for dedicated atomic interferometers built for space applications, where any reduction in complexity and mass of the experimental setup is crucial. These kind of experiments are built for fundamental tests of gravity and the universality of free fall [17].

Laser cooling with frequency combs has several different approaches where two of them

are presented in Fig. 2.7. In the first approach, a frequency comb excites the single-photon transition [12, 45]. Here only one comb mode participates in the excitation, as illustrated in Fig. 2.7(a). The repetition period is shorter than the excited state lifetime so the population is coherently accumulated in the excited state. In this approach, FC modes are equivalent to cw lasers. The drawback of this approach is that available power per comb mode is typically much smaller than in the cw laser experiments. The advantage of the FC in this approach is when multiple comb modes participate in cooling/repumping, or when multiple species are cooled simultaneously.

Second approach is to excite two-photon transitions using a frequency comb [46], presented in Fig. 2.7(b). Here all pairs of comb modes for which the condition of two-photon resonance is satisfied can participate in the excitation. This is possible since all modes of a frequency comb are coherent. In comparison to cw two-photon excitation, the scattering rate of the pulsed excitation is approximately the same if the average powers of the pulsed and cw lasers are the same. This enables laser cooling of species that have cooling transitions in VUV, where the generation of pulsed laser light is much more efficient than the cw light.

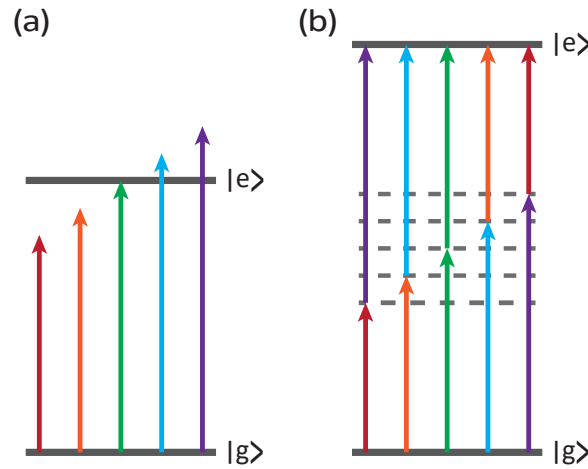


Figure 2.7: Two principles of frequency comb laser cooling. (a) Single photon cooling, where the repetition period is shorter than the excited state lifetime. (b) Two photon cooling with a frequency comb, where multiple excitation pathways sum coherently. Adapted from [11].

A theoretical model of comb-atom interaction that leads to the Doppler cooling has recently been developed [47, 15]. In this model, two counter-propagating pulse trains are interacting with two-level atoms, and the interaction is described by the Optical Bloch equations (OBEs). Since laser pulses are much shorter than the repetition period and excited state lifetime, time evolution of a system can be divided into four intervals. First is considered only interaction with the first pulse (from the first beam), which is then followed by subsequent relaxation.

Next is evaluated interaction with the second pulse (from the counter-propagating beam), with subsequent atomic relaxation. These steps are repeated with a pulse repetition period until a steady state is reached. An example of the time evolution of the excited state is presented in Fig. 2.8.

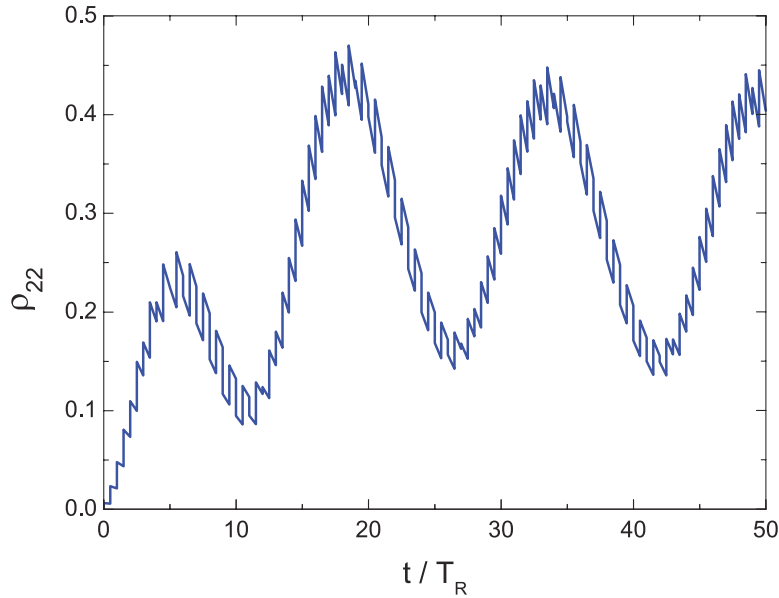


Figure 2.8: An example of the time evolution of the excited state population of a two-level atom excited by two counter-propagating beams from a frequency comb. Adapted from [15].

From the solution of the OBEs, radiation pressure force can be calculated. It is calculated using the Ehrenfest theorem or using the excited state populations. Calculated radiation pressure force exerted on two-level atoms is presented in Fig. 2.9. The force exerted on atoms by the first beam is presented in blue color, whereas the force by the counter-propagating beam is presented in red. The total force exerted on atoms is presented in black color. For atomic velocities near zero, force is similar to the radiation force for cw excitation, Fig. 2.2. This force is responsible for the reduction of atomic velocity and temperature. From Fig. 2.9 we can see another feature of the comb excitation. The radiation force profile is periodic at higher velocities  $j\lambda f_R$ , and has the same shape as the force around  $v = 0$ .

To calculate the temperature of atoms cooled in 1D by counter-propagating pulse trains, the diffusion coefficient has been calculated [15]. From the diffusion coefficient and radiation pressure force, it has been determined that the minimum temperature the system can reach is the Doppler temperature, which is the same as in cw laser Doppler cooling.

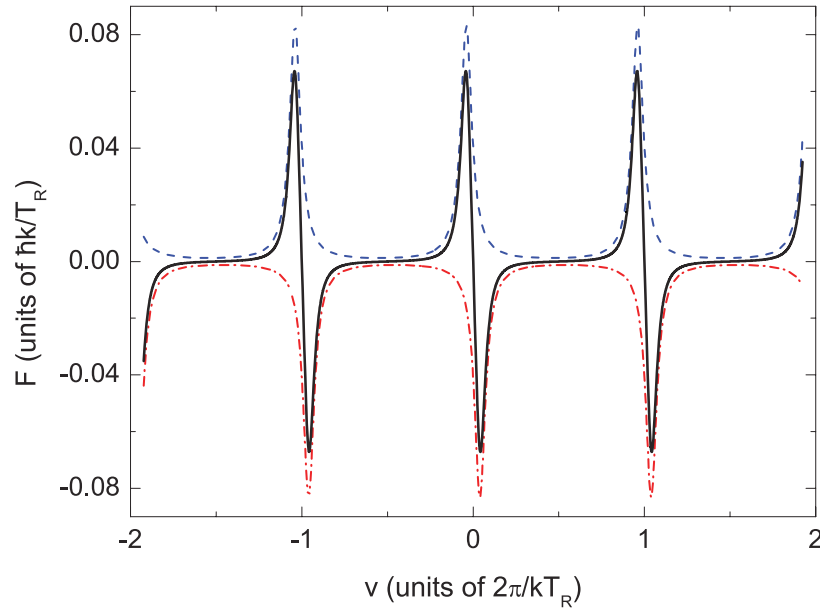


Figure 2.9: An example of the radiation pressure force from two counter-propagating pulse trains. Around  $v = 0$  radiation pressure force is similar to the cw radiation pressure force. Due to the comb structure, the radiation force profile is repeated in periods proportional to the repetition frequency. Adapted from [15].

## Chapter 3

# Theoretical study of Doppler cooling with a FC

Interaction of atoms with a frequency comb is very complex due to the complexity of an atom's energy level structure and the spectrum of a frequency comb. In this situation, many comb modes can be simultaneously resonant or near-resonant with atomic transitions. Some of these excitations can be beneficial for laser cooling, but some can hinder the laser cooling process. It is therefore crucial to well understand the influence of the comb parameters on the FC cooling process.

We developed a theoretical model of the 1D interaction of two counter-propagating pulse trains with a six-level atom. Our case study has been done for  $^{87}\text{Rb}$  atom, but can be easily adapted for any alkali atom, since they all have only one valence electron, and share similar energy level structure.

Using the Optical Bloch equations we calculate the time dynamics of the populations and the coherence terms of a density matrix. After stationary state is achieved, we calculate the radiation pressure force exerted on atoms and the diffusion coefficient. We then use Fokker-Planck equation to calculate the temperature of atoms, based on the calculated force and diffusion terms.

### 3.1 Comb-atom interaction

In our model, we use six-level atoms which we model after the  $^{87}\text{Rb}$  hyperfine energy level structure for  $D_2$  transition. Atoms are interacting with two counter-propagating pulse trains in one dimension  $z$ . We describe our system with the Hamiltonian  $\hat{H} = \hat{H}_0 + \hat{H}_{int}$ , where  $\hat{H}_0$  describes Hamiltonian of a free atom, and  $\hat{H}_{int}$  describes the interaction Hamiltonian. The

interaction part describes the interaction of atoms with an electric field  $\mathbf{E}(z, t)$  and is defined as:

$$(H_{int})_{nm} = -\boldsymbol{\mu}_{nm} \cdot \mathbf{E}(z, t), \quad (3.1)$$

where  $\boldsymbol{\mu}_{nm}$  is the transition dipole moment. Subscripts  $n$  and  $m$  refer to the hyperfine levels.

We use the density matrix formalism, where the time evolution of the density matrix is described with the von-Neumann equation:

$$\frac{\partial \rho_{nm}}{\partial t} = -\frac{i}{\hbar} [\hat{H}, \hat{\rho}]_{nm} + (\hat{\Gamma} \hat{\rho})_{nm}. \quad (3.2)$$

This equation is describing the time evolution of the density matrix elements, and for pure states it is equivalent to the Schrödinger equation. The advantage of the density matrix formalism is that Von Neumann equation can also describe time evolution of the mixed states, while Schrödinger equation can not. In the Eq. (3.2) last term was added *by hand* and it describes the spontaneous emission. These terms are defined as:

$$\langle F_e | \hat{\Gamma} \hat{\rho} | F_e \rangle = -\Gamma \langle F_e | \hat{\rho} | F_e \rangle, \quad (3.3a)$$

$$\langle F_e | \hat{\Gamma} \hat{\rho} | F_g \rangle = -\frac{\Gamma}{2} \langle F_e | \hat{\rho} | F_g \rangle, \quad (3.3b)$$

where  $\Gamma$  is the spontaneous emission rate of the excited state. We use the rotating-wave approximation to eliminate the fast oscillating terms by introducing the slowly varying envelope of the coherence terms  $\sigma_{nm} = \rho_{nm} e^{-i\omega_L t}$ , where  $\omega_L$  is the central wavelength of the laser.

The electric field in the model is defined as:

$$\mathbf{E}(z, t) = \tilde{\mathbf{E}}(z, t) e^{i\omega_L t} + c.c. \quad (3.4)$$

In the  $\tilde{\mathbf{E}}(z, t)$  we included the electric fields of two counter-propagating laser beams from a mode-locked laser as:

$$\tilde{\mathbf{E}}(z, t) = \mathcal{E}(t) e^{-ikz} + \mathcal{E}'(t) e^{ikz}. \quad (3.5)$$

Terms  $\mathcal{E}(t)$  and  $\mathcal{E}'(t)$  describe two counter-propagating pulse trains emerging from the same

laser, with a delay time  $\tau$  at  $z = 0$ :

$$\begin{aligned}\mathcal{E}(t) &= \sum_{n=0}^{\infty} \mathcal{E}_0(t - z/c - nT_R) e^{in\Phi_R}, \\ \mathcal{E}'(t) &= \sum_{n=0}^{\infty} \mathcal{E}_0(t - \tau + z/c - nT_R) e^{in\Phi_R}.\end{aligned}\tag{3.6}$$

These two pulse trains are propagating towards  $+z$  and  $-z$  directions. Pulses are repeated with a repetition period of  $T_R$  and the phase shift between two consecutive pulses is  $\Phi_R$ . Single pulse envelope is defined as  $\mathcal{E}_0(t) = E e^{-t^2/\tau_P^2}$ , where  $\tau_P$  is the parameter defining the pulse duration and  $E$  is the pulse amplitude.

The spectrum of a pulse train  $\mathcal{E}(t)$  is called a frequency comb and consists of many equidistant and narrow spectral modes. These modes are centered around  $\omega_L + \Phi_R/T_R$ , and the distance between them is the repetition frequency defined as  $f_{rep} = 1/T_R$ . These parameters define the whole comb spectrum so the frequency of the  $n$ -th comb mode is:

$$\omega_n = \left( \omega_L + \frac{\Phi_R}{T_R} \right) \pm \frac{2\pi n}{T_R}.\tag{3.7}$$

From this equation, we see that three parameters change the spectrum of a frequency comb,  $\omega_L$ ,  $\Phi_R$  and  $T_R$ . In the view of resonant excitation with a frequency comb, change of  $\omega_L$  and  $\Phi_R$  has the same effect on the population and coherence terms of a density matrix [48, 49]. Change of the  $T_R$  directly changes the spacing between the comb modes and greatly changes the relative detunings of the comb modes with respect to the atomic transitions.

### 3.1.1 The influence of comb parameters on FC laser cooling

We will study three cases of interaction of two counter-propagating pulse trains with  $^{87}\text{Rb}$  atoms in 1D geometry. These three cases are examples of a *good* and *bad* case, and a case with comb parameters that we have available experimentally. Relative positions of comb modes for three discussed cases of comb parameters with respect to the atomic transitions are presented in Fig. 3.1.

The first case we discuss here is the case that leads to effective laser cooling. Relative positions of the comb modes with respect to the atomic transitions are presented in Fig. 3.1(a). Repetition frequency for which it is achieved is  $f_{rep} = 187.82$  MHz. We tune the FC spectrum so the  $n$ -th comb mode is  $-\Gamma$  detuned from the  $|F = 2\rangle \rightarrow |F' = 3\rangle$ , the cooling transition for  $^{87}\text{Rb}$  atoms. For the  $^{87}\text{Rb}$  atoms,  $\Gamma \approx (2\pi \cdot) 6$  MHz [39] is the decay rate for  $5^2S_{1/2} \rightarrow 5^2P_{3/2}$

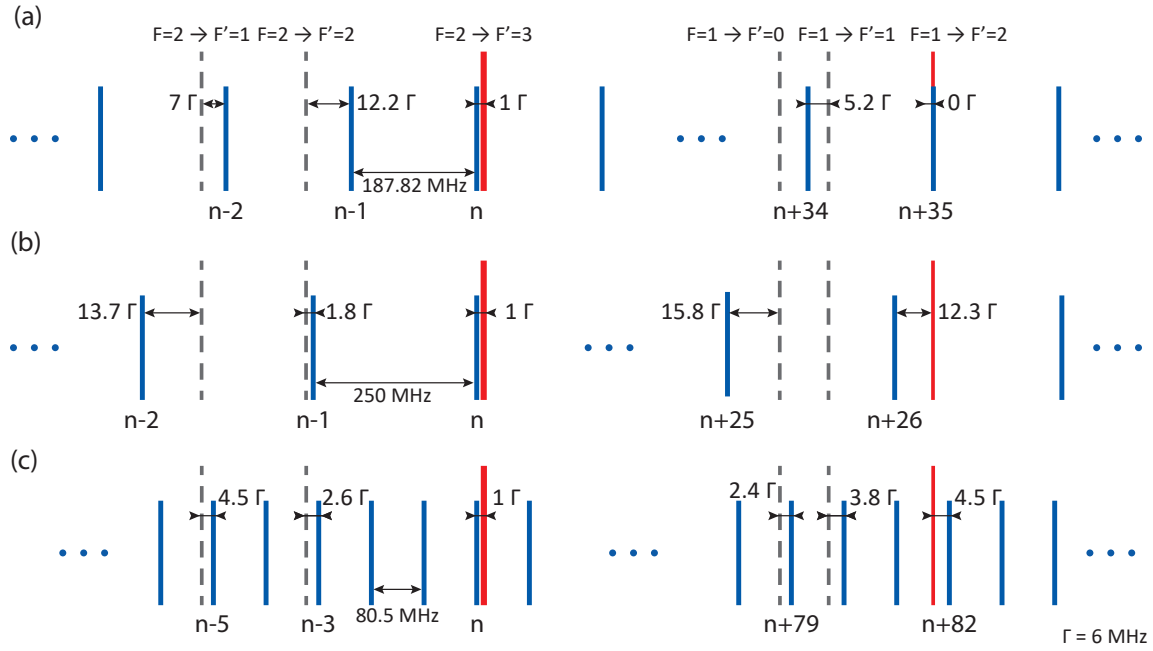


Figure 3.1: Relative positions of the comb modes with respect to the atomic transitions in  $^{87}\text{Rb}$  for three sets of FC parameters. (a) The repetition frequency of 187.82 MHz, where simultaneous excitation of the cooling and repumping transitions with  $n$ -th and  $(n+35)$ -th comb modes leads to effective laser cooling. (b) Repetition frequency of 250 MHz, where the cooling transition and  $|F=2\rangle \rightarrow |F'=2\rangle$  transition are excited with  $n$ -th and  $(n-1)$ -st comb mode, respectively. This set of comb parameters does not lead to effective laser cooling due to the optical pumping into  $|F=1\rangle$  ground state. (c) Repetition frequency of 80.5 MHz, which is available in the experiment. For this set, only the cooling transition is excited with  $n$ -th comb mode and partial optical pumping into  $|F=1\rangle$  ground state is preventing optimal laser cooling.

transition. In the standard laser cooling with continuous-wave lasers, it is usual to tune the laser to be  $-\Gamma$  detuned with respect to the cooling transition since it leads to the reduction of the atom's velocity, and thus the temperature.

To keep the atoms in the cooling cycle, it is necessary to repump the atoms from the ground state  $|F=1\rangle$ . In this case,  $(n+35)$ -th comb mode is resonant with the  $|F=1\rangle \rightarrow |F'=2\rangle$  transition, the repumping transition for  $^{87}\text{Rb}$  atoms. Here almost all population in the  $|F=1\rangle$  ground state is optically pumped into the  $|F=2\rangle$  ground state. This enables the efficient cooling of atoms while keeping the majority of the atoms in the cooling cycle. Other comb modes are far detuned from other transitions in the  $^{87}\text{Rb}$  atoms and have no significant effect on the cooling process.

In the second case, we have a very different situation. Repetition frequency is 250 MHz, and relative positions of the comb modes with respect to the atomic transitions are presented in

Fig. 3.1(b). Here we again tune the comb spectrum so the  $n$ -th comb mode is  $-\Gamma$  detuned from the cooling transitions of the  $^{87}\text{Rb}$  atoms.

The notable contribution to the force and cooling process comes from the interaction of the  $(n - 1)$ -st comb mode with the  $|F = 2\rangle \rightarrow |F' = 2\rangle$  transition. Two effects make the cooling process inefficient. Detuning of the  $(n - 1)$ -st comb mode with respect to the  $|F = 2\rangle \rightarrow |F' = 2\rangle$  transition is  $+1.8\Gamma$  so this excitation is heating the atoms instead of cooling them. Overall, the net effect is still cooling as  $|F = 2\rangle \rightarrow |F' = 3\rangle$  transition is considerably stronger, but the excitation of  $|F = 2\rangle \rightarrow |F' = 2\rangle$  transition reduces the cooling process. The second effect is the optical pumping of the population in the  $|F = 2\rangle$  ground state into the  $|F = 1\rangle$  ground state mediated by the excitation of the  $|F = 2\rangle \rightarrow |F' = 2\rangle$  transition with  $(n - 1)$ -st comb mode. This transfer of population is disabling the excitation of the cooling transition as the atoms are lost from the cooling cycle. This effect can be balanced when another comb mode is driving the repumping transition, like in the first case that we considered. Here, however, this is not the case, and FC cooling with these parameters is inefficient.

Last case we discuss is the repetition frequency of 80.5 MHz, which we have available in the lab. This is the case presented in the Fig. 3.1(c). Once again we tune the comb so that the  $n$ -th comb mode is  $-\Gamma$  detuned with respect to the cooling transition in  $^{87}\text{Rb}$  atoms. As it can be seen, for these comb parameters this is the only comb mode that is close to the resonance with atomic transitions. Here we do not achieve optimal laser cooling since the comb modes are detuned from repumping transitions, thus not recycling the atoms into the cooling cycle.

In this qualitative analysis, we considered three sets of comb parameters, one that leads to efficient laser cooling, one that does not, and one sub-optimal case. Tuning range of the repetition frequency in experiments is typically quite narrow. Often it can be tuned for only a few hundreds of kHz. Due to this frequency combs that are optimal for laser cooling have to be custom-built, where the optimal repetition frequency has to be chosen based on the analysis similar to the one presented here, and taking into account the properties of the atom of interest.

### 3.2 Temporal evolution of the density matrix elements

A frequency comb is the spectrum of a mode-locked pico- or femtosecond pulsed laser. Pulses duration from such lasers  $\tau_P$  is much smaller than the atom's excited state lifetime  $\Gamma^{-1}$  and the pulse repetition period  $T_R$ . With these assumptions, we solve Eq. (3.2) in four steps, presented in Fig. 3.2

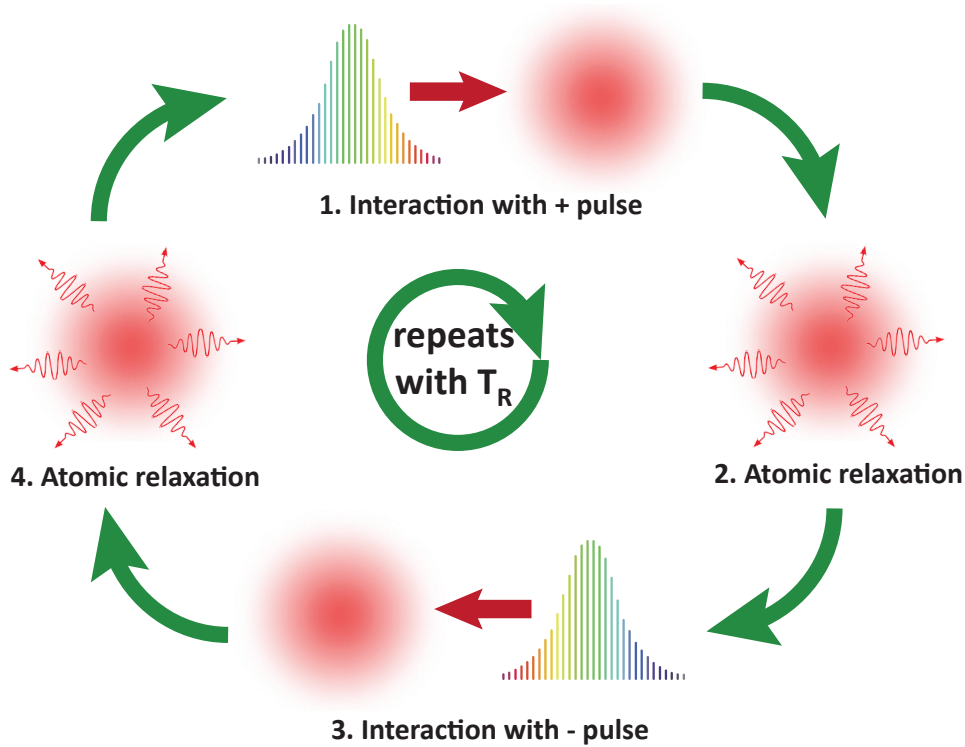


Figure 3.2: Temporal evolution of the density matrix elements is calculated in four steps: 1. interaction with '+' pulse; 2. atomic relaxation; 3. interaction with '-' pulse; 4. atomic relaxation. This process is repeated with a period of  $T_R$  until a stationary state of the density matrix elements is achieved.

In the first step, we include only interaction with the first pulse. This is the pulse that propagates towards  $+z$  direction, and we call it a '+' pulse. The second step is the calculation of subsequent atomic relaxation from the excited state. The next step is the interaction with the second pulse. This pulse is propagating towards  $-z$  direction and is called a '-' pulse. This pulse is delayed from the first pulse by  $\tau < T_R$ . The final step is the calculation of the atomic relaxation from the excited state.

These steps are periodic in time, with the period being the repetition period  $T_R$ . The procedure is repeated until density matrix elements reach a stationary state. The usual way of solving this problem for two-level atoms is by using the impulse approximation. Since pulse duration is

much shorter than the other characteristic times in the system, pulsed excitation is approximated to be instantaneous, where the pulse area is the parameter that describes the laser pulse [48]. The problem can then be solved analytically, using the iterative pulse-by-pulse procedure.

In our model we consider six-level atoms, so the use of the impulse approximation will not lead to a practical analytical solution. Instead, we solve the problem numerically, using the described time intervals that are repeated until the system reaches a stationary state. The initial conditions we use in all work done are:

$$\begin{aligned}\rho_{11} &= 3/8, & \rho_{22} &= 5/8, \\ \rho_{33} &= \rho_{44} = \rho_{55} = \rho_{66} = 0, \\ \rho_{ij} &= 0 \quad \text{for } i \neq j.\end{aligned}\tag{3.8}$$

Here  $\rho_{11}$  and  $\rho_{22}$  represent the populations of the  $|F = 1\rangle$  and  $|F = 2\rangle$  ground levels, while  $\rho_{33}$ ,  $\rho_{44}$ ,  $\rho_{55}$  and  $\rho_{66}$  represent the populations of the  $|F' = 0, 1, 2, 3\rangle$  excited levels, respectively. Off-diagonal terms  $\rho_{ij}$  are coherences between respective levels. The detuning is defined as the difference between the central laser frequency and the frequency of the cooling transition of the  $^{87}\text{Rb}$  atoms  $|F = 2\rangle \rightarrow |F' = 3\rangle$ :

$$\delta = \omega_L - \omega_{26}.\tag{3.9}$$

In the model atoms have velocity  $\mathbf{v}$ , so density matrix elements are dependent on the Doppler shifted laser frequency  $\omega'_L = \omega_L - \mathbf{k} \cdot \mathbf{v}$ .

Temporal evolution of the excited state populations of  $^{87}\text{Rb}$  atom is presented in Fig. 3.3. Here pulses are delayed by  $\tau = T_R/2$  and other parameters used in the calculation are:  $f_{rep} = 187.82$  MHz,  $\Phi_R = 0$ ,  $\tau_P = 80$  fs,  $\delta = -\Gamma$ ,  $v = 0.1$  m/s,  $E = 4.3 \times 10^5$  V/m.

In this figure, there is presented the time evolution for populations of the hyperfine levels of the excited states. Here we present the effect of the first few pulses on the populations, at the beginning of the calculation, to demonstrate the effect of the four time intervals that calculation is performed with. Since repetition period of the pulses is smaller than the excited state lifetime  $\Gamma^{-1} \approx 26$  ns [39], population is coherently accumulated. Populations of  $\rho_{33}$ ,  $\rho_{44}$  and  $\rho_{55}$  are multiplied by factors of 100, 30 and 50, respectively, so the time evolution is visible in the figure.

The delay between two consecutive pulses can be changed, and it has an effect on the time dynamics on the short scale, as presented in Fig. 3.4. When the stationary state is reached, final populations are very similar for different pulse delays.

After interaction with many pulses, density matrix elements reach the stationary state, as

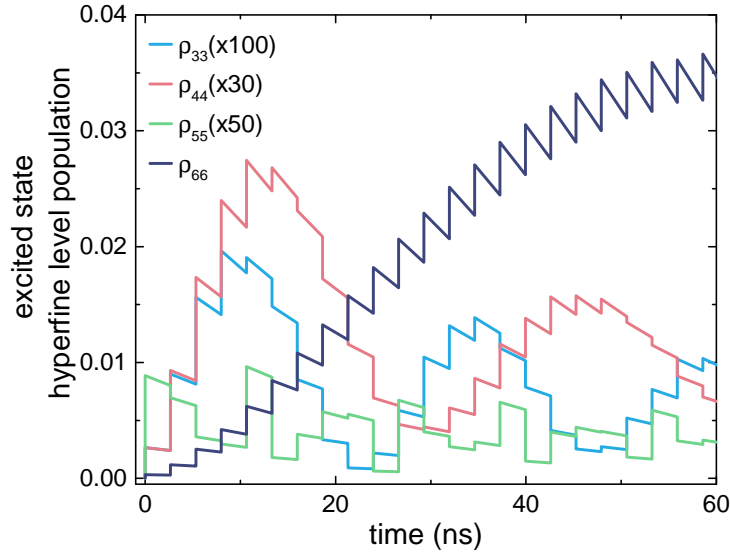


Figure 3.3: Transient temporal evolution of the excited state populations.  $\rho_{33}$ ,  $\rho_{44}$  and  $\rho_{55}$  are multiplied by factors 100, 30 and 50, respectively for visual clarity. The delay between two consecutive pulses is  $\tau = T_R/2$  and other calculation parameters are:  $f_{rep} = 187.82$  MHz,  $\Phi_R = 0$ ,  $\tau_P = 80$  fs,  $\delta = -\Gamma$ ,  $v = 0.1$  m/s,  $E = 4.3 \times 10^5$  V/m

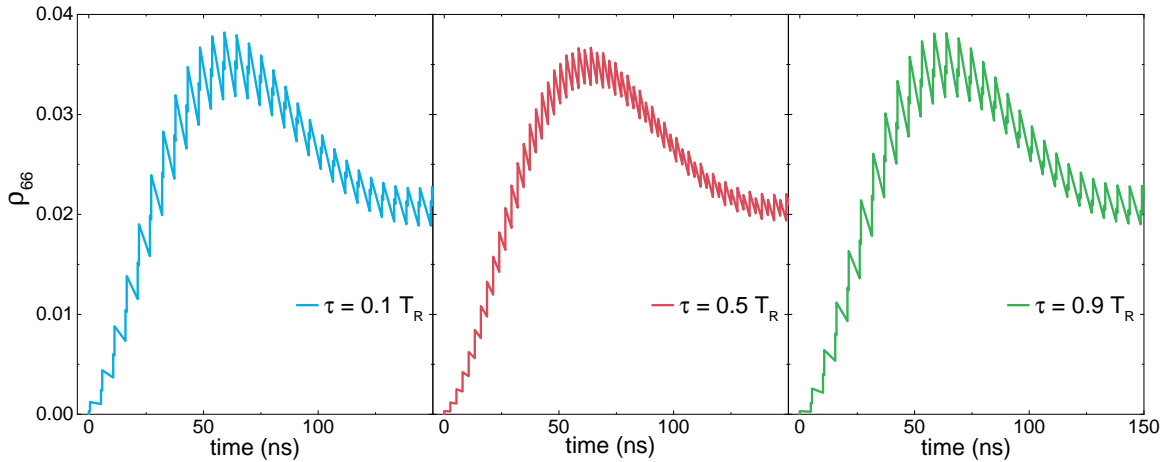


Figure 3.4: Effect of the pulse delay on the temporal evolution of the density matrix elements. Other parameters used in the calculations are the same as in Fig. 3.3.

seen in Fig. 3.5. The results for three sets of comb parameters (discussed in the previous section) are shown, the repetition frequencies of 187.82 MHz, 250 MHz and 80.5 MHz, and detuning of  $\delta = -\Gamma$ . Parameters used in the calculations are:  $E = 4.3 \times 10^5$  V/m for  $f_{rep} = 187.82$  MHz,  $E = 3.2 \times 10^5$  V/m for  $f_{rep} = 250$  MHz and  $E = 10^6$  V/m for  $f_{rep} = 80.5$  MHz,  $\Phi_R = 0$ ,  $\tau_P = 80$  fs,  $\delta = -\Gamma$ ,  $v = 0.1$  m/s. Here we scale the electric field amplitude

so the intensity per comb mode for different repetition frequencies is the same. Intensity per comb mode is calculated using the expression  $I_{CM} \approx I_{avg} \tau_P / T_R$  [15], where  $I_{avg}$  is the time-averaged intensity of a pulse train. Using the relation between average and peak power of the pulse  $I_{avg} \sim I_{peak} \tau_P / T_R$ , and the relation between intensity and electric field amplitude  $I \sim E^2$ , scaling of the electric field amplitude for different repetition periods is calculated using the expression  $E_1 / E_2 = T_{R,2} / T_{R,1}$ .

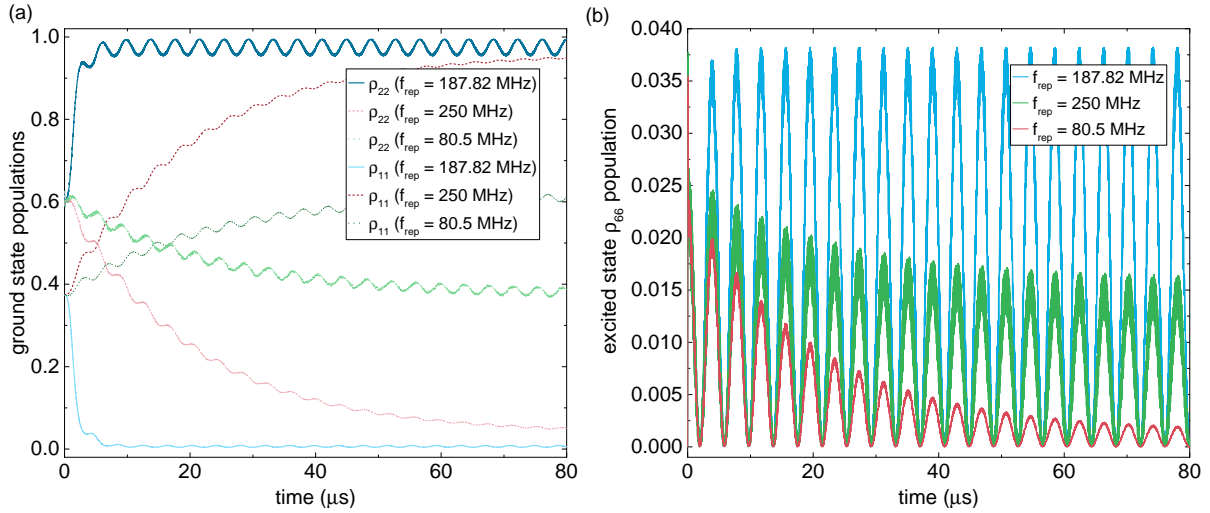


Figure 3.5: Stationary state populations of the (a) ground state hyperfine levels and (b)  $\rho_{66}$  level for three sets of comb parameters discussed. Parameters used:  $E = 4.3 \times 10^5$  V/m for  $f_{rep} = 187.82$  MHz,  $E = 3.2 \times 10^5$  V/m for  $f_{rep} = 250$  MHz and  $E = 10^6$  V/m for  $f_{rep} = 80.5$  MHz,  $\delta = -\Gamma$ ,  $\Phi_R = 0$ ,  $\tau_P = 80$  fs,  $\delta = -\Gamma$ ,  $v = 0.1$  m/s.

In the Fig. 3.5(a) we see the effect of the optical pumping process we discussed in the previous section. For the repetition frequency 187.82 MHz we see that almost all population is optically pumped into the  $|F = 2\rangle$  ground state. In the Fig. 3.5(b) we see the effect on the  $\rho_{66}$  population. On the contrary, for the repetition of 250 MHz, almost all population is pumped into the  $|F = 1\rangle$  ground level, and as a consequence, the excitation of the cooling transition is reduced. In the case of repetition of 80.5 MHz there is a partial transfer of population from the  $|F = 2\rangle$  into the  $|F = 1\rangle$  ground level, so the cooling transition is excited sub-optimally.

Oscillations of the level populations are observed in Fig. 3.5. This is happening due to the atom moving in the spatially varying electric field from two counter-propagating pulse trains. The period of these oscillations is  $\pi / (kv)$ , where  $k$  is the transition wavevector and  $v$  is the velocity of the atom. This effect is also happening for the excitation with cw lasers, where electric fields of two counter-propagating beams form the standing wave.

### 3.3 Radiation pressure force and diffusion coefficient

In laser cooling of atoms the velocity of the atoms interacting with laser beams is reduced. The reduction of the atomic velocity is a consequence of the radiation pressure force exerted on the atoms by the laser beams. The force exerted on atoms is calculated from the stationary state solution of the density matrix elements, using the Ehrenfest theorem. It is defined as [33]:

$$\mathbf{F} = \langle -\nabla_z \hat{H} \rangle = -\text{Tr} \left( \hat{\rho} \nabla_z \hat{H} \right), \quad (3.10)$$

where  $\nabla_z = \hat{\mathbf{z}} \partial / \partial z$ . This is the quantum mechanical analogue of the classical expression that the force is the negative gradient of the potential. Calculation of the radiation pressure force using the Eq. (3.10) requires direct integration over the duration of the individual laser pulses.

In the case that delay between two consecutive pulses is much longer than the pulse duration,  $\tau \gg \tau_P$ , and when the excited state lifetime is much longer than the pulse duration  $\Gamma^{-1} \gg \tau_P$ , the radiation pressure force can be calculated iteratively. This alternative way of calculating force is more practical (numerically much less demanding) since it uses already calculated density matrix elements, instead of numerical integration.

Change of the atomic momentum due to the pulsed excitation is proportional to the change in the excited state population [47]:

$$\partial \mathbf{p} = (\partial \rho_{ee}) \hbar \mathbf{k}. \quad (3.11)$$

Change in the excited state populations is the difference between the excited state population just after the excitation pulse and the population just before the pulse. The net contribution from the spontaneous emission is zero since it is in a random direction. The total time-averaged radiation pressure force exerted on the atoms due to the pulsed excitation is:

$$F = \frac{\hbar k}{T_R} \sum_e (\rho_{ee}^{p+} - \rho_{ee}^{n+}) - (\rho_{ee}^{p-} - \rho_{ee}^{n-}). \quad (3.12)$$

In this expression  $\rho_{ee}^{n\pm}$  is the population of the excited state  $e$  just before excitation with the  $n$ -th '+' or '-' pulse (pulses that are propagating towards  $+z$  or  $-z$  direction), and  $\rho_{ee}^{p\pm}$  is the population of the excited state  $e$  just after excitation with the  $n$ -th '+' or '-' pulse.

To confirm the validity of the radiation pressure force expression Eq. (3.12) with the result of the Eq. (3.10), we checked two values for exerted force and under the mentioned conditions they match within satisfactory precision. Due to the much lower computational time needed to calculate the radiation pressure force, the results in this work are calculated using the iterative

expression Eq. (3.12).

The radiation pressure forces for three pulse repetition frequencies discussed in the previous sections, as a function of atomic velocity is presented in Fig. 3.6.

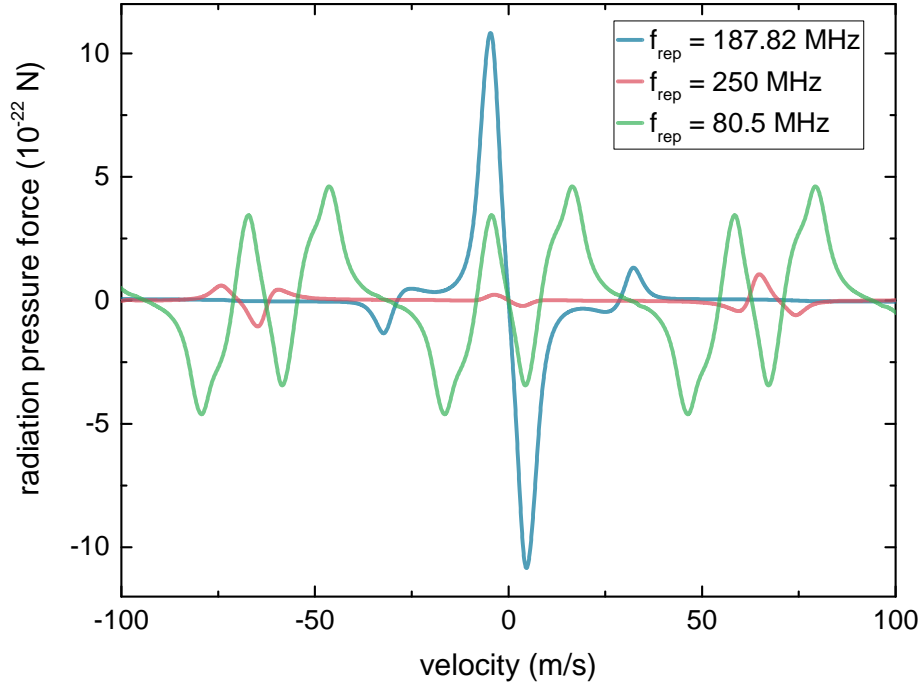


Figure 3.6: Radiation pressure force as a function of atomic velocity for three sets of comb parameters, illustrated in Fig. 3.1. Calculation parameters are the same as in Fig. 3.5.

When the atom undergoes spontaneous emission, it experiences the change of momentum in finite steps of  $\hbar k$ . Atom's momentum can be related with *random walk*, where randomness is a consequence of the spontaneous emission. It can be shown that the atom's momentum distribution in standard continuous-wave laser cooling can be expanded into two terms, one that describes the drift, and the other that describes the diffusion [33]. In the stationary state, in the case of Doppler cooling, the momentum distribution is the Maxwell-Boltzmann distribution, where the minimum temperature is Doppler limit temperature  $k_B T = \hbar \gamma / 2$ .

In this work, we calculate the diffusion coefficient iteratively, in a similar way to how radiation force terms are calculated. Diffusion is proportional to the change in the excited state populations due to the spontaneous emission:

$$D = \frac{(\hbar k)^2}{T_R} \sum_e (\rho_{ee}^{p+} - \rho_{ee}^{n-}) + (\rho_{ee}^{p-} - \rho_{ee}^{(n+1)+}). \quad (3.13)$$

In this expression, the first term is describing the diffusion contribution from the spontaneous emission following the excitation by the  $n$ -th '+' pulse, and the second term is describing the contribution from the spontaneous emission following the excitation by the  $n$ -th '-' pulse'. In Fig. 3.7 we present the diffusion coefficient as a function of atomic velocity for three different pulse repetition frequencies discussed in previous sections.

As a consequence of the atoms moving with velocity  $v$ , radiation pressure force and diffusion coefficient are functions of the atomic velocity  $v$ .

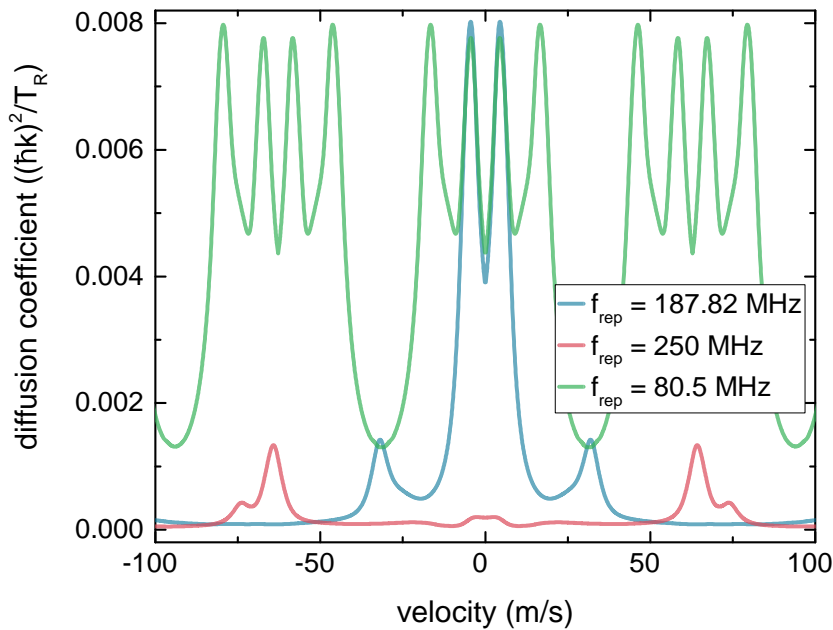


Figure 3.7: Diffusion coefficient as a function of atomic velocity for three different sets of comb parameters, as illustrated in Fig. 3.1. Calculation parameters are the same as in Fig. 3.5.

In the figures 3.6 and 3.7 we presented the radiation pressure force and diffusion coefficient as functions of atomic velocity. Parameters used in calculations are:  $f_{rep} = 187.82$  MHz and  $E = 4.3 \times 10^5$  V/m,  $f_{rep} = 250$  MHz and  $E = 3.2 \times 10^5$  V/m,  $f_{rep} = 80.5$  MHz and  $E = 10^6$  V/m. We scaled the electric field amplitude with the repetition rate so that the power per comb mode is constant for all repetitions. Other parameters used are:  $\Phi_R = 0$ ,  $\tau_P = 80$  fs,  $\delta = -\Gamma$  and  $\tau = T_R/2$ .

For the case of repetition of 80.5 MHz it is visible that the force and diffusion are periodic functions of atomic velocity, where the period is equal to  $\lambda f_{rep}$ . For two other repetitions, force and diffusion are also periodic, but due to the repetition frequency and scale of the figures, this

is not visible.

We setup the comb parameters so that a comb mode is  $-\Gamma$  detuned from the cooling transition, so the slope of the radiation pressure force in Fig. 3.6 is negative for all repetitions. For the cooling of atoms, only the force around  $v = 0$  is important, since faster atoms can not be captured in a trap. There is a big difference between the slope and the maximum of the force exerted on atoms around  $v = 0$  for three sets of comb parameters discussed.

From the three cases, the radiation force exerted on atoms at the repetition of 250 MHz is the smallest. This is the direct consequence of a comb mode being  $1.8\Gamma$  blue detuned from the  $|F = 2\rangle \rightarrow |F' = 2\rangle$  transition. Almost all of the population in the ground level  $|F = 2\rangle$  is optically pumped into the  $|F = 1\rangle$  ground level and therefore the cooling transition can not be excited efficiently. Effects of other comb modes that are far detuned from their respective transitions are visible at higher velocities.

In the case of repetition frequency of 80.5 MHz, the radiation force is bigger and it has a steeper slope in comparison to the force at the repetition of 250 MHz. This is a consequence of the partial transfer of the population from the ground level  $|F = 2\rangle$  into the  $|F = 1\rangle$  ground level. Here the cooling comb mode will still drive the cooling transition, but it will not be optimal. The radiation pressure force exhibits a rather complex behavior as atomic velocity is changed since several hyperfine transitions are close to resonance with respect to respective comb modes.

This two discussed cases of comb-atom excitation are not very efficient for laser cooling. A lot of the population is in the dark state for the cooling comb mode that is  $-\Gamma$  detuned from the cooling transition. For FC cooling at these repetitions, an additional repumping laser is necessary. To emulate this, we present the case of comb-atom excitation at the repetition frequency of 187.82 MHz. For this repetition frequency when the  $n$ -th (cooling) comb mode is  $-\Gamma$  detuned from the cooling transition, the  $(n + 35)$ -th comb mode is resonant with  $|F = 1\rangle \rightarrow |F' = 2\rangle$  transition, the repumping transition.

In Fig. 3.6 it is clear that the force is larger and the slope of the force is steeper for the repetition frequency 187.82 MHz, in comparison to the other two repetitions. This case is analogous to the standard continuous wave laser cooling, where cooling and repumping lasers are required. Here the population from the  $|F = 1\rangle$  level is optically pumped into the  $|F = 2\rangle$  level by the  $(n + 35)$ -th comb mode excitation (the repumping comb mode), so the  $n$ -th comb mode can drive the cooling transition optimally, and the cooling process is efficient.

We have tested different repetition rates around 187.82 MHz, while we fixed the detuning of the  $n$ -th comb mode from the cooling transition to  $-\Gamma$  detuning. With a slight change in the repetition frequency, relative positions of the comb modes with respect to transitions from the

$|F = 2\rangle$  level do not change significantly, but the change with respect to the transitions from the  $|F = 1\rangle$  level is significantly larger. For example, change of the repetition frequency of 0.1 MHz results in change of detuning for the  $|F = 2\rangle$  levels around  $0.02\Gamma$ , while the change of detuning for  $|F = 1\rangle$  levels is around  $0.6\Gamma$ . From these results we can conclude that the respective comb mode can be near-resonant with the repumping transition, within about  $\pm 3\Gamma$  without a significant change in the radiation pressure force and diffusion coefficient. As this is not the only repetition where this condition can be satisfied, we provide the expression for the repetition frequencies that are recommended for efficient frequency comb cooling of atoms:

$$\Delta - 3\Gamma \lesssim N \cdot f_{rep} \lesssim \Delta + 3\Gamma, \quad (3.14)$$

where  $\Delta = |f_{cooling} - f_{repumping}|$  is the frequency difference between the cooling and repumping transition of the respective atom,  $\Gamma$  is the excited state decay rate and  $N$  is an integer. In the case that the repetition frequency is comparable to the excited state decay rate, multiple comb modes can be near-resonant with the atomic transitions simultaneously and then the situation is very complex and requires deeper analysis. When Eq. (3.14) is applied, special care has to be taken so there are no comb modes near resonant with transitions that allows atoms to leave cooling cycle, for example, repetition frequency 250 MHz, where comb mode is near resonant with  $|F = 2\rangle \rightarrow |F' = 2\rangle$ . In that case detuning of the repumping comb mode has to be adjusted so it overcomes the effects of the unwanted excitation.

### 3.4 1D laser cooling with a Frequency comb

Radiation pressure force and the diffusion coefficient can give us information about the temperature of atoms interacting with two counter-propagating pulse trains. The temperature is calculated using the Fokker-Planck equation [33]

$$\frac{\partial \rho(v, t)}{\partial t} = -\frac{1}{m} \frac{\partial}{\partial v} [F(v) \rho(v, t)] + \frac{1}{m^2} \frac{\partial^2}{\partial v^2} [D(v) \rho(v, t)], \quad (3.15)$$

where  $m$  is the mass of an atom. Using the calculated radiation pressure force and diffusion coefficient, the Fokker-Planck equation is solved numerically. The solution is the time evolution of the atomic velocity distribution  $\rho(v, t)$ , from which we can calculate the temperature of atoms. The initial condition for the work done here is an atomic velocity distribution that corresponds to the temperature of 2.6 mK, well above the Doppler limit temperature. The stationary state temperature is same for different initial temperature, but for higher temperature

it takes longer time to reach stationary state, and thus computational time is increased. One dimensional atomic velocity distribution is Maxwell-Boltzmann distribution [33]

$$\rho(v) = \frac{1}{\sqrt{2\pi}\tilde{v}} \exp\left(-\frac{v^2}{2\tilde{v}^2}\right). \quad (3.16)$$

Here  $\tilde{v}$  has the meaning of the width of the distribution and is connected to the temperature of atoms by the means of the equipartition theorem:

$$\tilde{v} = \sqrt{\frac{k_B T}{m}}, \quad (3.17)$$

where  $k_B$  is the Boltzmann constant,  $m$  is the mass of an atom, and  $T$  is the temperature of the atoms. Fig. 3.8 presents the atomic distributions of atoms at the temperatures of 2.6 mK, used as the initial condition for the numerical calculations of the Fokker-Planck equation, Eq. (3.15), and the calculated steady state atomic distribution. The obtained distribution corresponds to the temperature of 185  $\mu$ K, the usual temperature of atoms achieved with laser cooling. Comb parameters used for the calculation of the temperatures are  $f_{rep} = 187.82$  MHz,  $E = 4.3 \times 10^5$  V/m,  $\Phi_R = 0$ ,  $\tau_P = 80$  fs,  $\delta = -\Gamma$ .

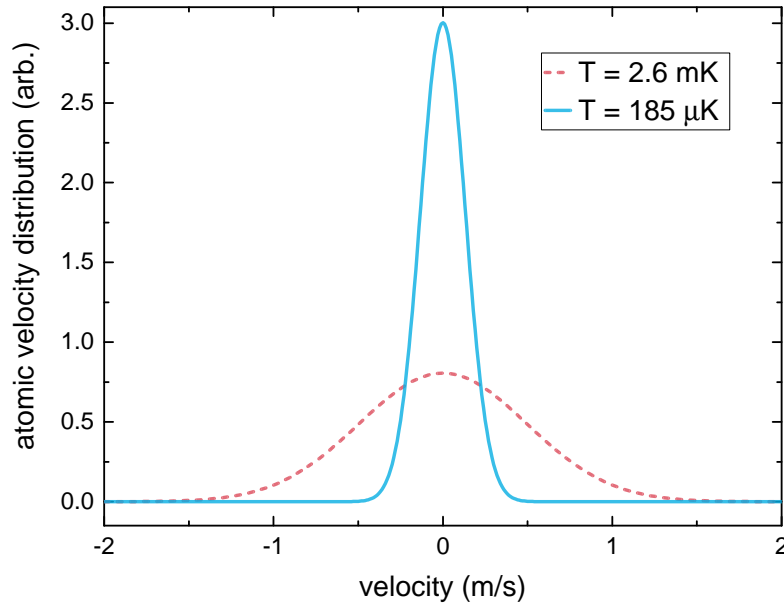


Figure 3.8: Atomic velocity distribution in 1D for two temperatures. Dashed red line presents the distribution that corresponds to the temperature of 2.6 mK, and the solid blue line the distribution that corresponds to the temperature of 185  $\mu$ K.

To calculate the temperature of the atoms interacting with two counter-propagating pulse trains we solve the Eq. (3.2) for a set of comb parameters. From the stationary state solution for the density matrix elements the radiation pressure force, Eq. (3.12), and diffusion coefficient, Eq. (3.13) are calculated. These two functions of velocity are then used in the Fokker-Planck equation, Eq. (3.15) to get the information about the temperature of atoms.

The Fokker-Planck equation is solved numerically, until the atomic velocity distribution reaches a stationary state. An example of the time evolution of the atomic velocity distribution is presented in Fig. 3.9. Comb parameters used for the calculation of the temperatures are  $f_{rep} = 187.82$  MHz,  $E = 4.3 \times 10^5$  V/m,  $\Phi_R = 0$ ,  $\tau_P = 80$  fs,  $\delta = -\Gamma$ . From the stationary state atomic velocity distribution, we calculate its width, and from width the temperature of atoms.

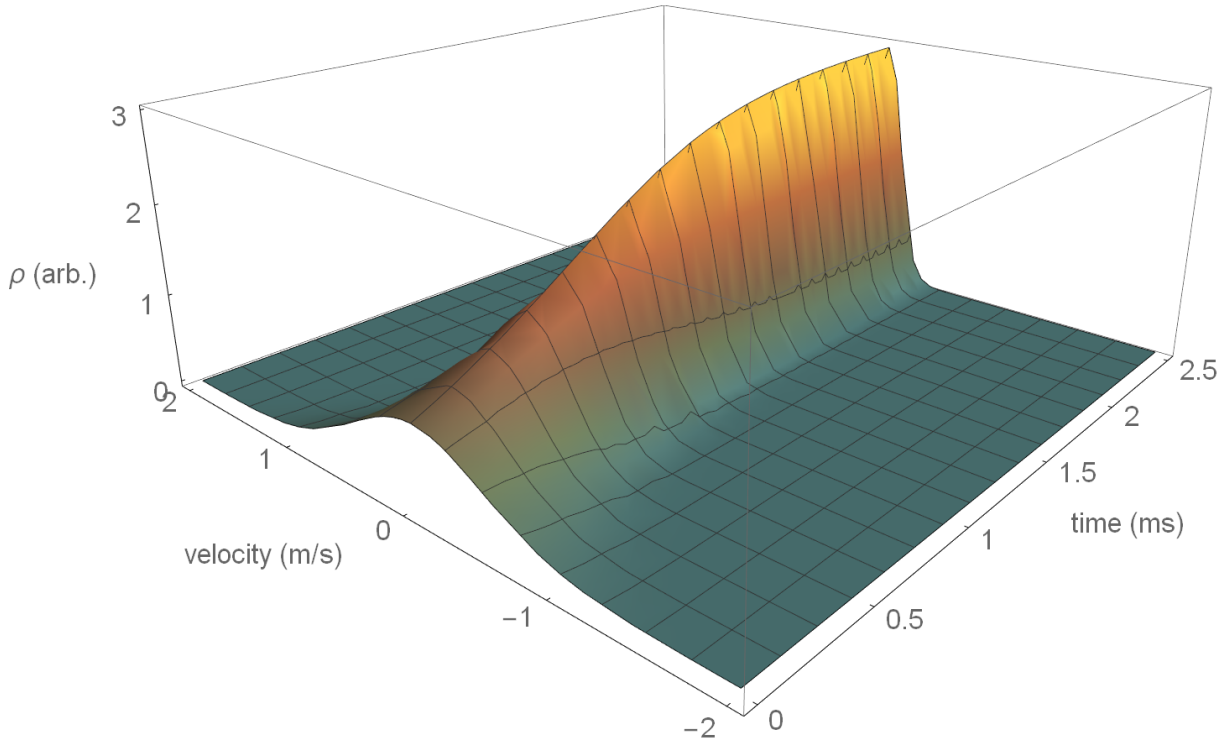


Figure 3.9: Time evolution of the atomic velocity distribution under the influence of two counter-propagating FC beams. Parameters used for calculation:  $f_{rep} = 187.82$  MHz,  $E = 4.3 \times 10^5$  V/m,  $\Phi_R = 0$ ,  $\tau_P = 80$  fs,  $\delta = -\Gamma$ .

We calculated the stationary state temperatures of the 1D frequency comb cooling for three sets of comb parameters discussed in previous sections. Calculated radiation pressure force and diffusion coefficients, presented in Figs. 3.6 and 3.7, are used as parameters in the Fokker-Planck equation. From the initial temperature of 2.6 mK, stationary state temperatures are

185  $\mu\text{K}$  for  $f_{rep} = 187.82$  MHz, 367  $\mu\text{K}$  for  $f_{rep} = 250$  MHz and 285  $\mu\text{K}$  for  $f_{rep} = 80.5$  MHz. As is expected, for repetition frequency of 187.82 MHz stationary state temperature of atoms is the lowest. It is close to the Doppler temperature and in experiments, similar temperatures are obtained. The temperature of atoms for the other two repetitions is higher but still is close to the Doppler temperature. This is also expected from the results of radiation pressure force and diffusion coefficient since all repetitions had a negative slope of the force near  $v = 0$ .

Another effect which is not described with the Fokker-Planck equation is the loss of atoms from the cooling cycle. In the Fokker-Planck equation, only the atoms that are kept in the cooling cycle are considered, assuming there is no loss of atoms in the processes of pulsed excitation. This loss of atoms is most visible in Fig. 3.5, where we observe the ground state populations time evolution.

From this analysis, we conclude that efficient laser cooling is achieved for repetition frequency of 187.82 MHz, sub-optimal cooling for repetition frequency of 80.5 MHz, and inefficient cooling for repetition frequency of 250 MHz. For these two repetitions, an additional repumping laser would be necessary to keep the atoms in the cooling cycle.

Finally, we studied how the detuning of the  $n$ -th comb mode from the cooling transition changes the temperature of atoms interacting with two counter-propagating pulse trains. Comb parameters used are  $f_{rep} = 187.657$  MHz,  $\Phi_R = 0$ ,  $\tau_P = 80$  fs and  $\tau = T_R/2$ . Here we also studied the effect of different electric field amplitudes of pulse trains, i.e. the power of the comb modes.

We choose a repetition frequency of 187.657 MHz so the detuning of the  $n$ -th comb from the cooling transition, and the detuning of the  $(n + 35)$ -th comb mode from the repumping transition is the same. Change of the detuning of repumping comb mode changes the repumping conditions, but if the detuning is inside the inequality (3.14) window, it is not significant and does not change the stationary state temperature significantly. Other comb modes are far detuned from respective transitions and have no effect on the radiation force and diffusion coefficient near  $v = 0$ . Here we calculated the radiation pressure force and diffusion coefficient for different detunings of the  $n$ -th comb mode from the cooling transition. Force and diffusion are used to calculate the temperature of atoms interacting with two counter-propagating pulse trains using the Fokker-Planck equation. Temperatures of atoms as a function of detuning are presented in Fig. 3.10 for different electric field amplitudes.

We also compared the calculated temperature with the low intensity temperature dependence on the detuning for continuous-wave laser cooling:

$$T = \frac{\hbar\Gamma}{2k_B} \frac{1 + (2\delta/\Gamma)^2}{2|\delta|/\Gamma} \quad (3.18)$$

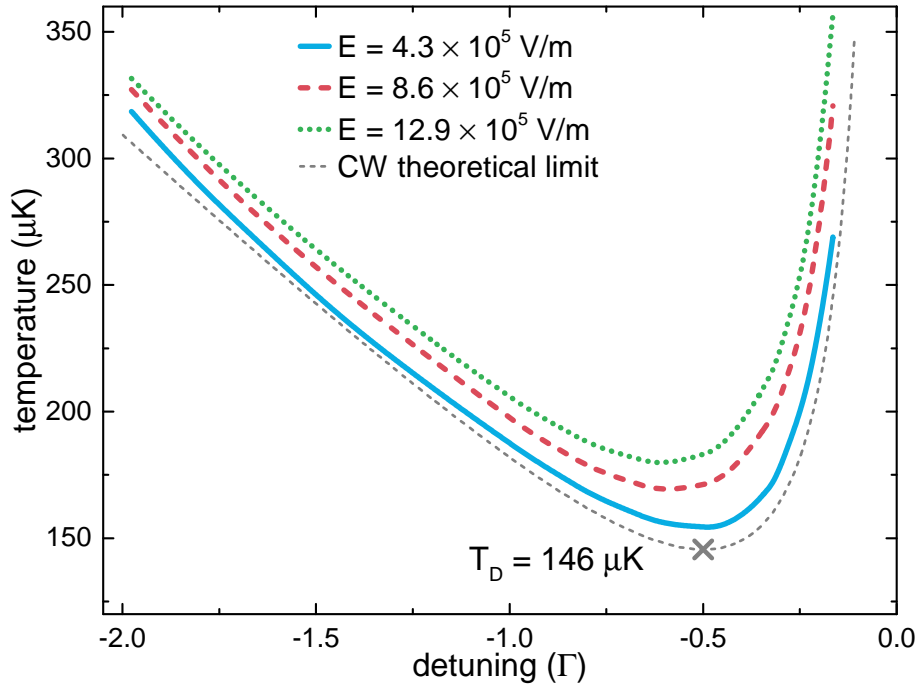


Figure 3.10: Temperature of atoms as a function of detuning of the  $n$ -th comb mode from the cooling transition for different pulse electric field amplitudes. Gray dashed line presents the Doppler temperature for cw interaction with two-level atoms. Parameters used in the calculation:  $f_{rep} = 187.657$  MHz,  $\Phi_R = 0$ ,  $\tau_P = 80$  fs and  $\tau = T_R/2$ .

This equation is also valid for the theory of two counter-propagating pulse trains for two-level atoms [15], for high pulse repetition rate ( $T_R \ll \tau_P$ ) and low intensity pulses.

As it is expected, for the lowest presented pulse electric field amplitude in Fig. 3.10, minimum achieved temperature is at  $-\Gamma/2$  detuning. The temperature at  $-\Gamma/2$  is  $154.3 \mu\text{K}$ , which is very close to the Doppler temperature of  $146 \mu\text{K}$ . For detunings closer to the atomic resonance temperature is increasing significantly, and for detunings higher than  $-\Gamma/2$  temperature is also increasing, as is predicted in theory. Since the calculation is made for six-level atoms, there is a slight deviation from the theoretical curve, due to the influence of other comb modes on other respective transitions.

With the increase in the electric field amplitude, the temperature of atoms is also increased, according to the theory for frequency comb cooling of two-level atoms and cw cooling of two-level atoms. To achieve temperatures closer to the Doppler limit, even smaller electric field amplitude of FC beams is necessary, with the consequence of increased time for a system to reach a stationary state. More importantly, in experiments the consequence of the lower electric field amplitudes, i.e. intensity is smaller number of atoms that are laser cooled.

### 3.5 Conclusion

To summarize, we developed a model of interaction of a six-level atom with two counter-propagating pulse trains. The pulse trains are interacting with atoms in 1D, where the spectrum of a single pulse train is an optical frequency comb. The interaction of atoms with frequency comb beams is very complex since multiple comb modes can be resonant with multiple transitions in a multi-level atoms. To optimize the comb parameters with regard to the atomic transitions, it is necessary to study the relative positions of the comb modes with regard to the atomic transitions. From this analysis, one can conclude on which comb parameters could lead to an effective cooling of atoms with a frequency comb.

In the model, we developed a set of differential equations for the time evolution of the density matrix elements for selected atoms. The stationary state solutions of the equations give the information about the ground and excited states populations, as well as the information about the coherence terms.

We presented two different methods of calculating the radiation pressure force from the stationary state solution for the density matrix elements. The advantage of the iterative method is the low computational time necessary to calculate the radiation pressure force exerted on the atoms. Similarly, the diffusion coefficient is calculated iteratively. The results of the radiation pressure force and diffusion coefficient provide information on the efficiency of the cooling process with selected comb parameters.

Finally, the temperature of atoms is calculated using the Fokker-Planck equation, where we insert the calculated radiation force and diffusion coefficient as function of the atomic velocity. From the atomic velocity distribution time evolution, we can get the temperature of atoms after the interaction with two counter-propagating pulse trains, as well as the time required for velocity distribution to reach a stationary state.

The results presented in this work are for the interaction of  $^{87}\text{Rb}$  atoms with two counter-propagating pulse trains. With a slight modification of the atomic parameters, it is possible to perform calculations for any atom that has an energy level structure similar to the  $^{87}\text{Rb}$  atom.

We discussed three different sets of comb parameters, where we fixed the detuning of the  $n$ -th comb mode to the cooling transition to be  $\delta = -\Gamma$ . First repetition frequency we discussed is  $f_{rep} = 187.82$  MHz, where  $n$ -th comb mode is  $-\Gamma$  detuned from the cooling transition and  $(n + 35)$ -th comb mode is on resonance with a repumping transition. This is an example of the optimal case where all population is optically pumped into the  $|F = 2\rangle$  ground level which enables efficient excitation of the cooling transition. Here only two comb modes participate in the comb-atom interaction around  $v = 0$ . This set of comb parameters mimics the stan-

standard continuous-wave laser cooling experiment, where one comb mode is the cooling laser and another comb mode is the repumping laser. The radiation pressure force slope in this case is steeper in comparison to other sets of comb parameters we discussed in this work, so it reduces the velocity of atoms efficiently. Calculated stationary state temperature is  $185 \mu\text{K}$ , which is close to the Doppler cooling temperature. By optimizing the detuning of the  $n$ -th comb mode and by lowering the pulse electric field amplitude, it is possible to reach temperatures even closer to the Doppler limit, but lowering the comb intensity comes at the expense of cooling less atoms.

The second discussed repetition frequency is 250 MHz, where the  $n$ -th comb mode is  $-\Gamma$  detuned from the cooling transition, and  $(n - 1)$ -st comb mode is  $-1.8\Gamma$  detuned from the  $|F = 2\rangle \rightarrow |F' = 2\rangle$ , while other modes are far detuned from other transitions. Here the majority of the population from the  $|F = 2\rangle$  level state is optically pumped into the  $|F = 1\rangle$  ground level. The loss of the atoms from the cooling cycle is therefore significant resulting in the inefficient laser cooling process. The last discussed repetition frequency is 80.5 MHz, which is the repetition frequency of the frequency comb laser available in our laboratory. Here only the cooling comb mode is close to resonance, optical pumping into the  $|F = 1\rangle$  ground state is partial, and, as a result, some of the atoms are lost from the cooling cycle. Temperatures calculated for these two comb parameters are higher in comparison to the temperature for 187.82 MHz. It also takes a lot more time to reach the stationary state, i.e. the final temperature, since the radiation pressure force, as well as the slope of the force, is smaller.

Three sets of comb parameters discussed here are only examples which showcase possible conditions of comb-atom interaction and its effect on the cooling process. Many sets of comb parameters can lead to effective cooling with a frequency comb, but much more will not. To achieve efficient laser cooling with a frequency comb several conditions have to be met. The first one is to red-detune (on the order of  $\Gamma$ ) comb mode from the cooling transition. The second condition is to tune the repetition frequency so that simultaneously there is a comb mode that is near-resonant with a repumping transition. We provided a relation (3.14), which gives a range of repetition frequencies that satisfy both conditions, and can be used as a rule of thumb in designing optimal frequency comb parameters for cooling of a specific atom. Another concern is when three or more comb modes are near resonance with respective transitions.

Laser cooling with a frequency comb is a very promising solution for the limitations of standard continuous-wave laser cooling. Frequency comb is a very flexible source where different comb modes can excite different transitions, even reaching the far UV spectral range. One of the issues in laser cooling experiments is the complexity of the experimental setup. Typically, several lasers have to be frequency stabilized using feedback loops simultaneously. Using fre-

quency combs in laser cooling experiments can reduce the number of stabilized lasers needed to only a single laser source. This can have great potential in experiments where many lasers are required, either due to the complexity of energy level structure or due to several different atomic species used simultaneously. Another potential application of a frequency comb as a laser cooling source is in experiments where simplification of a complete system is crucial for the development of mobile quantum sensors based on the cold atoms, such as for the applications of laser cooling experiments in space.

## Chapter 4

# Simultaneous dual-species laser cooling using an optical frequency comb

In the previous chapter, I presented theoretical calculations of the 1D laser cooling with a frequency comb for different sets of comb parameters. In the calculations, it is easy to find frequency comb parameters that lead to effective laser cooling. On the contrary, in the usual experimental laboratory conditions changing the comb parameters is quite restricted. This primarily refers to the repetition frequency, where it can typically be tuned from several kHz to several MHz, depending on the mechanical design of the laser source. The offset frequency can typically be tuned from  $-f_{rep}/2$  to  $f_{rep}/2$ , so detuning of a comb mode with respect to the cooling transition can be easily adjusted.

Another approach to laser cooling with a frequency comb is to design a frequency comb source with specific comb parameters, adjusted so the laser cooling process is optimized. This approach is technically demanding and can be rather expensive.

In the experiment, we used a frequency comb with a repetition frequency of 80.495 MHz and additional continuous-wave lasers as repumping lasers. We used two different comb modes as cooling lasers for two Rubidium isotopes,  $^{85}\text{Rb}$  and  $^{87}\text{Rb}$ .

In this chapter, I will describe the experimental setup used to generate the dual-species MOT and the demonstration of the dual-species laser cooling with a frequency comb.

## 4.1 FC laser cooling experiments

In recent literature there are several experimental demonstrations of laser cooling using an optical frequency comb. These demonstrations can be divided into three different approaches to laser cooling with a frequency comb.

The first approach is to use a pulse train with a repetition period longer than the excited state lifetime. In such experiments atoms (or ions) do not build an excited state population coherently across pulses and the cooling limit is related to the inverse of the pulse duration. Experimental demonstration of such kind of laser cooling using a pulse train from a mode-locked laser is on the  $\text{Cd}^+$  ions [50]. In the experiment, they used a picosecond frequency comb with a repetition frequency of around 80 MHz. The excited state lifetime is shorter than the pulse train repetition period, so the coherence between consecutive pulses is lost. In other words, the absorption spectrum is proportional to a single broad line with a bandwidth of  $1/\tau$ , where  $\tau$  is pulse duration. The equilibrium temperature for laser cooling with broadband pulsed excitation is scaling approximately with laser bandwidth but is much higher in comparison to the typical temperatures in conventional laser cooling experiments. The central wavelength of the Ti:Sapphire laser was frequency quadrupled to achieve light centered around 226.5 nm. This is the wavelength of the  $^2S_{1/2} - ^2P_{1/2}$  transition for  $\text{Cd}^+$  ion, where using around 1 mW of power they achieved temperatures around 1 K.

In literature, there is another demonstration of this approach of laser cooling with a frequency comb. In this experiment [13]  $^{171}\text{Yb}^+$  and  $^{174}\text{Yb}^+$  are laser cooled using a broadband laser, red detuned from the resonance. Due to the experimental limitations, they measured temperature to be upper bounded at 240 mK, while they predict a temperature of 830  $\mu\text{K}$ . They used a Ti:Sapphire picosecond mode-locked laser with a repetition frequency of 81.553 MHz. Using the second harmonic generation process they generated around 9 mW of average power around 369.5 nm to drive  $^2S_{1/2} - ^2P_{1/2}$  transition in  $\text{Yb}^+$  ions. To achieve cooling of  $\text{Yb}^+$  ions they used an additional continuous-wave laser at 935 nm as a repumping laser.

The second approach to laser cooling with a frequency comb is to use it to excite a two-photon transition. In comparison to the single-photon excitation with a frequency comb, where only one comb mode participates in the excitation, in a two-photon excitation, many pairs of comb modes can participate in the excitation. This is possible since all frequency comb modes are mutually coherent. In comparison to the continuous-wave two-photon excitation, the two-photon scattering rate of a frequency comb excitation is approximately the same, if the average comb intensity is the same as the intensity of a continuous-wave laser [11]. This approach has a big advantage for atoms with transitions in the ultraviolet spectrum, where the available power

of pulsed laser sources can be a few orders of magnitude higher than of the continuous-wave laser sources.

In recent literature, there is an experimental demonstration of two-photon laser cooling with a frequency comb of the  $^{85}\text{Rb}$  atoms [46]. The excitation of a two-photon transition  $5^2S_{1/2} \rightarrow 5^2D_{5/2}$  is achieved using a Ti:sapphire mode-locked picosecond laser, with a central wavelength around 778 nm and repetition frequency of 81.14 MHz. Since each pair of comb modes adds coherently, excitation can be explained using an effective *two-photon comb* [46]:

$$f_n = n f_r + 2 f_0, \quad (4.1)$$

where  $f_r$  is the repetition frequency and  $f_0$  is the carrier-envelope offset frequency. In the experiment, they generated a cold cloud of  $^{85}\text{Rb}$  using a standard continuous-wave laser cooling technique at around 110  $\mu\text{K}$ . In the next stage, they excite a two-photon transition using a frequency comb in 1D, where the minimum temperature measured is around 57  $\mu\text{K}$ . To demonstrate cooling an additional continuous-wave laser was used as a repumping laser. The achieved temperature is below the Doppler limit temperature for a single-photon transition but is above the expected two-photon Doppler limit temperature of 31  $\mu\text{K}$ .

The last method of laser cooling with a frequency comb is using a single comb mode to excite the cooling transition. For this method repetition period of pulses must be shorter than the excited state lifetime, so the excited state population is coherently accumulated across many pulses. In this cooling scheme single comb modes can be interpreted as single cw lasers. Different comb modes can be used as cooling or repumping lasers, or to simultaneously excite cooling transitions of different atomic or ionic species.

The first demonstration of laser cooling with a frequency comb using a single comb mode is on  $\text{Mg}^+$  ions [12]. In the experiment mode-locked Ti:Sapphire laser with a central wavelength of 840 nm and repetition frequency of 373 MHz is used. To excite the  $D_2$  line of  $\text{Mg}^+$  at 280 nm they used the third harmonic of the laser, using stages of second harmonic generation with subsequent sum-frequency generation stage. The temperature achieved for the  $^{26}\text{Mg}^+$  is around 1.16 mK, which is close to the Doppler temperature. Unlike the  $^{26}\text{Mg}^+$  isotope, the  $^{25}\text{Mg}^+$  isotope has a hyperfine structure, so cooling was observed only when a comb mode was red detuned from the  $D_2$  cooling transition  $|F = 3\rangle \rightarrow |F' = 4\rangle$  an additional comb mode was near-resonant with the  $D_2$   $|F = 2\rangle \rightarrow |F' = 3\rangle$  transition, repumping transition.

Another demonstration of single-mode frequency comb cooling was achieved for dipole-allowed transition for  $^{87}\text{Rb}$  atoms [45] in our group. The frequency comb used in the experiment was  $\text{Er}^{3+}$  doped fiber laser at 1560 nm, with a repetition frequency of 80.5 MHz. To excite the  $^{87}\text{Rb}$  cooling transition, central laser frequency was frequency-doubled to 780 nm. The mini-

mum achieved temperature was  $155 \mu\text{K}$ , which is close to the Doppler limit temperature for Rb atoms. Since power per comb mode was very low, a cloud was pre-cooled to the temperature of around  $250 \mu\text{K}$  using standard continuous-wave cooling techniques. As for this pulse repetition frequency there are no available comb modes near-resonant with the repumping transition, an additional continuous-wave repumping laser was introduced to keep the atoms in the cooling cycle.

In this chapter, I will present a recent demonstration of dual-species laser cooling using a frequency comb, where two different comb modes have the role of cooling lasers for two atomic species simultaneously. To keep atoms in the cooling cycle two additional continuous-wave lasers were introduced as repumping lasers.

## 4.2 Rubidium atom

In the experiment, we use the rubidium atoms. Rubidium is an atom with the atomic number 37. Its electron configuration is  $[\text{Kr}] 5s^1$  and is one of the alkali metals. One electron in the outer shell makes it a Hydrogen-like atom, with a relatively simple hyperfine structure. The main atomic transition of Rb is at  $780 \text{ nm}$ , and this is the main reason that Rb is one of the prevailing species in the laser cooling and Bose-Einstein condensation experiments.

In nature, rubidium has two common isotopes, one stable isotope  $^{85}\text{Rb}$ , with an abundance of 72 % and other slightly radioactive  $^{87}\text{Rb}$ , with an abundance of 28 % and half-life of  $48.8 \times 10^9$  years. Other isotopes are synthesized in the laboratory, but they have a short half-life and their usage is limited. Rubidium's color is grey-white and its melting temperature is  $39.3^\circ\text{C}$ . This makes it easy to obtain high concentrations of the vapor with moderate heating.

In the experiment, we use rubidium in two different forms. Rubidium atoms in the glass cells are used for spectroscopy, which is necessary for laser tuning and stabilization. In the vacuum chamber, we use rubidium dispensers, which are heated using the current of  $\sim 4 \text{ A}$ , so they evaporate rubidium atoms in the vacuum chamber.

To demonstrate the multi-species laser cooling with a frequency comb, we use both  $^{85}\text{Rb}$  and  $^{87}\text{Rb}$  isotopes. In theory, we could use any other atomic species that can be laser cooled, but the limiting factors are the availability of the atomic species in the vacuum chamber, availability of cw laser sources in the lab and the spectral width and the repetition frequency of the frequency comb light.

There are two main transitions in the rubidium atoms that are a consequence of spin-orbit coupling.  $5S_{1/2} \rightarrow 5P_{1/2}$  transition and  $5S_{1/2} \rightarrow 5P_{3/2}$ , more commonly known as  $D_1$  and  $D_2$  transitions. Wavelengths of these two transitions for both Rb species are around  $795 \text{ nm}$  for  $D_1$

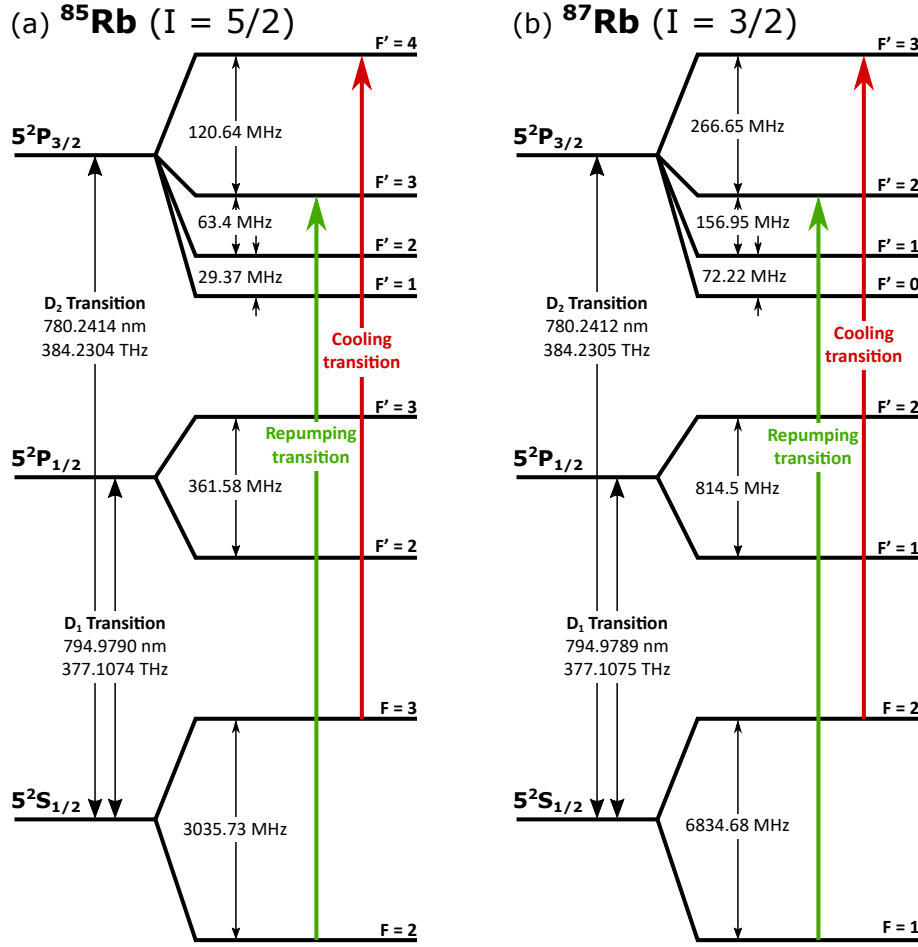


Figure 4.1: (a)  $^{85}\text{Rb}$  and (b)  $^{87}\text{Rb}$  hyperfine energy level structure. Red arrows mark the cooling transitions  $|5S_{1/2}; F=3\rangle \rightarrow |5P_{3/2}; F'=4\rangle$  and  $|5S_{1/2}; F=2\rangle \rightarrow |5P_{3/2}; F'=3\rangle$ , and green arrows mark the repumping transitions  $|5S_{1/2}; F=2\rangle \rightarrow |5P_{3/2}; F'=3\rangle$  and  $|5S_{1/2}; F=1\rangle \rightarrow |5P_{3/2}; F'=2\rangle$ , for  $^{85}\text{Rb}$  and  $^{87}\text{Rb}$  isotopes respectively. Adapted from [38] and [39].

transition and around 780 nm for D<sub>2</sub> transition. The isotopes have a nuclear spin of  $I = 5/2$  and  $I = 3/2$  for  $^{85}\text{Rb}$  and  $^{87}\text{Rb}$ , respectively. Total angular momentum  $\mathbf{F} = \mathbf{I} + \mathbf{J}$ , and  $\mathbf{I} \cdot \mathbf{J}$  coupling, leads to the hyperfine splittings where isotopes have different level structure splitting. Energy level structure for  $^{85}\text{Rb}$  and  $^{87}\text{Rb}$  is presented in Fig. 4.1.

Atoms in the vacuum chambers are at room temperature, and to laser cool them to the range of  $\sim 100 \mu\text{K}$  many cycles of absorption and spontaneous emission are needed. To achieve this, the frequency of the laser that is cooling the atoms has to be red detuned from the frequency of the closed transition of the atom. During this excitation, there is a small chance to excite another excited state and relax to the dark state, in which atoms are lost from the cooling cycle.

To avoid this, we have to introduce an additional laser, to restore the atoms from the dark state to the cooling cycle. We call this laser a repumping laser.

The cooling transitions for both species are marked with red arrows, and the repumping transitions are marked with green arrows. For  $^{85}\text{Rb}$  isotope the cooling transition is  $|5S_{1/2}; F = 3\rangle \rightarrow |5P_{3/2}; F' = 4\rangle$  and for  $^{87}\text{Rb}$  isotope is  $|5S_{1/2}; F = 2\rangle \rightarrow |5P_{3/2}; F' = 3\rangle$ . The repumping transition for  $^{85}\text{Rb}$  isotope is  $|5S_{1/2}; F = 2\rangle \rightarrow |5P_{3/2}; F' = 3\rangle$  and for the  $^{87}\text{Rb}$  is  $|5S_{1/2}; F = 1\rangle \rightarrow |5P_{3/2}; F' = 2\rangle$ .

The frequencies of cooling transitions for these two isotopes differ by 1126 MHz. The frequency comb source we have in the laboratory has a repetition frequency of around 80.5 MHz which is only narrowly tunable by the means of the stepper motor built in the laser cavity. This is very fortunate since the difference in the cooling transitions for our Rb isotopes closely matches the multiple of the repetition frequency, so the repetition frequency we have tuned our FC is 80.495 MHz.

Both isotopes have the decay rate of the excited state  $|5P_{3/2}\rangle$   $\Gamma = (2\pi) \cdot 6.0666(18)$  MHz, and of the excited state  $|5P_{1/2}\rangle$   $\Gamma = (2\pi) \cdot 5.7500(56)$  MHz [38, 39]. Doppler temperature for the  $D_2$  transition is  $154.57 \mu\text{K}$ , and the recoil temperature is  $370.47 \text{ nK}$  for  $^{85}\text{Rb}$  and  $361.96 \text{ nK}$  for  $^{87}\text{Rb}$ .

## 4.3 Experimental setup

### 4.3.1 Laser system

The existing laser system in the lab has been used to generate the single-species magneto-optical trap. To demonstrate dual-species cooling with a frequency comb, we have upgraded the existing setup, so we can load and cool atoms of  $^{85}\text{Rb}$  and  $^{87}\text{Rb}$  simultaneously. We have used four independent continuous-wave lasers, one cooling and one repumping laser for each rubidium isotope.

The laser for the cooling of  $^{87}\text{Rb}$  isotope is an external cavity diode laser, Moglabs CEL002. This laser has an anti-reflection laser diode and uses the cat-eye configuration to get the narrow linewidth. The linewidth of this laser is around 80 kHz, which is measured with heterodyne beat spectroscopy with an FC. This laser is stabilized to the polarization spectroscopy signal [51].

Usually, we use a home-built tapered amplifier diode (TA) to obtain higher optical powers needed for the experiment, but at the time of conducting this experiment, the electronics box for the TA broke so we had to amplify the laser power by other means. Fortunately, we had an additional DL100 free-running laser from Toptica, as well as high power laser diodes so we opted for the injection locking of the slave laser to obtain higher optical power [52, 53].

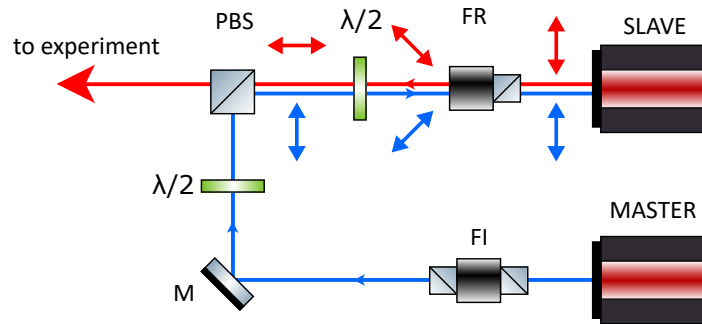


Figure 4.2: Setup for injection locking of lasers. For clarity, we have spatially separated two beams and marked each with a different color. The master laser beam is marked with blue color, and the slave laser beam is marked with red color. The blue and red arrows display the polarization of beams at the place where they are positioned. The wavelengths of the master and slave laser are similar. Abbreviations used: PBS - polarizing beam splitter,  $\lambda/2$  - half waveplate, FR - Faraday rotator, M - mirror, FI - Faraday isolator.

Injection locking is the method for obtaining the high power laser light while maintaining the narrow linewidth. The master laser has usually narrow linewidth and low power. A small portion of the master laser light is injected into the laser diode of the slave laser, and it drives the emission of the slave laser to be phase coherent to the master laser. To prevent unwanted

back-reflection to the master laser, we used a Faraday isolator. For the injection locking a Faraday isolator with the rejection port is usually used. In the lab, we did not have any Faraday isolator of this kind so we opted to partially disassemble one Faraday isolator to create a home-built rejection port. The setup for this assembly is displayed in Fig. 4.2, where we marked the polarization of laser beams coming from the master and slave laser. The polarization of the master beam after the polarizing beam splitting cube is vertical. Half-waveplate has been setup to rotate the polarization by  $45^\circ$ . Faraday rotator is a device that rotates the laser beam by  $45^\circ$  in one direction (for example counter-clockwise direction), regardless of the direction of the beam input. Finally, after the rotator, the polarization of the master beam is vertical and this matches the slave laser diode polarization. Polarization of the slave beam is vertical, and after the Faraday rotator is  $45^\circ$  counter-clockwise polarized. Half-waveplate makes this polarization horizontal, and this polarization of the slave laser is transmitted through the PBS to the experiment. This improvised Faraday isolator enables us to use it to safely inject the master laser beam into the slave laser, but at the same time, it protects the slave laser from other unwanted back-reflections. The power of the master beam injected in the slave diode is around 5 mW. A high power laser beam from the slave laser is used as a cooling beam, which passes through a double-pass acousto-optic modulator (AOM) setup to fine-tune the beam detuning from the cooling transition, and to be able to precisely switch this beam on and off.

The cooling laser for the  $^{85}\text{Rb}$  is the Toptica DL100 laser, with a high power laser diode. This is an external cavity diode laser setup in the Littrow configuration. Direct modulation of the laser current, as typically used to stabilize the laser using saturation spectroscopy, broadened the laser linewidth to around 2.7 MHz, a laser linewidth too broad to use for a cooling laser. Instead, we modulated the magnetic field in the reference Rb vapor cell using the Toptica LIR 110 module as the modulation source and a commercial audio amplifier to drive the Maxwell coils around the cell. Using this technique of laser stabilization, laser linewidth was reduced to 0.6 MHz, which was narrow enough for the use in laser cooling. More about this laser stabilization technique is available in literature [7]. For this laser double-pass AOM setup was used for fine-tuning the laser detuning from the cooling transition in  $^{85}\text{Rb}$  atoms, and precise switching on and off the laser beam.

Repumping lasers for the  $^{85}\text{Rb}$  and  $^{87}\text{Rb}$  species were Toptica DL100 lasers. These two lasers are ECDL diode lasers in Littrow configuration, which were stabilized using the saturation spectroscopy, with current modulation. Repumping lasers do not require as much stability as cooling lasers, so the linewidths of a few MHz are usually enough for repumping lasers. Fine-tuning and switching on and off were achieved with a single-pass AOM setup.

### 4.3.2 Frequency comb

The frequency comb spectrum is generated from the femtosecond mode-locked  $\text{Er}^{3+}$  doped fiber laser Toptica Photonics Femtofiber Scientific FFS. Central wavelength of this laser is around 1560 nm with spectrum FWHM of 50 nm, and with pulse length of around 150 – 200 fs. The main parts of this laser are an oscillator and an amplifier, where the cavity length of the oscillator defines the repetition frequency of laser pulses. Mode locking is achieved by the nonlinear polarization rotation method [54, 55]. This is a fiber laser, with a small free space part, where waveplates are placed. At one fiber coupler end, there is a motorized linear stage, which can change the length of the laser cavity and thus the pulse repetition frequency. Repetition frequency for this laser can change around 100 kHz, so we tuned it to be 80.495 MHz, almost at the lower limit for the repetition frequency. The average power emitted from the laser is around 220 mW. The frequency comb oscillator and amplifier stage are presented in Fig. 4.3.

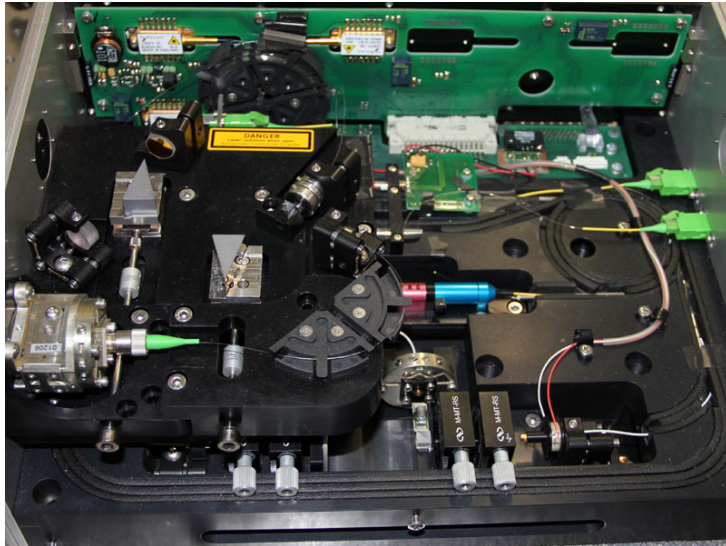


Figure 4.3: A photograph of the frequency comb oscillator and amplifier. In the bottom part of the figure is the free space part of the laser cavity responsible for mode-locking and adjusting the repetition frequency.

To excite cooling transitions for both rubidium isotopes, we used PPLN crystal to generate a second-harmonic of the original spectrum to obtain the frequency comb centered around 780 nm and with FWHM of 5 nm. Spectrum of the frequency comb is presented in Fig. 4.4. Pulses of the second-harmonic were around 200 fs long, and the average power is around 70 mW. We estimate that around 100000 comb modes are under the spectrum of the frequency comb at 780 nm.

To demonstrate laser cooling with a frequency comb, it is necessary to stabilize the spectrum

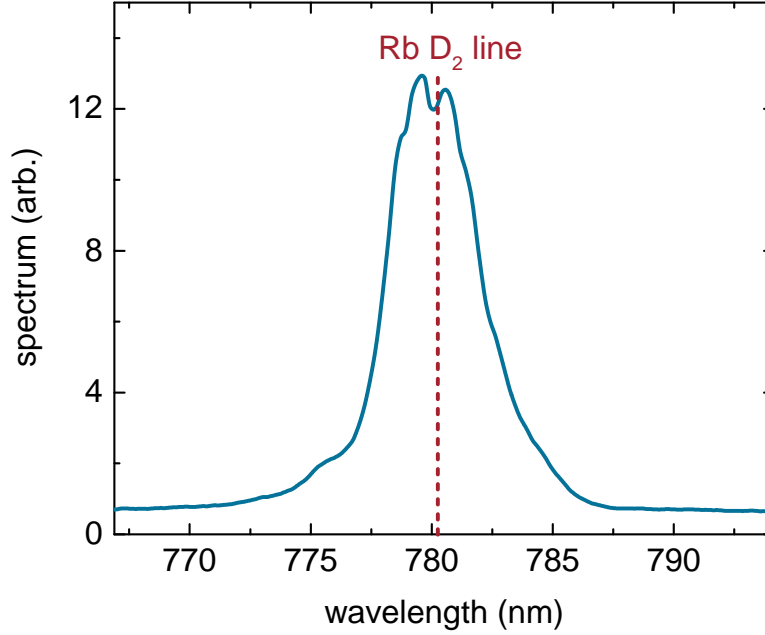


Figure 4.4: The spectrum of a frequency comb light centered around 780 nm used to demonstrate simultaneous cooling of two Rb isotopes. The wavelength of the Rb  $D^2$  transition, used for laser cooling, is marked with red dashed line.

of a frequency comb laser. The spectrum of a frequency comb is described with:

$$f_n = n f_{rep} + f_0, \quad (4.2)$$

where  $f_n$  is the frequency of the  $n$ -th comb mode,  $f_{rep}$  is the repetition frequency and  $f_0$  is the offset frequency. Repetition frequency is measured with a fast photodiode placed inside the laser oscillator. This frequency is compared with a direct digital synthesiser (DDS) output referenced on the rubidium standard clock on the frequency-phase detector. Output from the frequency-phase detector is an error signal used with a proportional–integral–derivative (PID) controller to stabilize the repetition frequency with a piezoelectric device, which is placed inside the laser oscillator.

To stabilize the whole comb spectrum it is usual to build an  $f$ - $2f$  interferometer, so the offset frequency can be measured and stabilized [56]. This stabilization method is impractical in our case as almost all power would be used for comb stabilization, leaving insufficient power for comb cooling. We used an alternative comb stabilization method instead, by locking a comb

mode to a continuous-wave reference laser, frequency-shifted Moglabs CEL002 laser. To compare frequencies of the  $n$ -th comb mode with the continuous-wave laser we use heterodyne beat spectroscopy, where the output is the frequency difference between two optical frequencies  $f_{beat} = |f_n - f_{cw}|$ . The beat signal is amplified and filtered to remove beat frequencies with other than nearest comb modes. To increase the capture range of the lock, the beat frequency is divided by a factor of 64. An error signal is obtained by comparing this divided beat frequency with an output from the DDS. Servo PI controller Newport LB1005 is used to generate a feedback signal to the pump current of the laser oscillator to stabilize the beat frequency and thus the whole frequency comb spectrum. The scheme of the setup for frequency comb stabilization is presented in Fig. 4.5. Details about the frequency comb stabilization can be found in [7].

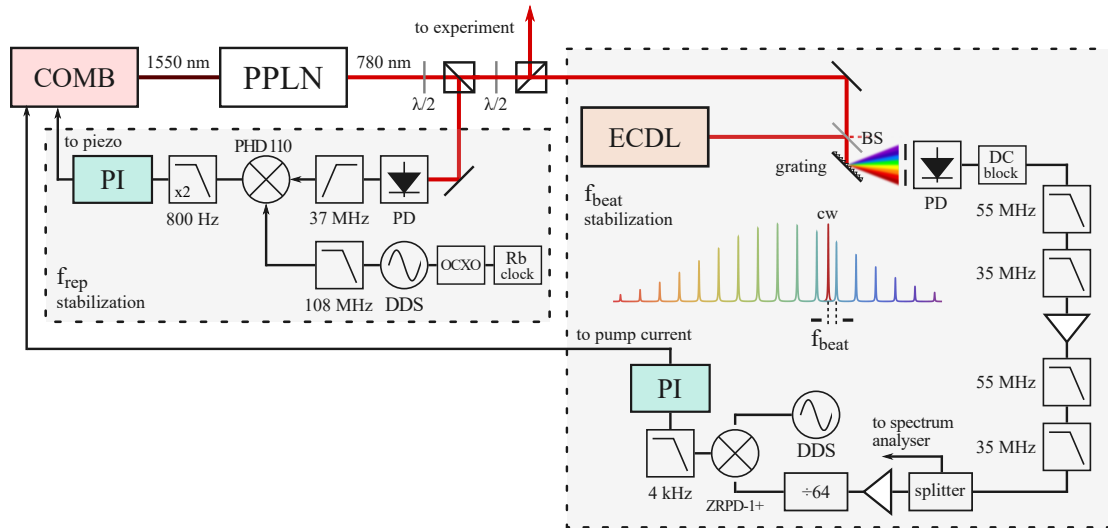


Figure 4.5: Frequency comb stabilization scheme. Two separate feedback loops are necessary to stabilize the whole comb spectrum. The left part of the scheme presents a feedback loop for stabilization of the repetition frequency. The right part of the scheme presents the setup to measure beat signal with a stable cw reference laser and the scheme of the feedback loop to stabilize a comb mode to the cw reference. Abbreviations used: PPLN - periodically poled lithium niobate crystal, PD - photodiode,  $\lambda/2$  - half waveplate, DDS - direct digital synthesizer, OCXO - oven-controlled crystal oscillator, ECDL - external cavity diode laser, BS - beam splitter. Taken from [7].

### 4.3.3 Magneto-optical trap

Cold clouds of rubidium atoms are generated inside the 316LN stainless steel vacuum chamber. Pressure inside the chamber is maintained at around  $10^{-8}$  mbar using the Varian VacIon Plus StarCell 55 ion pump. Vacuum chamber has two 8 in windows, eight 2.87 in and four 1.33 in

window ports, where windows are coated with broadband anti-reflection coating. Despite the coating, transmission of the laser power through windows is around 90 %, most probably due to the thin rubidium deposits on the windows. Nipples are installed on two 1.33 in ports, each with four rubidium dispensers installed inside of them. About 4 A of current is applied through a dispenser to generate the rubidium background vapor at natural abundance. Picture of a vacuum chamber is presented in Fig. 4.6.

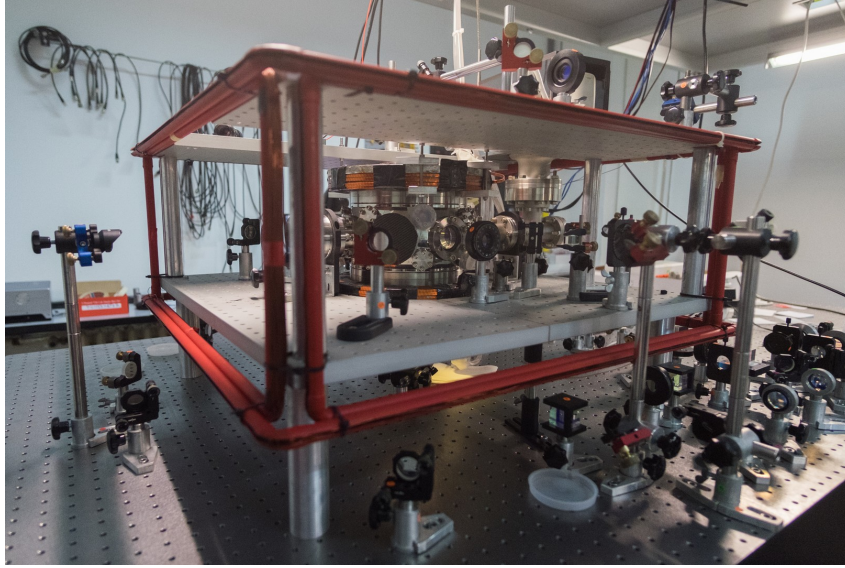


Figure 4.6: Photograph of the vacuum chamber where cold Rb clouds are generated. Around the vacuum chamber, there is a pair of coils that produce a gradient of the magnetic field. Optics around the vacuum chamber is guiding the laser beams into the vacuum chamber, where they overlap in the center of the chamber.

To create a magneto-optical trap it is necessary to generate a gradient of the magnetic field at the center of the trap. Due to the limitation of the current power supply and the geometry of the vacuum chamber, we used two coils in a near anti-Helmholtz configuration. Each coil has 100 windings placed in four layers. Due to the large power dissipation, coils are water-cooled with pipes soldered to the coil housing. In usual experimental conditions the magnetic field gradient used is 11.3 G/cm, where around 17 A of current from the power supply is drawn. We implemented a fast switch for the magnetic field gradient, where the current through coils is decayed after around 2.8 ms [7]. Fast switching off of the magnetic field gradient induces eddy currents in big aluminum plates and copper gaskets inside the vacuum chamber and this induced magnetic field is decaying slowly, with a decay constant of around 10 ms. We have cut the aluminum plate in a way that it does not form a closed path, which slightly lowered the decay constant of the magnetic field, but the effect is still significant for the times used in

the experiment. We therefore opted not to switch off the gradient coils during the experiment. More about the construction of the anti-Helmholtz coils and fast switches can be found in [7].

To compensate for the stray magnetic field of the Earth and other fields from the environment, we built three pairs of coils. These coils are producing a near homogeneous magnetic field around the center of the vacuum chamber, which ensures that the magnetic field zero is at the center of the vacuum chamber, where all six beams overlap and a cold cloud is generated. Details about the compensation coils can be found in [57].

#### 4.3.4 Optics setup for laser cooling and trapping

The requirement for the laser cooling of atoms is that the laser beam responsible for cooling has to be red detuned from the cooling transition. Detuning of the cooling lasers in the experiment is controlled using two double-pass AOM setups, where the first one is on the spectroscopy line, and the other is on the experiment line. Since both cooling lasers are locked to their respective cooling transitions, total detuning can be calculated using an expression  $\delta = 2f_{ex} - 2f_{sp}$ , where  $f_{ex}$  is the driving frequency of the AOM device placed on the experiment line, and  $f_{sp}$  is the driving frequency of the AOM device placed on the spectroscopy line. Red detuning is achieved when  $f_{sp} > f_{ex}$ . Optics setup is presented in Fig. 4.7, where the blue dashed box marks the setup for the cooling beam for  $^{87}\text{Rb}$ , and the green dashed box marks the setup for the cooling beam of  $^{85}\text{Rb}$  isotope.

The cooling lasers are coupled to the same polarization-maintaining fiber, so the overlap of the cooling beams in the trap region is optimal. This is done so that the clouds of two Rb isotopes overlap as good as possible. To couple the full power of both cooling beams into the same fiber, their polarizations are perpendicular, where the  $^{85}\text{Rb}$  cooling beam is coupled to the fast axis of the PM fiber, and the  $^{87}\text{Rb}$  cooling beam is coupled to the slow axis of the PM fiber. To ensure polarization matching of these two beams to the fiber axis, a half-waveplate is inserted between the polarizing cube and fiber coupler.

Repumping beam for the  $^{85}\text{Rb}$  atoms is locked to the crossover peak arising from the  $|F = 2\rangle \rightarrow |F' = 1\rangle$  and  $|F = 2\rangle \rightarrow |F' = 2\rangle$  transitions, and is shifted using an AOM to be in resonance with the  $|F = 2\rangle \rightarrow |F' = 3\rangle$  repumping transition. Similarly, repumping beam for the  $^{87}\text{Rb}$  atoms is locked to the crossover peak arising from the  $|F = 1\rangle \rightarrow |F' = 1\rangle$  and  $|F = 1\rangle \rightarrow |F' = 2\rangle$ , and then frequency shifted with an AOM to the resonance with the  $|F = 1\rangle \rightarrow |F' = 2\rangle$  repumping transition. Two repumping beams are coupled into another PM fiber so repumping beams are also co-propagating after the fiber output.

As mentioned in Section 2.2.2, if the magnetic field gradient is twice as big in the  $z$  direction in comparison to  $x$  and  $y$  direction, then the power of the beams in  $x$  and  $y$  direction has

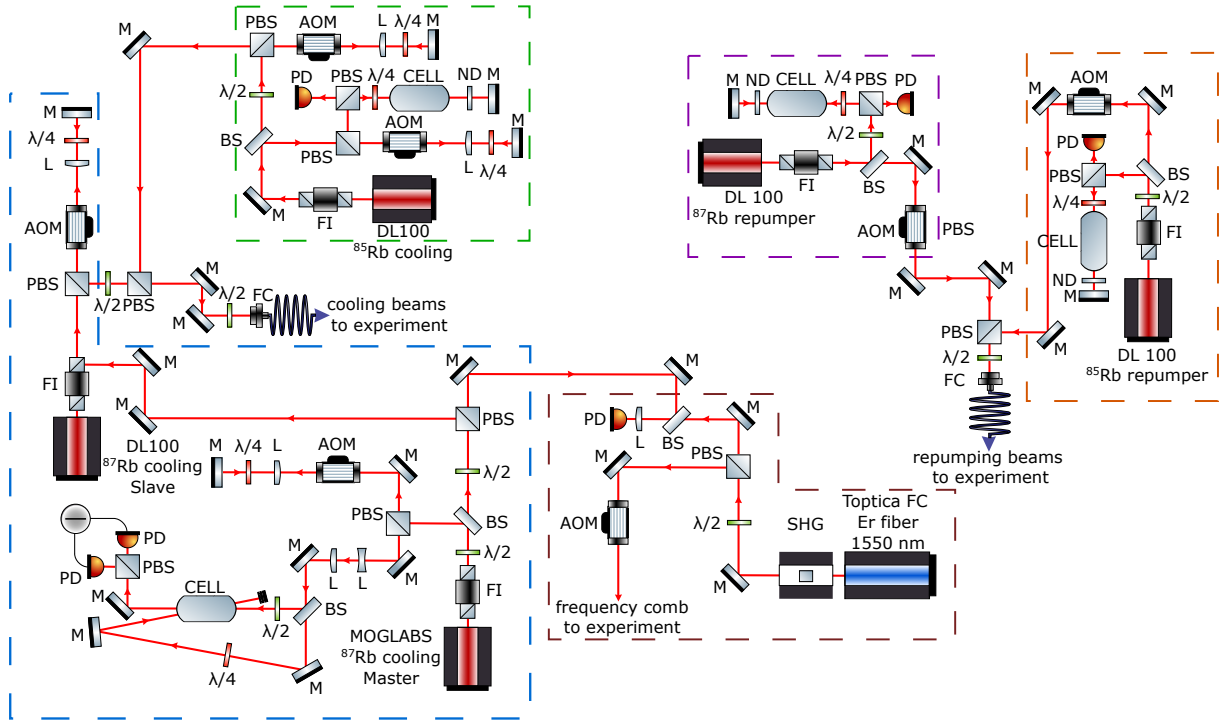


Figure 4.7: Schematic experimental setup for the dual-species MOT and demonstration of the simultaneous dual species frequency comb laser cooling. Laser systems and related optics for cooling and repumping lasers are marked with dashed boxes. Abbreviations used in the image: M - mirror, L - lens, PD - photodiode, ND - neutral density filter, BS - beamsplitter, PBS - polarizing beam splitter, FI - Faraday isolator, CELL - Rubidium Cell, SHG - second harmonic generation unit, AOM - acousto-optics modulator,  $\lambda/2$  - half-waveplate,  $\lambda/4$  - quarter-waveplate, FC - fiber coupler.

to be twice as big as in the  $z$  direction, so the cooling and trapping forces are equal in all three dimensions. Cooling beams for both species are going through the same PM fiber with perpendicular polarizations. It is necessary to carefully divide these beams into three pairs of beams, one pair for each direction. This setup is presented in Fig. 4.8. Cooling and repumping beams are co-propagated on the first PBS. Half-waveplates before the first PBS are adjusted so the cooling and repumping beams are divided in a 50:50 ratio. After first PBS, polarizations of cooling beams (and repumping beams) are the same for both isotopes, but polarizations between cooling and repumping beams are here perpendicular. On the second set of half-waveplates which separates beams for  $\pm x$  and  $+z$  direction, and  $\pm y$  and  $-z$  direction we adjusted them so the cooling beams are separated into 40:10 ratio. Consequentially, repumper beams are separated into a 10:40 ratio on the same PBS due to the orthogonal polarization. On the last set of half-waveplates, we adjusted them so the ratio between two cooling beams for  $\pm x$  and  $\pm y$  direction is 20:20. Repumping beams are separated in a 5:5 ratio on the same set of half-

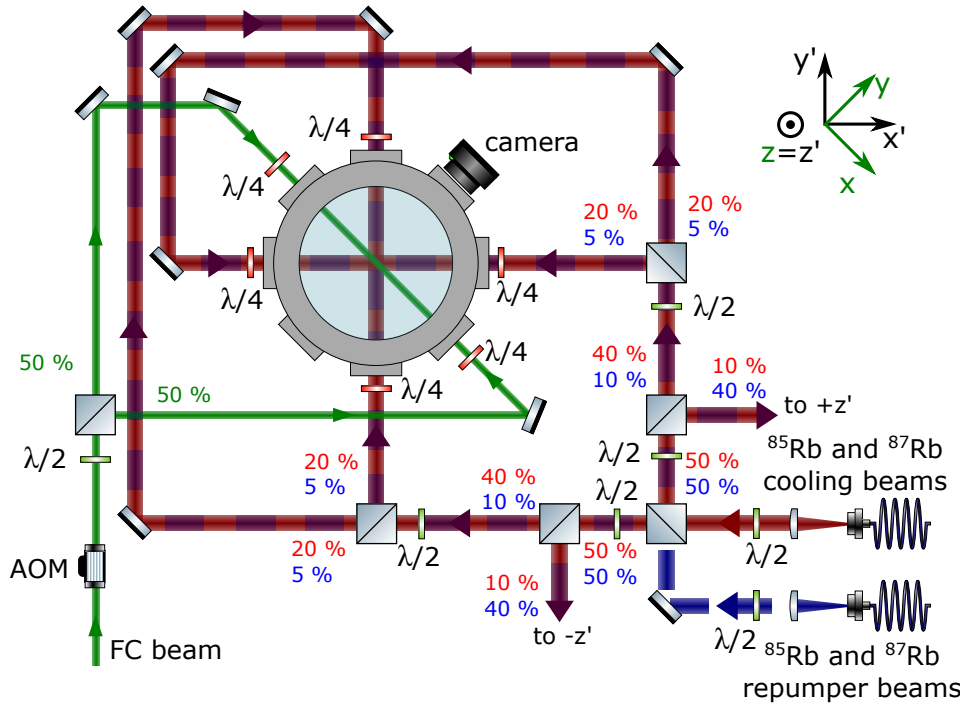


Figure 4.8: Schematic setup of the optics around vacuum chamber for dual-species cooling. The intensity ratios of the cooling (repumping) beams in  $x$ ,  $y$ , and  $z$  directions are shown in red (blue). Abbreviations used: M - mirror, L - lens, PBS - polarizing beam splitter, AOM - acousto-optics modulator,  $\lambda/2$  - half-waveplate,  $\lambda/4$  - quarter-waveplate, FC - fiber coupler. Taken from [58].

waveplates and PBS. To summarize, we have divided cooling and repumping beams for both species in the same ratio, which is  $\pm x : \pm y : \pm z = 20 : 20 : 10$  for cooling beams, and  $\pm x : \pm y : \pm z = 5 : 5 : 40$  for repumping beams. From here we see that the repumping beams are propagating dominantly through the  $\pm z$  direction.

Each of these six beams is going through a quarter-waveplate, which converts linear polarization into the circular polarization necessary for trapping the atoms in the center of the vacuum chamber.

Frequency comb beams are propagating in the  $xy$  plane, at  $45^\circ$  to the MOT beams. They are in counter-propagating configuration with  $\sigma^+ \sigma^-$  polarizations. Their switching is controlled with an AOM and a mechanical shutter. More about the mechanical shutter and its characteristics can be found in [57]. For the measurement of the radiation pressure force, one of the FC beams is blocked with a beam blocker.

## 4.4 Dual MOT generation

To demonstrate laser cooling with a frequency comb of two rubidium isotopes we first have to generate pre-cooled clouds of both species. Due to the very low power per comb mode of our frequency comb, of less than  $1 \mu\text{W}$ , it is not possible to demonstrate cooling from the thermal vapor, so we first have to generate precooled clouds at a temperature above the Doppler limit temperature.

Since cooling beams (and repumping beams) for both isotopes are propagating through the same PM fiber and the ratios between six beams is very carefully adjusted, clouds of both rubidium isotopes are loading at the same point and they occupy the same space in the vacuum chamber.

The initial conditions for the two rubidium isotopes are chosen so there is a slight difference in temperature for these two isotopes. The temperatures of cold clouds are determined by the powers of cooling beams and detunings of cooling lasers from respective cooling transitions. Powers at the fiber coupler output for the cooling beam for  $^{85}\text{Rb}$  is 27 mW and for the  $^{87}\text{Rb}$  is 40 mW. Powers of the repumping beams for  $^{85}\text{Rb}$  and  $^{87}\text{Rb}$  are 2.8 mW and 2.2 mW, respectively. Cooling and repumping beams have gaussian spatial profiles with a FWHM of 12 mm.

To achieve temperatures above the Doppler limit temperature, loading of the cold clouds is achieved in two stages. In the first stage detunings of cooling beams are chosen so the number of atoms in the trap is maximized. After this stage temperatures of both isotopes are very close to the Doppler limit, so we use the second stage to fine-tune the temperature of both isotopes. In this stage detunings of cooling beams are closer to the resonance so the temperature of clouds is increased, whereas the loss of atoms from the trap is negligible.

The first stage is 1.3 s long, where the detuning of the cooling beam for  $^{85}\text{Rb}$  is  $-1.7\Gamma$ , and the detuning of the cooling beam for  $^{87}\text{Rb}$  is  $-3.3\Gamma$ . Detunings are expressed in the units of excited state decay rate, which is  $\Gamma = (2\pi \cdot)6.07 \text{ MHz}$  for both Rb isotopes [38, 39]. The second stage is 0.1 ms long and the detuning of the cooling beam of  $^{85}\text{Rb}$  is  $-\Gamma$  and of  $^{87}\text{Rb}$  is  $-2.6\Gamma$ . Using this loading scheme we simultaneously load about  $1 \cdot 10^6$   $^{85}\text{Rb}$  atoms at  $(210 \pm 20) \mu\text{K}$  and about  $3 \cdot 10^6$   $^{87}\text{Rb}$  atoms at  $(260 \pm 10) \mu\text{K}$ .

These parameters are typical for the experiment, but with a slight change of the detunings in the second stage, we can fine-tune temperatures of clouds in the range of  $200 - 300 \mu\text{K}$ . Radii ( $1/e^2$ ) of the cold clouds of both rubidium isotopes are around 0.8 mm. Due to the careful alignment, we estimate that centers of mass of  $^{85}\text{Rb}$  and  $^{87}\text{Rb}$  atomic clouds overlap to within 5 % of their radii.

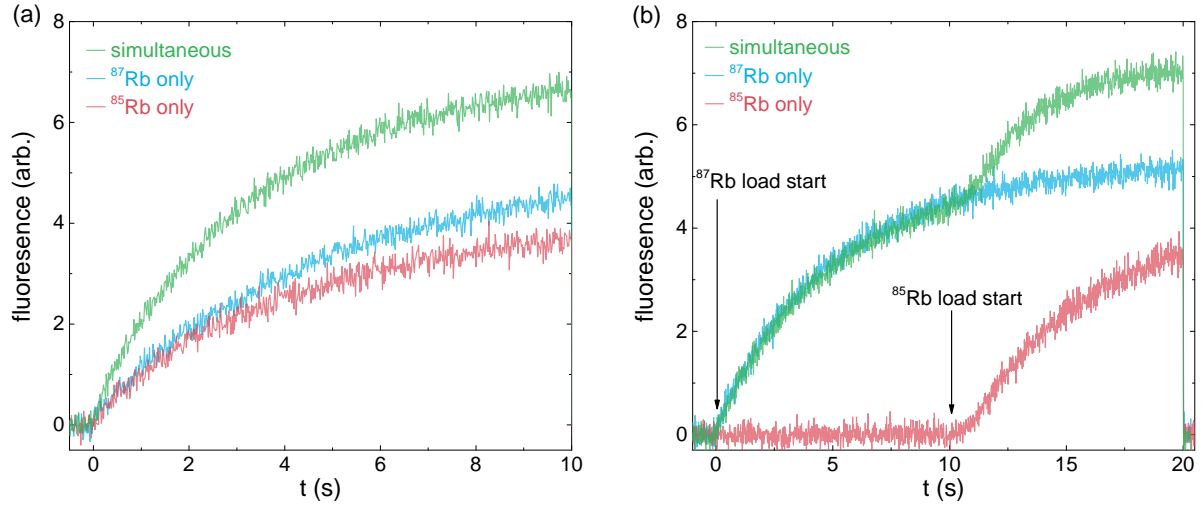


Figure 4.9: Simultaneous loading of two Rb isotopes MOT. Loading of each isotope separately, as well as simultaneous loading of both isotopes, is presented. Fluorescence is obtained from the integration of the cloud fluorescence images taken with the camera as a function of time. (a) Loading of both Rb isotopes starts at the same time  $t = 0$ . (b) Loading of  $^{87}\text{Rb}$  atoms starts at  $t = 0$  and the loading of the  $^{85}\text{Rb}$  starts at  $t = 10$  s. In both loading schemes simultaneous fluorescence is smaller than the net sum of individual fluorescence signals, which is a consequence of hetero-isotope collisions in the cold cloud.

Fig. 4.9 presents the loading curves for the cold  $^{85}\text{Rb}$  and  $^{87}\text{Rb}$  clouds. The fluorescence signal is captured with a camera during the MOT loading. To get the fluorescence signal, individual frames are integrated over the acquired image of the clouds.

Fig. 4.9(a) presents the cloud fluorescence when individual isotopes are loading and when both isotopes are loading simultaneously. Situation presented in Fig. 4.9(b) is loading of  $^{87}\text{Rb}$  from  $t = 0$  and loading of the  $^{85}\text{Rb}$  is delayed for 10 s for clarity. Fluorescence signal is smaller when both species are loading into the trap simultaneously, in comparison to the sum of individual fluorescence signals. This is an expected result since when different species are present in the trap, trap loss is increased due to the hetero-isotope collisions in the trap area [59]. In the experiment, loading is stopped at 1.3 s, before a stationary state is achieved.

#### 4.4.1 Imaging of cold clouds and temperature measurement

Imaging of cold clouds of rubidium atoms is done by collecting the atomic fluorescence when the imaging laser is exciting the atoms. Imaging lasers for both rubidium isotopes are the cooling lasers for respective isotopes. The detuning of the imaging laser for the  $^{85}\text{Rb}$  isotope is  $-0.8\Gamma$  and the detuning of the imaging laser for the  $^{87}\text{Rb}$  isotope is  $-2.6\Gamma$ .

The camera used to collect the fluorescence signal is a CMOS camera from IDS UI-3240CP-

NIR with enhanced quantum efficiency in the NIR spectrum. Quantum efficiency for this camera at 780 nm is around 60%. The camera is placed in the  $xy$  plane,  $45^\circ$  from the  $x$  and  $y$  direction of the cooling beams propagation. The camera is placed perpendicular to the frequency comb beams. Since the dead time between two consecutive frames of the camera is too long to capture fluorescence signals from both species in one measurement cycle, images of two isotopes are taken consecutively, where first  $^{87}\text{Rb}$  cloud fluorescence is measured, and then in next cycle  $^{85}\text{Rb}$  fluorescence is images. The loading procedure is the same for all measurements, frame-to-frame conditions do not change.

To create images of cold clouds on the camera sensor, we used macro objective MVL7000 from Thorlabs. Usual magnification used in the experiment is  $M = 0.25\times$ .

The temperature of the clouds is measured with the time-of-flight method [60, 61]. In the time-of-flight method, we take a series of cloud images after different times of the free expansion of the cloud. During the free expansion, all lasers are turned off and the cloud is expanding ballistically. The initial spatial distribution of atoms is expanding due to the finite velocity of atoms. After the time of flight  $t_{TOF}$ , or free expansion time, the atomic velocity distribution is mapped to the spatial distribution. The width of the atomic cloud as a function of free expansion time  $t_{TOF}$  is:

$$\sigma(t_{TOF}) = \sqrt{\sigma_0^2 + \frac{k_B T}{m} t_{TOF}^2}, \quad (4.3)$$

where  $\sigma_0$  is the initial spatial distribution width of the cloud,  $k_B$  is the Boltzmann constant and  $T$  is the temperature of the cold atomic cloud, and  $m$  is the mass of the atom.

The usual free expansion times we use to determine the initial temperature of cold clouds are 9 – 14 ms. After each expansion time, atoms are briefly excited (for 0.15 ms), and the resulting fluorescence is imaged with the camera. Examples of the  $^{87}\text{Rb}$  atomic cloud expansion and the 2D Gaussian fit are presented in Fig. 4.10. The measurement sequence is repeated ten times so we calculate the mean value and uncertainty of the widths.

From the measured cloud widths as a function of free expansion time, by fitting the Eq. (4.3) we calculate the temperature of the atomic cloud. An example of the measured cloud width as a function of free expansion time for the  $^{87}\text{Rb}$  atomic cloud is presented in Fig. 4.11. The temperature of the atomic cloud obtained from the Fig. 4.11 is  $(204 \pm 1) \mu\text{K}$ .

Initial temperatures of cold clouds of  $^{85}\text{Rb}$  and  $^{87}\text{Rb}$  have been measured 10 times consecutively to estimate the stability of the laser system and cloud generation process. Stability measurement is presented in Fig. 4.12.

From the Fig. 4.12 we see that temperature standard deviation of the  $^{87}\text{Rb}$  in comparison to

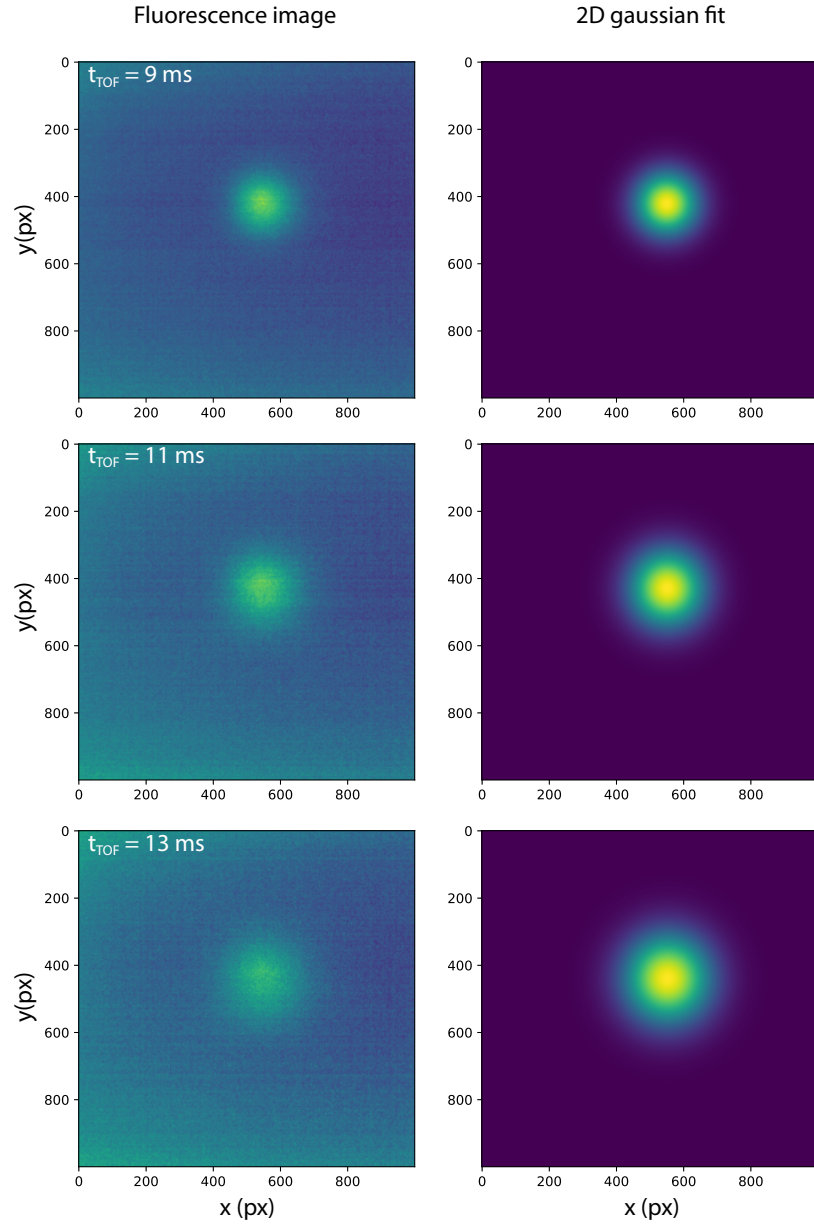


Figure 4.10: Fluorescence images of the  $^{87}\text{Rb}$  cloud for 9, 11, and 13 ms of free expansion time (left column). 2D Gaussian fits to the experimental data are shown in the right column.

the  $^{85}\text{Rb}$  is around 2.7 times smaller. This is a consequence of different cooling laser linewidths for  $^{87}\text{Rb}$  and  $^{85}\text{Rb}$ , where the  $^{87}\text{Rb}$  cooling laser has a linewidth of around 80 kHz and the  $^{85}\text{Rb}$  cooling laser has a linewidth of around 600 kHz.

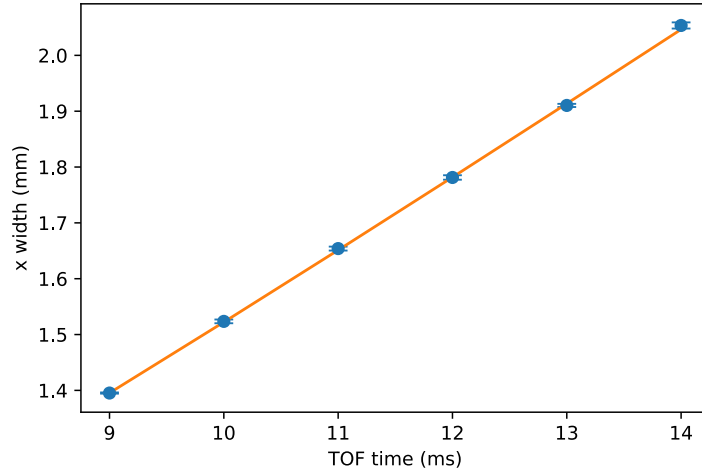


Figure 4.11: Measured width of the atomic cloud as a function of free expansion time, and fit to Eq. (4.3) to obtain the temperature of cold atoms.

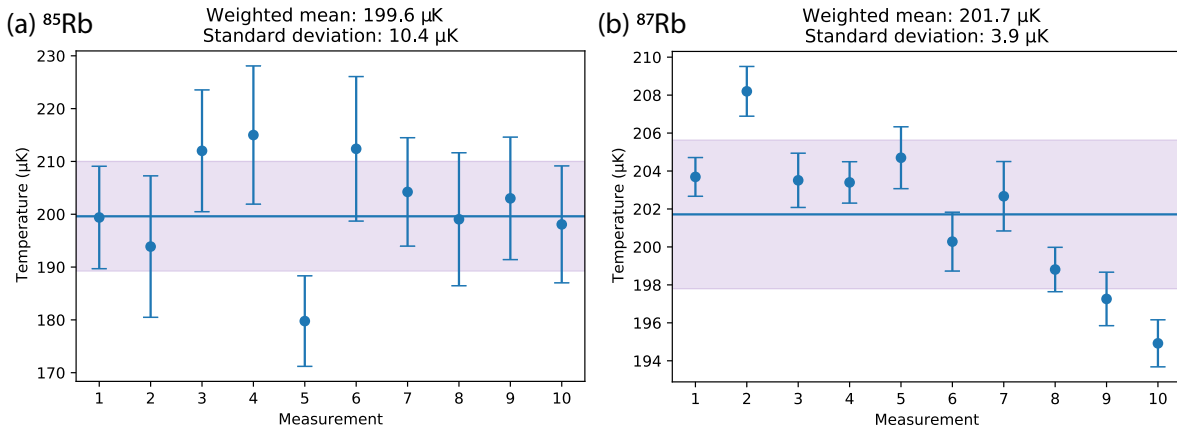


Figure 4.12: Measurement of temperature stability in ten independent measurements for (a)  $^{85}\text{Rb}$  and (b)  $^{87}\text{Rb}$  atoms. Weighted mean and standard deviation of the temperature is shown.

#### 4.4.2 Experiment control

In the experiment, precise time control is necessary to achieve cooling effects. Since atomic time dynamics is on the  $\mu\text{s}$  and  $\text{ms}$  time scale, it is necessary to control the time sequence very precisely. This is done using a DAQ card USB-6259 from National Instruments. The time sequence is stored in the card buffer and can be refreshed in  $5 \mu\text{s}$  intervals. The card has four analog input/output channels and 128 digital channels.

In the experiment, we have seven AOMs that are used to control the frequency and switching of the laser beams. Using the analog outputs of the DAQ card, we control the frequencies of the AOMs that determine the detuning of the cooling beams for both Rb isotopes, and the frequency

and power output of the repumping beam for  $^{85}\text{Rb}$  atoms. Digital channels are used for turning on and off AOMs to switch on/off beams of the frequency comb laser, cooling lasers for both Rb isotopes, and repumping laser for  $^{87}\text{Rb}$ . Other digital channels are used for the control of the magnetic field gradient, mechanical shutter, triggering the imaging camera.

The DAQ card is controlled using a self-written Matlab program, where we can setup and run experimental sequences. A picture of the program window used to control the experiment is presented in Fig. 4.13. In the figure, several labeled boxes are important for the experiment. In the green box, there is the main panel, where we setup the experimental protocol of the experiment. This includes setting up the sequence timing, laser detunings, and other triggers necessary for the experiment. In the TOF panel we setup a timing sequence for TOF measurement, as well as a number of repeated sequences. In the FC scan panel, we control the output from the DDS, which sets the beat frequency of the fc and cw laser to scan the FC detuning. In this panel number of repeated sequences is also chosen. DDS control panel is used to setup DDS output frequency, amplitude, and phase. The last important panel is the operation panel, where we can choose a predefined measurement type, DAQ refresh interval and we can start the experimental sequence. The predefined measurement type is programmed and can be easily modified.

To capture the images from the camera we use the software from the camera manufacturer. In the software, we can configure manually all camera settings like gain, framerate, exposure time, determine the area of interest, and many others.

Captured images of the cloud fluorescence are processed in self-written Python code, which determines the cloud widths, from which temperatures is calculated, the fluorescence amplitude, from which we estimate the number of atoms loaded [38, 39], and the center of mass of the cloud, from which forces exerted on atoms can be estimated.

### 4.4.3 Experimental protocol

In the main panel of the experiment control program, we define a timing sequence of the experiment. A defined protocol can be separated into several stages, as it is presented in Fig. 4.14. The experiment starts with the loading of both Rb isotopes simultaneously. In this stage, both cooling and repumping lasers for both species are switched on. This stage consists of two phases, described in previous sections. During this stage frequency comb beam is switched off.

At  $t = 0$  we switch off the cooling beams for both Rb isotopes, and turn on the frequency comb beam for different times of interaction with pre-cooled atoms. To achieve FC cooling, it was necessary to keep the cw repumpers switched on, since for the FC repetition frequency of 80.495 MHz there are no comb modes that are near-resonant to the repumping transitions in

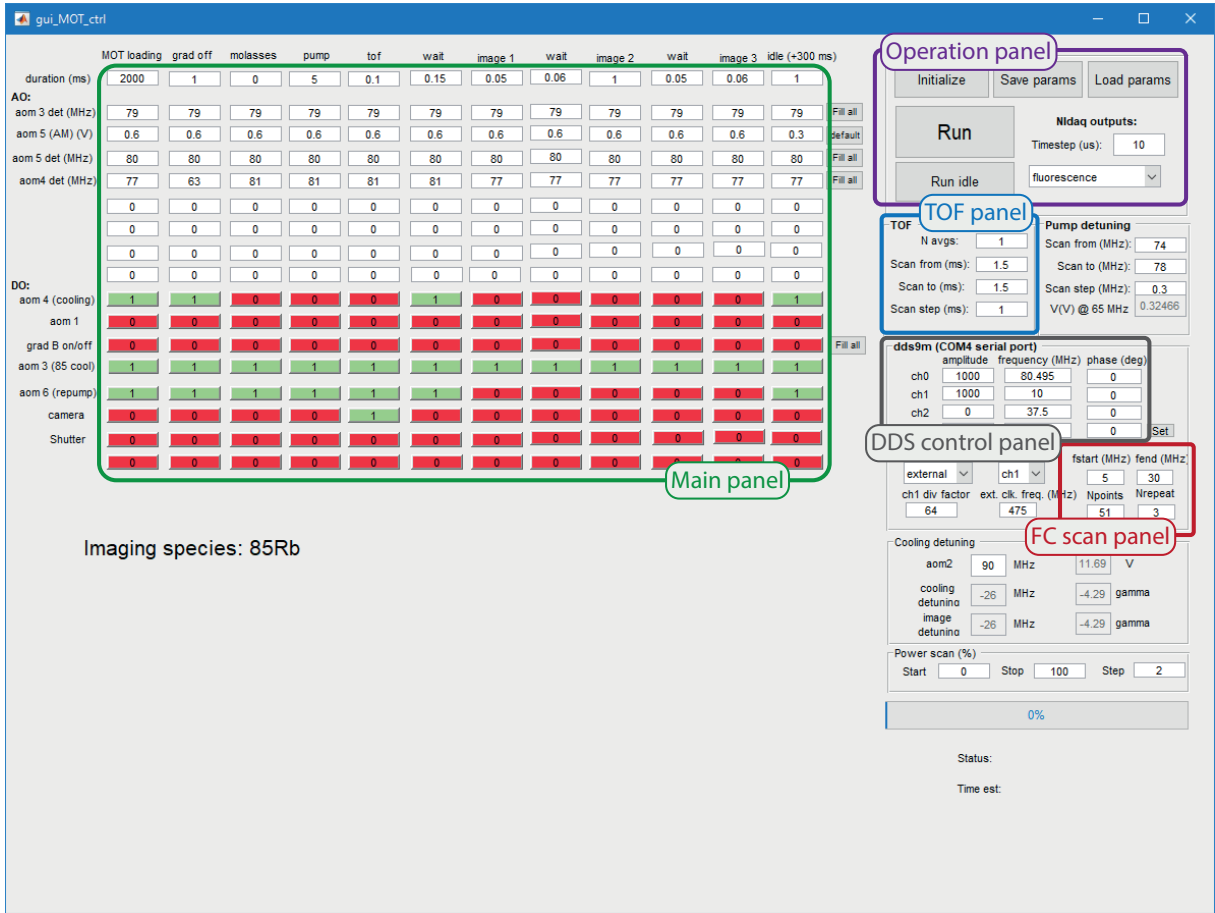


Figure 4.13: A window of the self-written program for experiment control with labeled important panels. In the main panel (green color) we define timing sequence, laser switching, and some detunings of laser beams. In the TOF panel (blue color) we define TOF measurement parameters. DDS control panel (gray color) is used to set DDS outputs amplitude, frequency, and phase. The FC scan panel (red color) sets the local oscillator frequency scan, which is used to scan the FC detuning. The operation panel (purple color) is used to choose the measurement type and run the experimental sequence.

both isotopes. For the measurement of simultaneous radiation pressure force, one FC beam is blocked, and for the measurement of simultaneous cooling, both beams are propagating.

After interacting with the FC beams for a specific time, the cloud is left to expand freely for  $t_{TOF}$ , with all laser beams turned off. After  $t_{TOF}$ , we briefly shine the cloud with the cooling and repumping laser of a specific isotope and image the cloud fluorescence. As mentioned earlier, only one Rb isotope can be imaged at a time, so the images of different Rb isotopes are taken consecutively, so the experimental procedure has to be repeated twice with the same parameters in order to gather data for both isotopes.

Throughout the whole experiment the magnetic field gradient is left switched on, due to the

slow decay of the eddy currents that are generated when the field is switched off, producing the time dependent magnetic field.

The experimental procedure is repeated several times to obtain the mean value of the measured values and their statistical uncertainty. Between consecutive running of the procedure, timing parameters can be changed inside the experiment control program, as well as the beat frequency of the frequency comb, to scan the detuning from the cooling transitions.

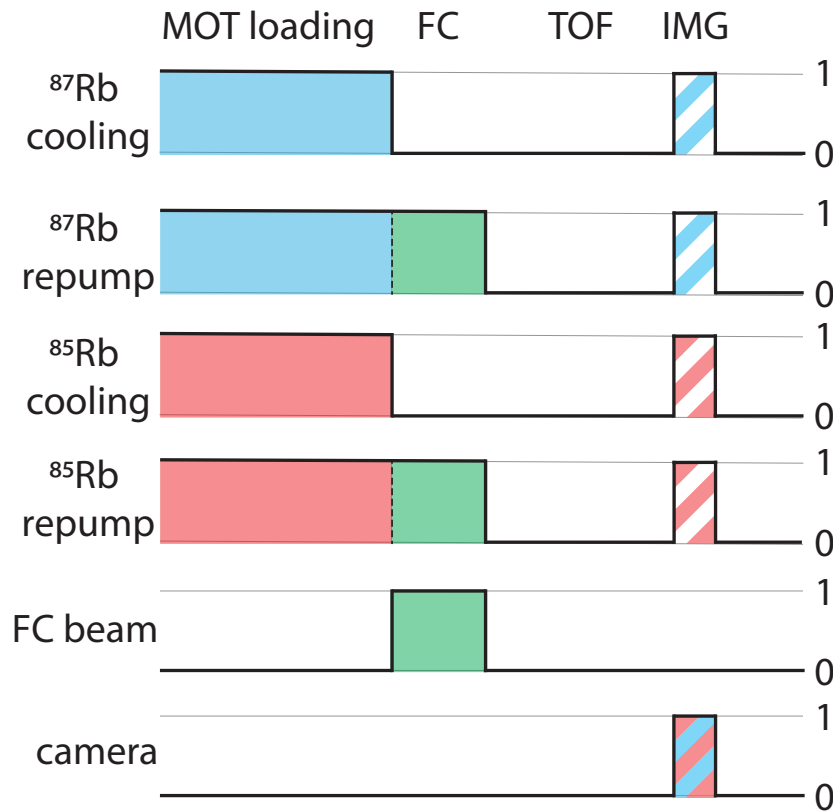


Figure 4.14: Protocol of the measurement. During the MOT loading stage, both cooling and repumping lasers are switched on. At  $t = 0$  we switch off cooling lasers and switch on FC beams. During the interaction with FC beams, repumper lasers are switched on. In the TOF stage, all lasers are switched off and the cloud is expanding freely. In the IMG phase we briefly shine the cloud with corresponding cooling and repumping lasers and image cloud fluorescence with a camera. The isotopes are imaged separately due to the experimental limitations.

## 4.5 FC radiation pressure force

To simultaneously excite both Rb isotopes, two or more comb modes must be close to the resonance with two or more transitions in Rb isotopes. In this section we will present the results of the simultaneous excitation of two Rb isotopes, using a single FC beam.

As we know from previous chapters, the whole frequency comb spectrum is defined with two RF frequencies, repetition frequency  $f_{rep}$  and carrier-envelope offset frequency  $f_0$ . These two frequencies are defining the relative positions of the comb modes with respect to atomic transitions. The repetition frequency of our frequency comb laser is  $f_{rep} = 80.495$  MHz, which can simultaneously excite the cooling transitions of both  $^{85}\text{Rb}$  and  $^{87}\text{Rb}$  isotopes. Frequency difference of the cooling transition in  $^{85}\text{Rb}$   $|F = 3\rangle \rightarrow |F' = 4\rangle$  and the cooling transition in  $^{87}\text{Rb}$   $|F = 2\rangle \rightarrow |F' = 3\rangle$  is 1126 MHz [38, 39] so the repetition frequency enables the excitation of both cooling transitions simultaneously.

Scheme of the frequency comb spectrum with respect to the atomic transitions for both Rb isotopes is presented in Fig. 4.15. In the experiment during the FC beam interaction with atoms, cw repumper lasers for both species are switched on to keep the populations of  $^{85}\text{Rb}$  atoms in the  $|F = 3\rangle$  ground state, and the populations of  $^{87}\text{Rb}$  atoms in the  $|F = 2\rangle$  ground state. Transitions from  $|F = 2\rangle$  for  $^{85}\text{Rb}$  and  $|F = 1\rangle$  for  $^{87}\text{Rb}$  do not contribute to the total radiation pressure force significantly for this repetition frequency, as there are no comb modes close to the resonance with the respective transitions. The interaction of the comb modes with  $|F = 2\rangle \rightarrow |F' = 1, 2, 3\rangle$  for  $^{85}\text{Rb}$  and  $|F = 1\rangle \rightarrow |F' = 0, 1, 2\rangle$  for  $^{87}\text{Rb}$  are exempt from the analysis.

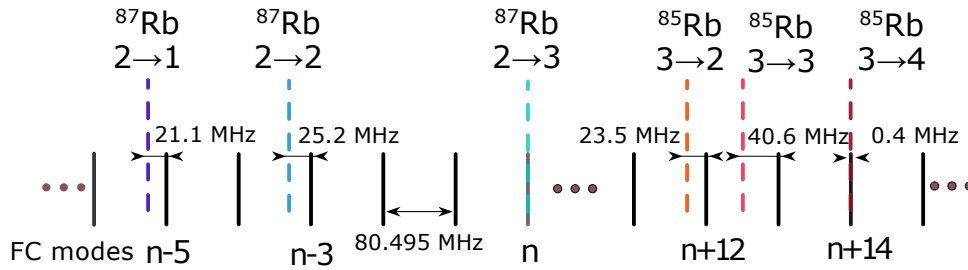


Figure 4.15: Scheme of the frequency comb modes with respect to  $^{85}\text{Rb}$  and  $^{87}\text{Rb}$  atomic transitions. The FC repetition frequency is  $f_{rep} = 80.495$  MHz and detuning of the  $n$ -th comb mode from the  $^{87}\text{Rb}$  cooling transition is 0. Simultaneously, the  $(n + 14)$ -th comb mode is 0.4 MHz blue detuned from the  $^{85}\text{Rb}$  cooling transition. Transitions from  $|F = 2\rangle$  for  $^{85}\text{Rb}$  and  $|F = 1\rangle$  for  $^{87}\text{Rb}$  are not considered. In the FC cooling conditions FC spectrum is  $\sim -\Gamma$  red detuned to satisfy the cooling condition for both isotopes.

In the case when the  $n$ -th comb mode is resonant with the  $|F = 2\rangle \rightarrow |F = 3\rangle$  transition of

the  $^{87}\text{Rb}$ , then the  $(n+14)$ -th comb mode is 0.4 MHz blue detuned from the  $|F=3\rangle \rightarrow |F=4\rangle$  transition of the  $^{85}\text{Rb}$  atom. Natural linewidth for both Rb isotopes is  $\Gamma = 6.07$  MHz [38, 39], so both of the cooling transitions can simultaneously be excited by the FC beam at this repetition frequency.

Radiation pressure force exerted on atoms by a FC beam is calculated from the measurement of the atomic cloud center of mass displacement from the initial position. Cloud is displaced due to the interaction with a frequency comb beam. At  $t = 0$ , when the cooling beams are turned off, the FC beam is switched on. During the interaction with an FC beam, cw repumping beams are left on. Repumping beams are predominantly in the  $z$  direction and have no measurable effect on the cloud displacement. FC beam interacts with both Rb isotopes simultaneously for 2 ms, so the center of mass of clouds are accelerating due to the exerted force. After the interaction, the FC beam and cw repumping beams are switched off, so clouds center of mass are moving with a constant velocity. Clouds are moving freely for 2 ms, after which we take images of the cold clouds. The total displacement of the cloud's center of mass is:

$$\Delta x = \frac{F}{m} \left( \frac{1}{2} t_{INT}^2 + t_{INT} t_{TOF} \right), \quad (4.4)$$

where  $F$  is the force exerted on atoms,  $m$  is the mass of the atom,  $t_{INT}$  is the interaction time with the FC beam, and  $t_{TOF}$  is the time of free expansion.

The average power of the FC beam on the atoms is 10 mW with a beam FWHM of 2.7 mm. Power and intensity per comb mode are around  $0.3 \mu\text{W}$  and  $3.6 \mu\text{W}/\text{cm}^2$  respectively. Power per comb mode is calculated from the measurement of average power and the spectrum of the FC beam, Fig. 4.4. Scan of the FC radiation pressure force as a function of detuning of the  $n$ -th comb mode from the  $^{87}\text{Rb}$  cooling transition is done by changing the beat frequency for comb stabilization. In our scheme, the beat frequency can be changed continuously in the range of 5 – 30 MHz by changing the frequency of the local oscillator. To cover one  $f_{rep}$  range of detunings we have to measure four separate scans with different cw reference laser frequency shifts. Cw reference laser frequency shift is done by changing the frequency on the AOM setup on the spectroscopy beam, as well as the respective change of the AOM on the experiment path so the initial conditions for MOT loading stay the same. Measurement is repeated six times to obtain the mean value and the experimental uncertainty.

Examples of the clouds center of mass displacement is presented in Fig. 4.16.  $^{85}\text{Rb}$  and  $^{87}\text{Rb}$  clouds displacements at three detunings of the  $n$ -th comb mode from the  $^{87}\text{Rb}$  cooling transition are shown. White dashed line in the figure presents the initial center of mass for both Rb isotopes. Red dashed line presents the center of mass of the  $^{87}\text{Rb}$  and orange dashed line

the center of mass of the  $^{85}\text{Rb}$  isotope. In the figure in the top row there are images of the  $^{87}\text{Rb}$  isotope, and in the bottom row are images of  $^{85}\text{Rb}$  isotope. Images in the middle present images of both clouds imaged simultaneously. From this image, it is clear that clouds of both isotopes are overlapped and can not be distinguished. To distinguish separate clouds they have to be imaged separately, as described in the previous section.

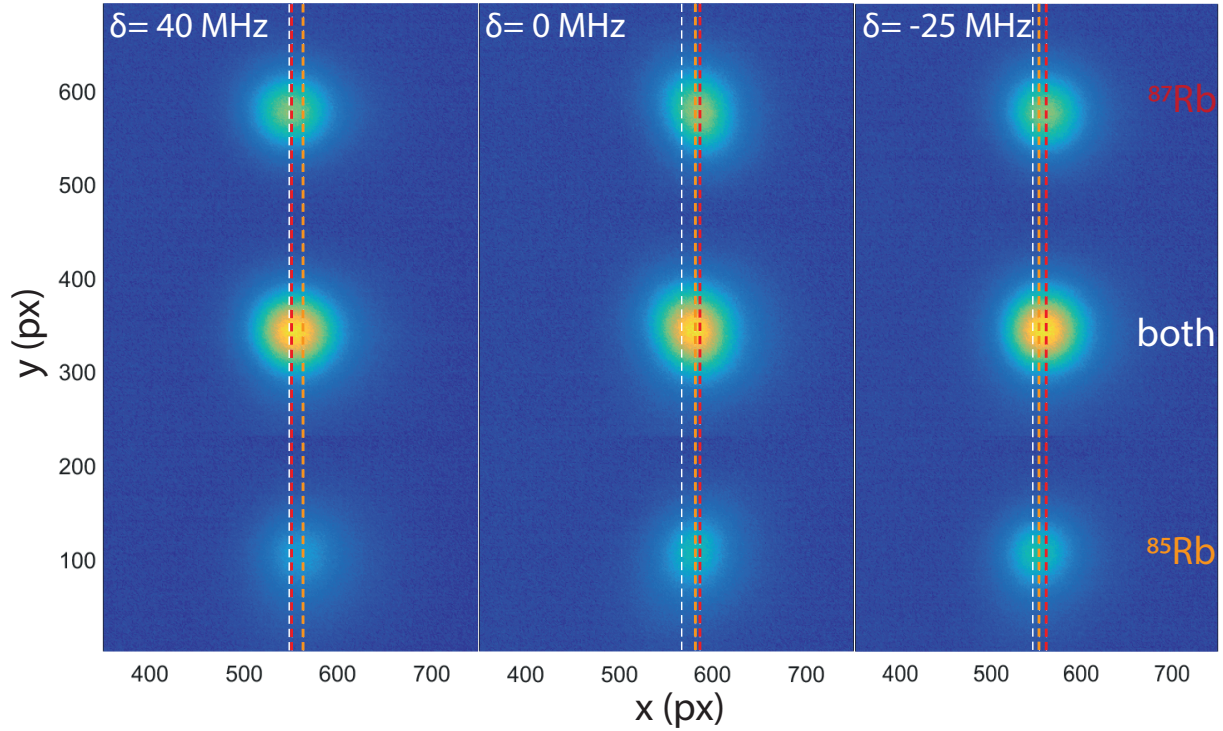


Figure 4.16: Displacement of the cloud's center of mass due to the FC beam interaction for three different detunings. In the top row are presented images of the displaced  $^{87}\text{Rb}$  atomic cloud and in the bottom row of the  $^{85}\text{Rb}$  cloud. In the middle row, there are images of the simultaneously imaged clouds of both isotopes. The white dashed line represents the initial center of mass for both clouds, and the red and orange dashed lines represent the displaced center of mass of  $^{87}\text{Rb}$  and  $^{85}\text{Rb}$  atomic clouds.

In the Fig. 4.16 for detuning of  $\delta = 40$  MHz, only the cloud of  $^{85}\text{Rb}$  is displaced from the initial position. This displacement is the consequence of the  $(n + 12)$ -th comb mode resonant interaction with the  $^{85}\text{Rb}$   $|F = 3\rangle \rightarrow |F' = 3\rangle$  transition. At this detuning all comb modes are far detuned from respective transitions in the  $^{87}\text{Rb}$  isotope, so there is no significant change in the cloud's center of mass.

For detuning of  $\delta = 0$  MHz, it is clear that both clouds are significantly displaced from the initial position. For this detuning  $n$ -th comb mode is resonant with  $^{87}\text{Rb}$   $|F = 2\rangle \rightarrow |F' = 3\rangle$  transition and the  $(n + 14)$ -th comb mode is 0.4 MHz blue detuned from the  $^{85}\text{Rb}$   $|F = 3\rangle \rightarrow |F' = 4\rangle$  transition. This is the case where displacement of the clouds of both isotopes is the

greatest.

The last detuning presented in Fig. 4.16 is  $\delta = -25$  MHz. In this case both clouds are displaced from the initial position, but the displacement of the  $^{87}\text{Rb}$  cloud is bigger than the  $^{85}\text{Rb}$  cloud. This is due to the resonant interaction of the  $(n - 3)$ -rd comb mode with  $^{87}\text{Rb}$   $|F = 2\rangle \rightarrow |F' = 2\rangle$  transition and near resonant interaction of the  $(n + 12)$ -th comb mode with  $^{85}\text{Rb}$   $|F = 3\rangle \rightarrow |F' = 2\rangle$  transition.

The simultaneous radiation pressure force as a function of detuning of the  $n$ -th comb mode from the  $^{87}\text{Rb}$  cooling transition is presented in Fig. 4.17. For all data points presented in the figure, the uncertainties of the radiation pressure forces are smaller than the data points and are not presented here. Besides the experimental results, the theoretical calculation of the force is also shown. The force is calculated numerically using the optical Bloch equations that describe the interaction of six-level atoms with a frequency comb and the Ehrenfest theorem. Details about the calculation can be found in [7, 58].

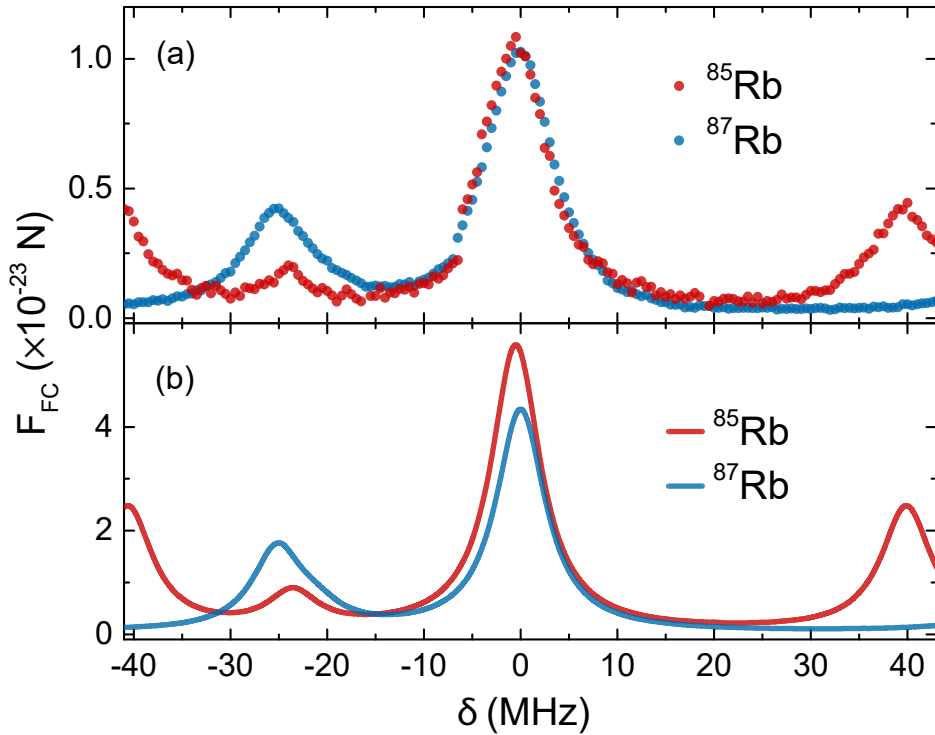


Figure 4.17: FC radiation pressure force exerted on atoms of both Rb isotopes simultaneously as a function of the detuning of the  $n$ -th comb mode from the  $^{87}\text{Rb}$  cooling transition. (a) Experimental results (b) Theoretical calculations.

Comparing the experimental results and the theoretical calculation, the agreement is satisfactory. Relative positions of the peaks arising from the comb interaction with atoms as well

as the ratios between them are properly reproduced for both Rb isotopes. In the experimental results, the measured force is about four times smaller and the linewidth is about 1 MHz broadened. In theoretical calculations effects of the stray magnetic field, finite comb linewidth, and spatial profile of the beams are not included, so the discrepancy between experiment and calculation can be attributed to these effects. In recent literature by our group, we shown that the broadening of the linewidth is due to the finite optical depth of the cloud [62].

The radiation force peaks at  $\delta = 0$  are the same for both Rb isotopes in the measurement, but in the calculations, there is a difference between the peak heights. Powers of the  $n$ -th and  $(n + 14)$ -th comb modes are approximately the same, so the radiation force peaks are of different heights due to the difference in transition dipole moment. The transition dipole moment of the cooling transition for  $^{85}\text{Rb}$  isotope is  $\sqrt{3/2} \cdot 3.584 \cdot 10^{-29}$  Cm [38], while the transition dipole moment of the  $^{87}\text{Rb}$  cooling transition is  $\sqrt{7/6} \cdot 3.584 \cdot 10^{-29}$  Cm [39]. In the experiment, due to the presence of the stray magnetic fields and  $\sigma^+$  circularly polarized FC beam, stretched transitions  $|F = 3; m_F = +3\rangle \rightarrow |F = 4; m_F = +4\rangle$  for  $^{85}\text{Rb}$  and  $|F = 2; m_F = +2\rangle \rightarrow |F = 3; m_F = +3\rangle$  for  $^{87}\text{Rb}$  dominate all other Zeeman transitions. For both isotopes transition dipole moments for these stretched transitions have the same value of  $\sqrt{1/2} \cdot 3.584 \cdot 10^{-29}$  Cm [38, 39], so the resulting force is equal for both isotopes. It is possible to make a more detailed theoretical model which would include all Zeeman components but it is cumbersome and out of the scope of this thesis.

Peak at the  $\delta \approx -25.5$  MHz for  $^{87}\text{Rb}$  is the consequence of the FC interaction of  $(n - 3)$ -rd comb mode with  $|F = 2\rangle \rightarrow |F' = 2\rangle$  and  $(n - 5)$ -th mode interaction with  $|F = 2\rangle \rightarrow |F' = 1\rangle$  transition. For  $^{85}\text{Rb}$  peak at  $\delta \approx -23.5$  MHz is arising from the interaction of  $(n + 12)$ -th comb mode with  $|F = 3\rangle \rightarrow |F' = 2\rangle$  transition. Other two peaks for  $^{85}\text{Rb}$  at  $\delta \approx -40$  MHz and  $\delta \approx 40$  MHz are result of the  $(n + 13)$ -th and  $(n + 12)$ -th comb modes interaction with the  $|F = 3\rangle \rightarrow |F' = 3\rangle$  transition. This is a characteristic signature of the FC interaction with atoms, where the radiation pressure force profile is repeated with  $f_{rep}$ .

## 4.6 Simultaneous dual species laser cooling with a frequency comb

Cooling of atoms happens when a laser is red detuned from the cooling transition, and this also applies for cooling with a frequency comb laser. In this work, we demonstrate simultaneous FC cooling of two Rb isotopes in 1D with counter-propagating  $\sigma^+\sigma^-$  polarized beams. The power of the FC beams on the atoms is 10 mW per beam, where beam FWHM is 2.7 mm. This gives the power of a single comb mode of  $0.3 \mu\text{W}$  or intensity of  $3.6 \mu\text{W}/\text{cm}^2$ . FC beams are interacting with pre-cooled clouds of  $^{85}\text{Rb}$  and  $^{87}\text{Rb}$  atoms for 3 ms. TOF images are taken for 6 – 11 ms of free expansion. Initial temperatures of Rb isotopes are  $T_{\text{init}} = (210 \pm 20) \mu\text{K}$  for  $^{85}\text{Rb}$  and  $T_{\text{init}} = (260 \pm 10) \mu\text{K}$  for  $^{87}\text{Rb}$ . Different initial temperatures are setup so the temperatures can be distinguished in the graph.

Fluorescence images of both Rb isotopes under the influence of two counter-propagating FC beams in 1D are presented in Fig. 4.18. Individual images of both species cooled with a FC simultaneously, as well as images of both species taken simultaneously are shown. In comparison to Fig. 4.10, where the cloud has a round shape, here we see that clouds have an elliptical shape, where the compressed dimension is the dimension of FC beams propagation. Temperature is calculated from the expansion of the clouds widths as the function of free expansion time and fitting to Eq. (4.3).

Cooling of the clouds of both Rb isotopes is observed when the  $n$ -th and  $(n + 14)$ -th comb modes are red detuned from the respective cooling transitions. The temperature of the clouds achieved by simultaneous interaction of FC beams with  $^{85}\text{Rb}$  and  $^{87}\text{Rb}$  atoms as a function of the  $n$ -th comb mode detuning from the  $^{87}\text{Rb}$  cooling transition is presented in Fig. 4.19.

As can be seen from the figure, minimum temperature is achieved at  $\delta \approx -\Gamma/2$  and is close to the Doppler temperature of  $T_D = 145.57 \mu\text{K}$  [38, 39]. Minimum measured temperature for  $^{85}\text{Rb}$  is  $(140 \pm 15) \mu\text{K}$ , and for  $^{87}\text{Rb}$  is  $(169 \pm 10) \mu\text{K}$ . The minimum measured temperature for  $^{87}\text{Rb}$  is slightly higher than for the  $^{85}\text{Rb}$  due to the higher initial temperature so the steady-state temperature has not yet been achieved in the measurement. For detunings closer to the resonance and for blue detunings the final temperature is increased as is expected. When the same initial temperatures for both Rb isotopes are adjusted in the experiment, the same minimum temperature close to the Doppler limit is achieved.

The temperature obtained for the  $\text{Lin} \perp \text{Lin}$  polarized frequency comb beams as a function of comb detuning has the same qualitative shape as is presented in Fig. 4.19 for  $\sigma^+\sigma^-$  polarizations. The minimum measured temperature for perpendicular linear polarization of the comb beams is close to the Doppler limit for both isotopes, as is expected.

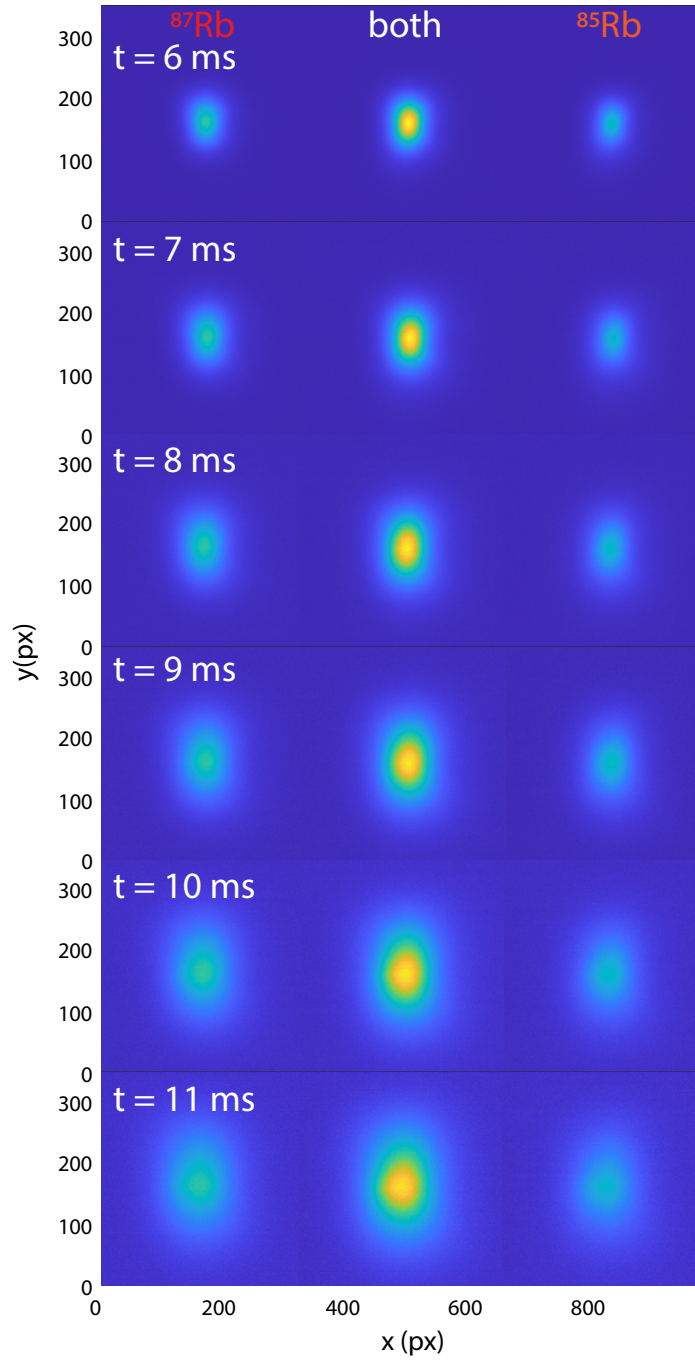


Figure 4.18: False-color images of the cold clouds of  $^{87}\text{Rb}$  (first column) and  $^{85}\text{Rb}$  (third column) atoms at 6-11 ms of free expansion after cooling with two counter-propagating FC beams. Images of two species taken simultaneously are shown in the middle column. FC beams are propagating in the x direction, where clouds are compressed and temperature is measured.

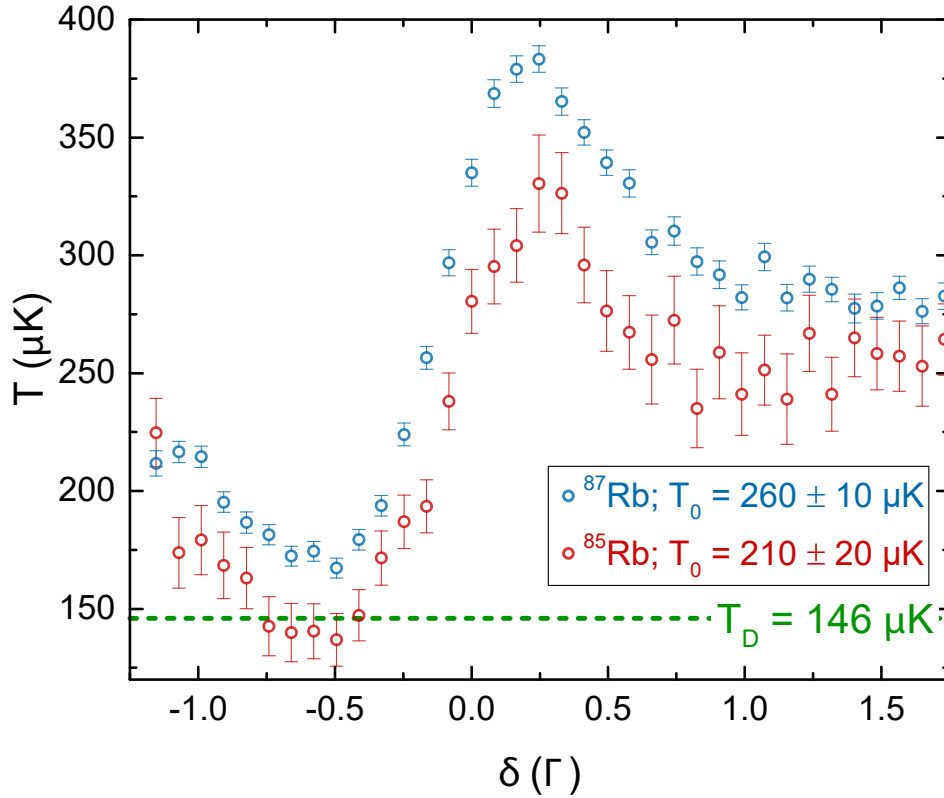


Figure 4.19: Simultaneous temperatures of cold atoms of  $^{85}\text{Rb}$  and  $^{87}\text{Rb}$  as a function of the  $n$ -th comb mode detuning from the  $^{87}\text{Rb}$  cooling transition. Minimum temperature for  $^{85}\text{Rb}$  is  $(140 \pm 15) \mu\text{K}$ , and for  $^{87}\text{Rb}$  is  $(169 \pm 10) \mu\text{K}$  at  $\delta = -\Gamma/2$ . Both temperatures are very close to the Doppler limit temperature, indicated by the green dashed line.

Temperatures lower than the Doppler limit have not been achieved in this work due to the low power per comb mode available from our FC laser. For higher intensities of the comb modes, it should be possible to demonstrate sub-Doppler cooling [63] and direct cooling from the background vapor [15].

In Fig. 4.20 we present temperatures of both Rb isotopes cooled simultaneously as a function of the FC interaction time. During the interaction time, cw repumper lasers for both Rb isotopes are switched on to keep the atoms in the cooling cycle. For this set of measurements, the duration of the comb interaction with the atoms  $t_{FC}$  was  $0.5 - 3.5$  ms. Measurements presented for  $t_{FC} = 0$  are the initial temperature measurements. In the experiment FC interaction times longer than  $3.5$  ms are impractical. Due to the limited power of the FC laser, FC beams are rather small in comparison to the MOT beams. FC beams are still bigger than the initial cold cloud, but for  $t_{FC} > 3.5$  ms the cloud size in the dimensions perpendicular to the comb beams becomes larger than the size of the beams. As a result, the cloud is no longer elliptical

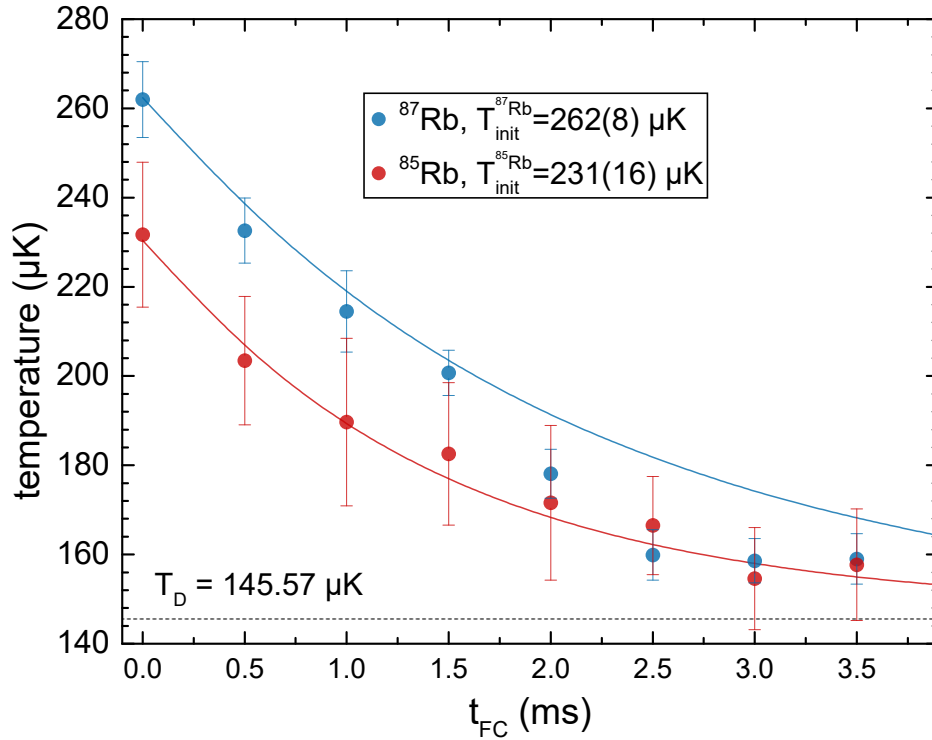


Figure 4.20: Simultaneous temperatures of cold clouds of  $^{85}\text{Rb}$  and  $^{87}\text{Rb}$  atoms as a function of FC beams interaction time. A theoretical calculation of the temperatures dependence on the interaction time for two-level atoms and cw laser interaction is presented with solid lines (see text for more details). Doppler temperature limit is presented with dashed line.

and the determination of the cloud width and consequentially the temperature is ambiguous.

The expansion times used for this measurement are from  $(9 - t_{FC})$  ms to  $(14 - t_{FC})$  ms so the time from the MOT beams switch off is the same for all interaction times. The expansion time in this measurement is changed as we changed the interaction time so the signal-to-noise ratio in images taken is approximately the same for all interaction times.

The solid lines in Fig. 4.20 are theoretical estimations of the cold cloud temperatures as functions of frequency comb interaction time. This estimation is based on the simple model of the cw laser interaction with a two-level atom. In this model, we numerically solve the Fokker-Planck equation where the radiation pressure force and diffusion coefficient are expressions for the low-intensity theory for two-level atoms in 1D [33]. Details about this model can be found in [7]. Theoretical results presented in Fig. 4.20 are calculated using a cw laser with intensity of  $7.2 \mu\text{W}/\text{cm}^2$ , the same as the power per comb mode in the experiment, transition dipole moments of  $\sqrt{3/2} \cdot 3.584 \cdot 10^{-29}$  Cm and  $\sqrt{7/6} \cdot 3.584 \cdot 10^{-29}$  Cm for  $^{85}\text{Rb}$  and  $^{87}\text{Rb}$  respectively and detuning of  $\delta = -\Gamma/2$ . Theoretical curves describe the measured temperatures as a function

of FC interaction time well. This result is also confirming the analogy between frequency comb and continuous-wave laser cooling, as is expected in the case of a cooling regime when the repetition period is smaller than the excited state lifetime and coherent accumulation of population is achieved.

## 4.7 Conclusion

In this chapter we have presented simultaneous cooling of two rubidium isotopes,  $^{85}\text{Rb}$  and  $^{87}\text{Rb}$  with a single frequency comb laser source. To the best of our knowledge, this is the first demonstration of the simultaneous multi-species laser cooling with a frequency comb laser.

Cooling is achieved in 1D, with counter-propagating FC beams in  $\sigma^+\sigma^-$  configuration of polarization. By comparing the FC cooling of a single Rb isotope [7] and simultaneous cooling of two Rb isotopes, we conclude that the simultaneous cooling does not affect the cooling of each isotope. Results also suggest that other far detuned comb modes do not change the final temperature of the FC cooling process. Used repetition period in the experiment is smaller than the excited state lifetime, so the coherent accumulation of population is achieved. In this FC cooling regime, each mode of the frequency comb is analogous to a continuous-wave laser, as is demonstrated in this work.

With advances in the novel frequency comb technology, power per comb mode should increase significantly, thus enabling the sub-Doppler cooling and direct cooling from the background vapor using a frequency comb. The use of the FC as a laser cooling source should contribute to the development of the multi-species atom interferometers for ground and space applications, investigation of the multi-species interactions, and formation of the heteronuclear cold molecules.

The successful use of a frequency comb in laser cooling paves a way toward laser cooling of species that can not be cooled using standard continuous-wave lasers, where the most desired species would be hydrogen, carbon, nitrogen, and oxygen.

# Chapter 5

## EIT quantum memories with rubidium vapor

In this chapter, I will present the theory and the results of the recent experiment on the electromagnetically induced transparency (EIT) effect and the storage of the light pulses in the quantum memory. Quantum memories (QM) can be realized in many different mediums: solid-state mediums, vapor mediums, or even cold atoms. The advantage of the vapor QMs is the simplicity of the experiment. For each medium, there are a lot of different schemes a QM can be realized. Some of these are Gradient echo memory [25], Raman-based memory [26], atomic frequency comb memory [27], memory based on the EIT effect [64], and hybrid memory schemes [65]. Advantages of the EIT-based QM in the atomic vapor are in its efficiency, high memory efficiency, and very long storage times [66].

### 5.1 Theory of EIT and quantum memories

When the near resonant probe beam goes through a medium it is absorbed. In a highly controlled conditions using additional laser beam called the control beam, it is possible to achieve full transmission of the probe beam. This effect is called Electromagnetically induced transparency (EIT). There are several different realizations of the EIT, the *lambda* scheme, the *vee* scheme and the *ladder* scheme [30]. EIT scheme names come from the configuration of probe and control beams with respect to atomic energy level structure. In the experiment, we used *lambda* EIT scheme so I present here the theory of the three-level atom in the *lambda* excitation scheme.

Storage of the probe pulses inside the medium is a consequence of the EIT. In EIT, the group velocity of the probe pulse in the medium is significantly reduced and this effect is called

slow light [67]. By rapidly changing the EIT conditions, by switching the control beam off, the group velocity of the probe pulse can be reduced to zero, so the pulse is stored inside the medium. To read the stored pulse, the control beam is switched on, and the pulse is released from the medium [66].

### 5.1.1 Electromagnetically induced transparency

To describe the effect of electromagnetically induced transparency (EIT) we will look at the interaction of two laser beams and a three-level atom. This three-level atom has two ground states which are dipole forbidden, and one dipole allowed excited state. Scheme of the energy level structure of the atom and used laser beams is presented in Fig. 5.1.

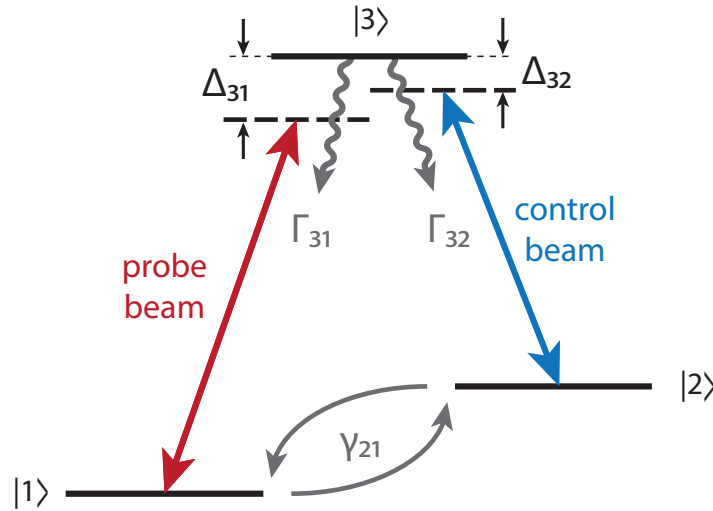


Figure 5.1: Energy level structure of a three-level atom with marked probe and control laser beams. Adapted from [68].

Two laser beams are necessary to achieve the EIT effect, one strong control laser beam, which is tuned to the  $|2\rangle \rightarrow |3\rangle$  transition with the frequency  $\omega_c$ , and a weak probe laser beam, tuned to the  $|1\rangle \rightarrow |3\rangle$  transition with frequency  $\omega_p$ . We define detunings of control and probe beams as  $\Delta_c = \omega_c - \omega_{32}$  and  $\Delta_p = \omega_p - \omega_{31}$ .  $\Gamma_{31}$  and  $\Gamma_{32}$  are decay rates from the excited state, and  $\gamma_{21}$  is the coherence decay rate of the dipole-forbidden  $|1\rangle \leftrightarrow |2\rangle$  transition. This coherence decay rate is called the ground state decoherence rate and is much smaller than the  $\Gamma_{31}$  and  $\Gamma_{32}$  for dilute gases.

We need to derive the optical Bloch equations for populations and coherence terms to describe the EIT effects. The procedure is similar to the derivation for two-level atoms interaction with a single cw laser presented in Chapter 2. In literature, there are many examples of the

derivation of the OBEs [30, 69], so here I will provide only the main results of the derivation. The derivation is following the work presented in [32].

Optical Bloch equations are derived from the density matrix formalism, where decay terms can be easily added. The three-level atom density matrix is a  $3 \times 3$  matrix where diagonal terms represent the populations of atomic states, and off-diagonal terms represent the coherence between atomic states. As mentioned previously, two laser beams are included in the effect, where probe beam is much weaker than the control beam. Strong control beam optically pumps almost all population to the  $|1\rangle$  state so we can assume that  $\rho_{11} \approx 1$ , and  $\rho_{22} \approx \rho_{33} \approx 0$  and also  $\rho_{23} \approx 0$ . This approximation is called the weak probe approximation.

Using this approximation, and adding the relaxation terms to the differential equations, we obtain

$$\dot{\rho}_{13} = -i(\Delta_p - i\gamma_{13})\rho_{13} - i\Omega_c^*\rho_{12} - i\Omega_p^* \quad (5.1a)$$

$$\dot{\rho}_{12} = -i(\Delta_p - \Delta_c - i\gamma_{12})\rho_{12} - i\Omega_c\rho_{13}. \quad (5.1b)$$

Here we used Rabi frequencies of probe and control beams defined as  $\Omega_p = \mathbf{d}_{31} \cdot \boldsymbol{\epsilon}_p E_p / 2\hbar$  and  $\Omega_c = \mathbf{d}_{32} \cdot \boldsymbol{\epsilon}_c E_c / 2\hbar$ , where  $\mathbf{d}_{ij}$  are transition dipole moments,  $\boldsymbol{\epsilon}_{p/c}$  are electric field polarization vectors and  $E_{p/c}$  are electric field amplitudes.

The steady-state solution for  $\rho_{13}$  of the Eqs. (5.1a) is

$$\rho_{13} = \frac{\Omega_p^*(\Delta_p - \Delta_c - i\gamma_{12})}{|\Omega_c|^2 - (\Delta_p - \Delta_c - i\gamma_{12})(\Delta_p - i\Gamma_{13})}. \quad (5.2)$$

By equating the probe-induced dipole moment and the induced dipole moment terms, we obtain the expression for the probe-induced polarizability [32]:

$$\alpha_p = \frac{|\mu_{13}|^2}{\hbar} \frac{\Delta_p - \Delta_c + i\gamma_{12}}{|\Omega_c|^2 - (\Delta_p - \Delta_c + i\gamma_{12})(\Delta_p + i\Gamma_{13})}, \quad (5.3)$$

where  $\mu_{13} = \mathbf{d}_{13} \cdot \boldsymbol{\epsilon}_p^*$  is the projection of the transition dipole moment to the polarization vector axis.

The index of refraction detected by the probe laser is [69]:

$$n = \sqrt{1 + N\alpha_p / \epsilon_0}, \quad (5.4)$$

where  $N$  is the concentration of atoms. Assuming that the index of refraction is complex, the

imaginary part gives us the expression for the absorption coefficient

$$\alpha = \frac{N\omega_p}{\epsilon_0 c} \frac{|\mu_{13}|^2}{\hbar} \frac{\Gamma_{13}\delta^2 + \gamma_{12}(\gamma_{12}\Gamma_{13} + |\Omega_c|^2)}{[\Delta_p\delta - \gamma_{12}\Gamma_{13} - |\Omega_c|^2]^2 + [\gamma_{12}\Delta_p + \Gamma_{13}\delta]^2}, \quad (5.5)$$

and the expression for the real part of the refractive index

$$n_r = 1 - \frac{N}{2\epsilon_0} \frac{|\mu_{13}|^2}{\hbar} \frac{\delta(\delta\Delta_p - |\Omega_c|^2) + \gamma_{12}^2\Delta_p}{[\Delta_p\delta - \gamma_{12}\Gamma_{13} - |\Omega_c|^2]^2 + [\gamma_{12}\Delta_p + \Gamma_{13}\delta]^2}, \quad (5.6)$$

where  $\delta = \Delta_p - \Delta_c$  is the relative probe-control detuning, or the two-photon detuning. The probe absorption and the real part of the refractive index are presented in Fig. 5.2, where they are presented as a function of the probe detuning  $\Delta_p$  and control detuning is set to be zero  $\Delta_c = 0$ .

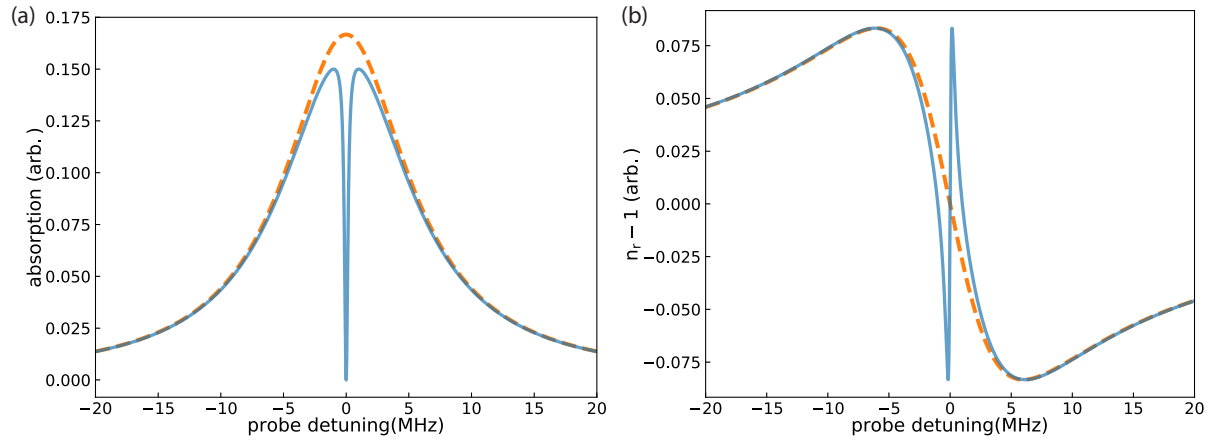


Figure 5.2: (a) Probe beam absorption and (b) the real part of the refractive index as functions of the probe beam detuning in the EIT conditions. They are presented with a blue solid line, whereas the orange dashed line presents probe absorption and the real part of the refractive index when the control beam is off. Parameters used:  $\Delta_c = 0$ ,  $\Omega_c = 1$  MHz,  $\Gamma_{13} = 6$  MHz,  $\gamma_{12} = 0$ .

The figures compares absorption of the probe beam and the real part of the refractive index in the EIT conditions (solid blue line), and in the conditions with no control beam (dashed orange line). In the EIT conditions when the probe beam and the control beam are in resonance with respective transitions, probe absorption drops to zero (if  $\gamma_{12} = 0$ ). As a result probe beam is completely transmitted through the medium, where in usual conditions it should be absorbed. In other words, the medium becomes transparent for the probe beam. In usual laboratory conditions, ground state decoherence is around a few kHz, and  $\Gamma_{13}$  is in the range from several MHz to several hundreds of MHz. As a consequence, the absorption coefficient is no longer 0 in the

EIT resonance and the probe beam is slightly absorbed by the medium.

This narrow window of the reduced absorption is called the EIT window. The EIT window is described with the Lorentzian lineshape, where its FWHM is defined as [32]

$$\Gamma_{EIT} = 2\gamma_{12} + \frac{2|\Omega_c|^2}{\Gamma_{13}}. \quad (5.7)$$

The EIT window is also characterized by its contrast, which is a measure of the amplitude of the transparency window defined as

$$C = |\Omega_c|^2 / (\Gamma_{13}\gamma_{12} + |\Omega_c|^2). \quad (5.8)$$

From this expression, we see that the ground state decoherence rate reduces the EIT window contrast, so the probe beam is more absorbed in the medium for a higher ground state decoherence rate.

In real experiments, the situation is more complex, since atoms have complex energy level structures. Off-resonant excitation of other states is possible which lowers the EIT linewidth and contrast. These effects are included in the EIT linewidth expression (5.7), by introducing the optical depth factor [70]. OD is the on-resonance optical depth of the probe field in a medium of length L. The Eq. (5.7) is then equal to:

$$\Gamma_{EIT} = 2\gamma_{12} + \frac{2|\Omega_c|^2}{\Gamma_{13}\sqrt{OD}}. \quad (5.9)$$

### 5.1.2 Slow light and quantum memories

It is known that light travels slower in a medium than in the vacuum. The group velocity of light with frequency  $\omega_p$  traveling through a medium with an index of refraction  $n_r$  is [30]:

$$v_g = \frac{c}{n_r + \omega_p \frac{\partial n_r}{\partial \omega_p}}. \quad (5.10)$$

As we saw in the previous section, the EIT effect changes the absorption profile of the probe beam, but it also changes the refraction index of the medium, as presented in Fig. 5.2(b). It is clear that the gradient of the index of refraction of the probe beam is very steep near the resonance. The gradient is positive, so it leads to the significant reduction of the group velocity of the probe beam in EIT conditions. This is the phenomenon called *slow light* [67]. Using the definition of the optical depth and the expression for the index of refraction Eq. (5.6), the group

velocity of the probe beam in the EIT conditions is equal to [32]

$$v_g = L \frac{\Gamma_{EIT}}{\sqrt{OD}}, \quad (5.11)$$

where  $L$  is the length of the medium.

Let us consider a pulsed probe beam with a pulse duration of  $\tau_p$ . The probe pulse traveling through the EIT medium is propagating slower in comparison to the reference probe beam propagating through free space so the time delay between these two pulses is  $\tau_d$ . The delay time of the probe pulse is due to the reduced group velocity inside the EIT medium, so the delay is defined as  $\tau_d = L/v_g - L/c$ . Using the expression Eq. (5.11) and the fact that  $v_g \ll c$  inside the EIT medium, delay time is equal to

$$\tau_d = \frac{\sqrt{OD}}{\Gamma_{EIT}}. \quad (5.12)$$

This means that if the EIT window is narrower, the delay of the probe pulse will be larger, and the group velocity will reduce.

The probe pulse in the EIT medium is also spatially compressed. The pulse length inside the EIT medium is [71]

$$L_p = \frac{L_0 v_g}{c}, \quad (5.13)$$

where  $L_0$  is the free space length of the probe pulse. To summarize, the probe pulse is slowed and compressed inside the EIT medium so, in other words, the pulse is stored inside the EIT medium.

Storage of the pulse inside the EIT medium has its limitations. For a pulse to be stored inside the EIT medium, its frequency bandwidth  $\tau_p^{-1}$  must be smaller than the EIT linewidth. If the pulse is too short, and its bandwidth is larger than the EIT linewidth, it will be partially absorbed by the medium, since only the frequency components inside the EIT linewidth are transmitted through the medium. Using the relation (5.12) this limit can be expressed as [32, 71]:

$$\tau_p^{-1} \tau_d \leq \sqrt{OD}. \quad (5.14)$$

Another limitation to efficient pulse storage inside the EIT medium is that the compressed pulse must be shorter than the length of the EIT medium. Combining these two limitations, it can be shown that the optical depth must be large for the efficient storage of pulses [71].

In this kind of storage, a pulse can only be slowed, but not stopped. To achieve storage

of light and its retrieval, the control beam must be changed, since it changes the bandwidth of the EIT. Intensity reduction of the control beam can reduce the probe beam group velocity to zero, so the pulse is stored inside the medium [71, 66]. Retrieval of the pulse stored inside the medium is done by switching on the control beam. The storage time is limited by the ground state decoherence.

## 5.2 Experimental setup

In the previous section, I have described the effect of the Electromagnetically induced transparency. EIT is an effect where a probe beam is transmitted through the EIT medium, while it is usually absorbed by the medium. In the experiment, we use  $^{85}\text{Rb}$  atoms at room temperature as our medium. There are two major transitions for  $^{85}\text{Rb}$ ,  $D_1$  and  $D_2$ , presented in Fig. 4.1. As is mentioned in the previous section, the existence of many different hyperfine transitions in the excited state is lowering the EIT linewidth and contrast. To obtain the best possible EIT signal, we are working with  $D_1$  transitions at 795 nm. The spacing of two excited states for  $D_1$  transition is 361.58 MHz, which is sub-optimal since one of the transitions lays under Doppler broadened line (around 500 MHz at room temperature) of another transition. This additional excited state is partially absorbing the control and probe beam, so the EIT conditions are not ideal. The control beam is tuned to the  $|F = 3\rangle \rightarrow |F' = 3\rangle$  transition, and the probe beam is tuned to the  $|F = 2\rangle \rightarrow |F' = 3\rangle$  transition.

In the experiment, we are using a Toptica DL100 ECDL laser, with a single-mode laser diode QLD-795-150S from QPhotonics. The output laser beam was diverging in a horizontal direction so we setup the cylindrical telescope to shape the laser output beam. We used a Faraday isolator to prevent unwanted back-reflection to the laser diode. The laser diode is stabilized using saturation spectroscopy and modulation of the magnetic field around the reference Rb cell. The signal of the saturation spectroscopy, with identified transitions, is presented in Fig. 5.3. Laser is stabilized to the crossover peak arising from  $|F = 3\rangle \rightarrow |F' = 2\rangle$  and  $|F = 3\rangle \rightarrow |F' = 3\rangle$  transitions. The laser linewidth is around 700 kHz, measured with heterodyne beat spectroscopy using the stabilized Menlo FC1500-250-ULN frequency comb.

The stabilized output of the laser is separated into two beams necessary for EIT demonstration, and their setup is presented in Fig. 5.4. The control beam and the probe beam are derived from the same laser source and so they are mutually phase-coherent. It is possible to use two separate cw lasers, but they have to be phase-locked, which is more complex and prone to increased instability in the system. The control beam uses the majority of the power from the main laser beam. To frequency tune the control beam, we use a double-pass AOM setup, which

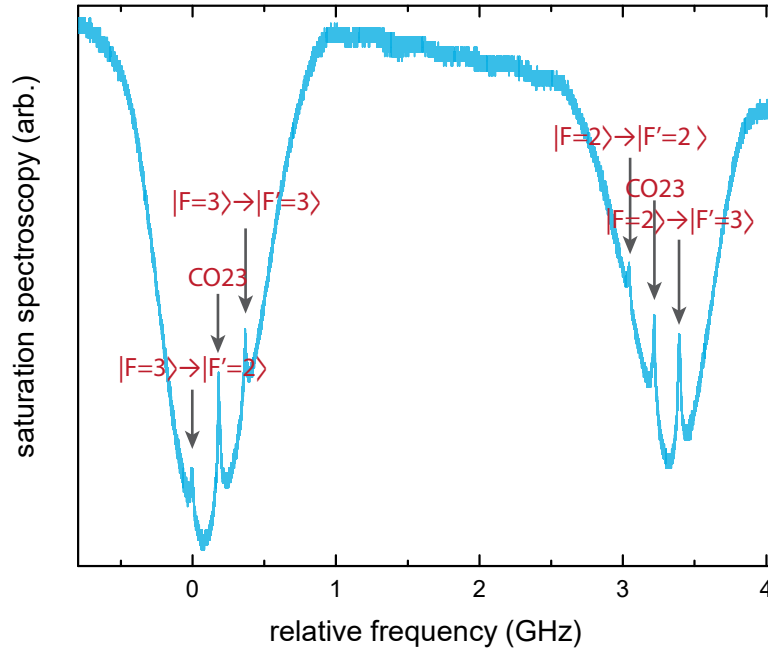


Figure 5.3: Saturation spectroscopy signal for  $^{85}\text{Rb}$   $D_1$  transition. Labeled peaks represent atomic transitions and crossover signals.

we also use to switch off the control beam. Using the AOM, control beam frequency is resonant with  $|F = 3\rangle \rightarrow |F' = 3\rangle$ .

Preparation of the probe beam is more complex since it requires larger frequency tuning. Tuning of the probe beam frequency starts by coupling the beam into the fiber-coupled EOM PM785 from Jenoptik. The electro-optic modulator (EOM) is a device that uses high-frequency phase modulation to create sidebands around the carrier frequency. EOM generates sidebands at frequencies  $\omega \pm \Omega$ , where  $\omega$  is the carrier frequency, and the  $\Omega$  is the phase modulation frequency. At higher modulation depth, sidebands of higher orders are not negligible. In the experiment, we want to shift the probe beam for exactly 3035.732439 MHz, which is the frequency of the hyperfine splitting of the  $^{85}\text{Rb}$  ground state [38]. To get as much as possible laser power, we choose a relatively high modulation depth so the  $\pm 1$  sidebands are of higher amplitude in comparison to the carrier amplitude, in other words, a relatively high modulation depth is required. For this, we use a Rigol DSG836 frequency generator and high-frequency amplifier ZHL-42+ from Mini-Circuits.

The output from the EOM has now a probe beam, together with another four frequencies. Most of the frequencies do not interact with Rb atoms, since they are far detuned, but are an inconvenience for the signal detection after the Rb cell. To filter the unwanted frequencies from the probe beam, we built an optical cavity that can transmit only one of these frequencies,

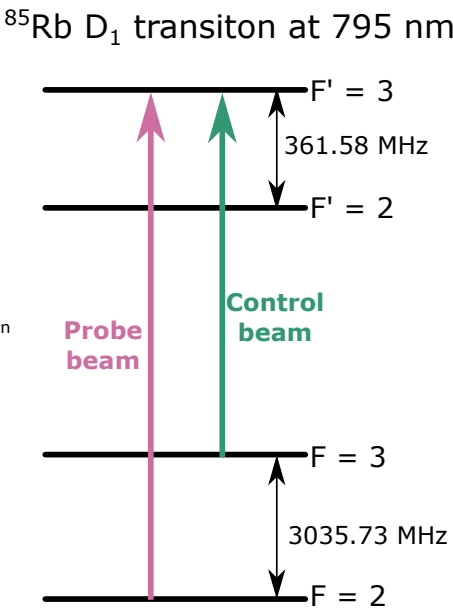


Figure 5.4: Schematic setup for EIT and QM experiment and schematic energy level diagram with labeled laser beams. The probe beam and the control beam paths are presented, as well as the filtering cavity, and the vapor cell within mu-metal shield. Abbreviations used in figure: M - mirror, L - lens, PD - photodiode, APD - avalanche photodiode, ND - neutral density filter, BS - beamsplitter, PBS - polarizing beam splitter, FI - Faraday isolator, AOM - acousto-optics modulator,  $\lambda/2$  - half-waveplate,  $\lambda/4$  - quarter-waveplate, FC - fiber coupler, CYL - cylindrical lens, EOM - electro-optics modulator, ASPH - aspherical lens, CAVITY - optical cavity.

depending on the system parameters. More details about the optical cavity are in the next section. Fine-tuning of the probe beam frequency is achieved with a double-pass AOM setup, which can also precisely switch the probe beam. The probe beam is tuned in resonance with the  $|F = 2\rangle \rightarrow |F' = 3\rangle$  transition.

After fine-tuning of control and probe beams, they are also expanded with two separate telescopes, where the  $1/e^2$  diameter of the control beam is 15.5 mm and the  $1/e^2$  diameter of the probe beam is 5.6 mm. The control and the probe beam are merged on the PBS, and their polarizations are perpendicular linear. Co-propagation of the control and the probe beam is crucial in the EIT experiments due to the residual Doppler broadening [32], where an angle of

only a few mrad between two beams is broadening EIT linewidth for hundreds of kHz. The co-propagation of the control and probe beams is ensured by dummy coupling both of the beams into the single-mode fiber. First, we insert the probe beam into the SM fiber. Using the second set of mirrors, we align the control beam to be coupled in the same fiber simultaneously. Since coupling into the fiber is very sensitive to any miss-alignment this is ensuring that the control and the probe beams are co-propagated to the best of our abilities.

Co-propagated beams are going through a Rb vapor cell inside the mu-metal shield, and after that using a Glan-Thompson polarizer, the probe beam is transmitted and focused to the avalanche photodiode APD430A/M from Thorlabs. Mu-metal shield is a nickel-iron soft magnetic alloy of very high magnetic permeability, which serves as a shield for stray magnetic fields. We have bought a triple-layered mu-metal shield from Meca-Magnetic, for our custom order. Shield is cylindrical shape made from a sheet material 1 mm thick, and dimensions of layers are  $d_1 = 290$  mm,  $L_1 = 300$  mm,  $d_2 = 270$  mm,  $L_2 = 280$  mm and  $d_3 = 250$  mm,  $L_3 = 260$  mm. Each of the layers has end caps that can be removed. Magnetic shielding is important since the magnetic field is broadening the atomic transitions due to the Zeeman effect, and consequentially is the EIT linewidth broadens. A photograph of the experimental setup is presented in Fig. 5.5.

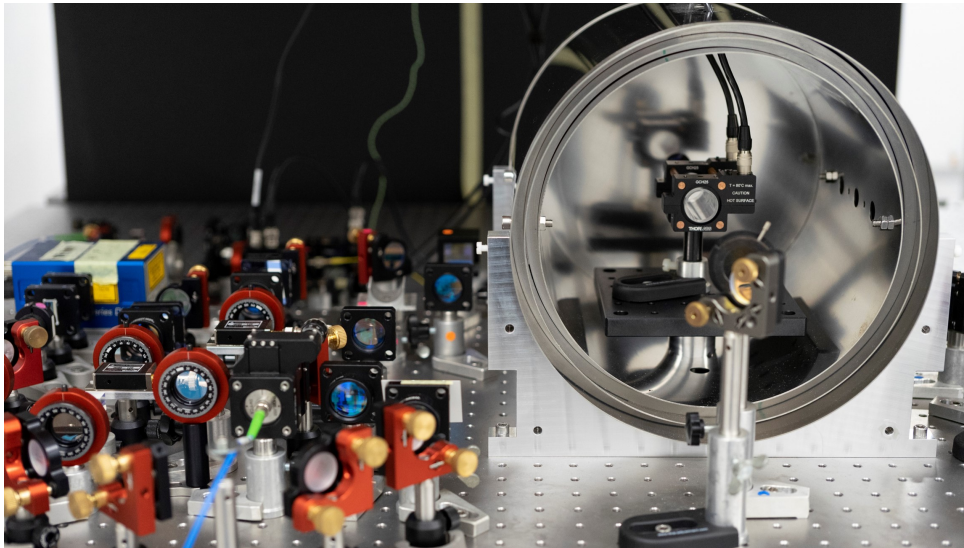


Figure 5.5: Photograph of the experimental setup for EIT and QM. On the right side is the glass cell inside the mu-metal shield with opened end caps. Photograph by H. Hiršl.

### 5.2.1 Filtering cavity

We have built a custom optical cavity which is used as a filtering cavity of the output from the EOM. For the modulation depth of the EOM, the output beam consists of five frequencies, with frequencies of  $\omega$ ,  $\omega \pm \Omega$ , and  $\omega \pm 2\Omega$ . The EIT probe beam is the +1 sideband of the EOM output, so other frequencies should be discarded.

An optical cavity is built from two concave mirrors, Layertec 103239, with a radius of curvature of 50 mm. The reflectivity of the mirrors is 0.991, which gives a finesse of around 350. Mirrors are glued to the Inox 304 spacer, where a piezoelectric actuator is glued between one mirror and the spacer so we can scan the modes of the cavity and lock the cavity. Piezo actuator is HPCh-150/15-8/3 from Piezomechanik.

After the cavity was assembled, the measured free spectral range of the cavity is  $FSR = 8.9$  GHz, which corresponds to the spacing between mirrors of 1.7 cm. From the mirrors finesse and FSR, we estimate the linewidth of the cavity modes to be around 25 MHz. Transmission from the cavity is measured to be around 40%. A photograph of the assembled cavity on a separate breadboard is presented in Fig. 5.6.

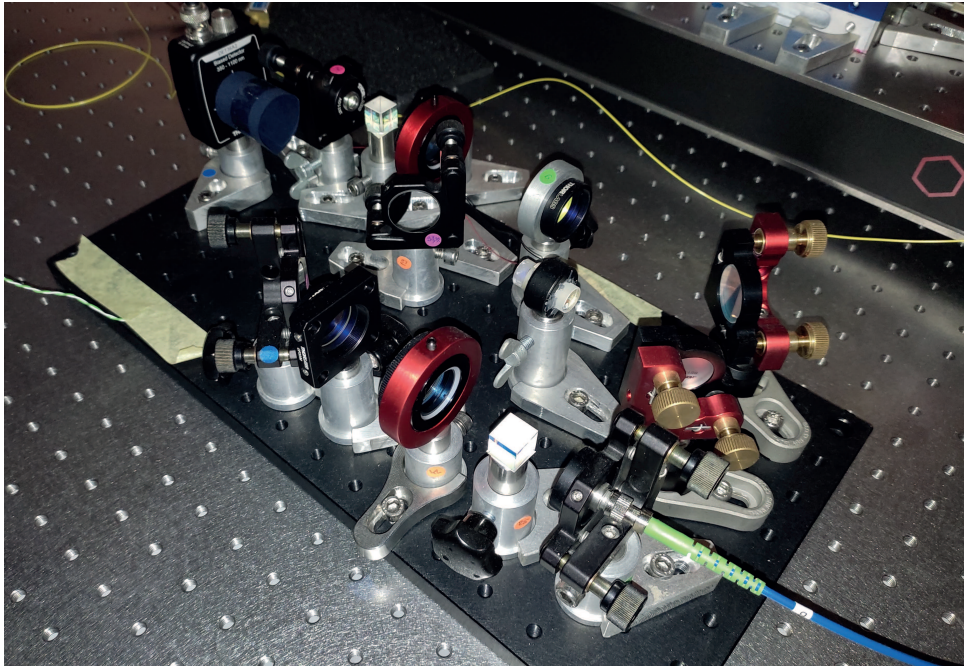


Figure 5.6: Photograph of the setup for filtering cavity.

The cavity transmission signal is obtained using a photodiode which detects a small portion of the cavity transmission through a lossy mirror. The cavity is stabilized using a side-of-resonance method [72]. In this method, the side of the Lorentzian lineshape of cavity modes is

serving as a discriminant signal for the stabilization of the cavity. The principle of this cavity locking is presented in Fig. 5.7. The cavity is locked using a Servo PI controller NewFocus LB1005.

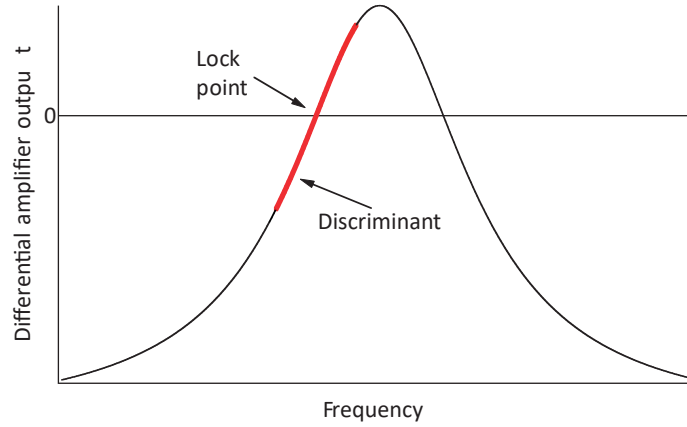


Figure 5.7: Side of resonance cavity locking principle. The side of the cavity resonance (red line) serves as a discriminant for cavity stabilization. Adapted from [72].

Cavity transmission signal is presented in Fig. 5.8, when EOM is switched on. In the usual conditions, modulation depth is chosen so the  $\pm 1$  sidebands have maximum amplitude. In the middle of the scan, there is the carrier frequency, the  $n$ -th cavity mode. In the scan there are also visible  $\pm 2$  sidebands from the  $(n \mp 1)$ -st cavity modes due to the small FSR of the cavity. When the cavity is stabilized to the  $+1$  sideband of the EOM, this beam is a resonant probe beam for the experiment. Other frequencies are filtered from the beam and have no measurable effect on the results.

In the experiment, the  $-1$  sideband is also used. When the cavity is locked to the  $-1$  sideband, the probe beam is far off-resonant and is used as a reference beam for the EIT and QM measurements, since it is passing through the same optics as is the resonant probe beam, so all losses on the optics are included in the measurements.

### 5.2.2 Rubidium glass cells

In the experiment, we use four different vapor cells filled with  $^{85}\text{Rb}$  atoms. One vapor cell is without any coating or filling, with diameter of 25 mm and length of 50 mm. Diameters of other three vapor cells are 25 mm, and they are 75 mm long. Each of these three cells has a different coating or filling, which reduces the ground state decoherence, and thus the storage time of the quantum memory.

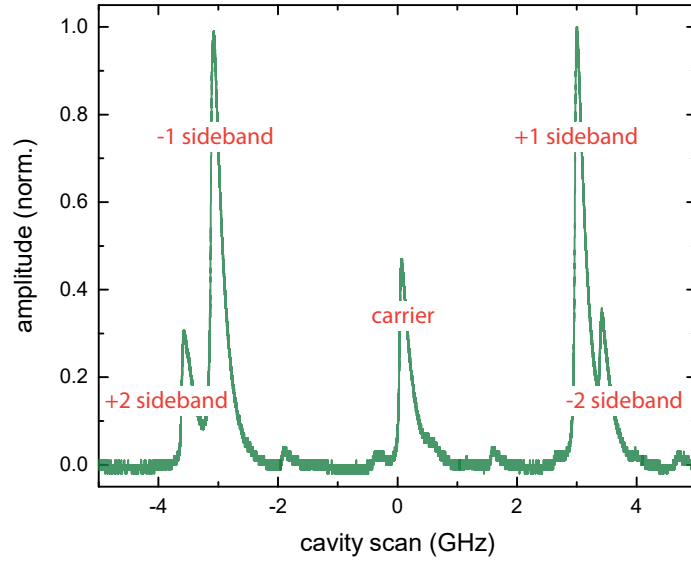


Figure 5.8: Cavity transmission signal when EOM is switched on. Due to the high modulation depth,  $\pm 1$  sidebands have the largest amplitude.  $\pm 2$  sidebands are a consequence of small FSR and they are sidebands from previous and later cavity modes.

The first coated vapor cell is a quartz cell with a paraffin coating. This cell has windows wedged at 1 degree, and an AR coating for 795 nm on both sides of the windows. The second coated cell is also a quartz cell with an alkene coating. Windows are also AR coated and 1 degree wedged. The last coated vapor cell is a quartz cell with paraffin coating and filled with 5 Torr of neon gas. This cell has flat windows and no AR coating. Vapor cells are produced on demand by Precision Glassblowing.

From the measurements, we have noticed that the cells with an AR coating are mixing the polarizations of the probe and control beam slightly. The coating on the glass cell has the purpose of the reduction of the ground state decoherence. Best EIT linewidths and contrasts are achieved for the cell with minimal ground state decoherence. In the experiment, we are measuring the ground state decoherence of these three cells and we study how the decoherence affects the quantum memory efficiency and storage time.

The EIT width is a combined effect of several mechanisms in the experiment. We have already mentioned some of them, residual Doppler broadening and the presence of the magnetic field. Residual Doppler broadening is the effect when the probe and the control beams are not perfectly co-propagated. Due to the difference in beams wavevector, two-photon detuning is slightly shifted, which results in broadening of EIT [73]. Presence of the magnetic field splits degenerate Zeeman components of the hyperfine levels which are then broadened. There are many other mechanisms, where some of which are transit-time broadening, Rb-Rb collisions,

and collisions with walls. The effects of these mechanisms are discussed in detail in [74]. Briefly, the transit-time broadening is a consequence of the atomic motion in the vapor cell, where atoms leave the volume of the cell illuminated with the probe and control beam, and other atoms (atoms not in a prepared EIT state) arrive in the illuminated cell volume. Rb-Rb collisions have a small effect when the medium is dilute but are significant at higher temperatures. By the term Rb-Rb collisions, we refer to the Rb-Rb hyperfine changing collision, where Rb atoms colliding can exchange their hyperfine states, due to the valence electron exchange process. The last mentioned effect is one of the biggest effects that is impairing the EIT resonance, the collisions of Rb atoms with glass cell walls. After this kind of collision, Rb atoms lose their *memory*, i.e. their coherence is lost after a collision with the vapor cell wall.

Effects that increase the ground state decoherence rate are approached in two different ways. As we mentioned, collisions with glass cells are the biggest source of the decoherence, so the first method of the reduction of the decoherence from these collisions is the usage of anti-relaxation coatings on the walls of the glass cell. When atoms collide with a coated wall, their coherence is preserved in that collision. Coatings usually allow up to several thousand collisions with walls before atomic coherence is lost. In the experiment, we use two different types of glass cell coatings, paraffin coating, and alkene coating. While there are lot of experimental data on the EIT and QM experiments with glass cells coated with paraffin coating [75, 76], literature about the novel alkene coating is limited [77].

Another method of the reduction of the ground state decoherence is by filing the glass cell with an inert gas. In usual experimental conditions pressure of the inert gas is several orders of magnitude higher than the Rb vapor pressure, so the Rb atoms are moving diffusely, where its mean free path is greatly reduced. This means that atoms are staying inside the illuminated region of the glass cell for longer times and their coherence is preserved [64, 32].

In the experiment, we will measure the ground state decoherence rate of these three glass cells, and study their effect on the QM efficiency and storage time.

### 5.2.3 Glass cell heater

The EIT and QM measurements are done at room temperature and elevated temperature, so the atomic concentration is increased in the glass cell, and consequentially the optical depth. In the experiment, we used a GCH25-75 glass cell heater from Thorlabs. This glass cell heater produces a small, but noticeable magnetic field, which broadened our EIT resonance significantly. By changing all possible Inox parts of the heater, we reduced the magnetic field, but not sufficiently. Because of the stray magnetic field, this glass cell heater was not suitable for our experiment, since the decoherence rate is smaller than the magnetic field broadening induced

by the heater.

To raise the temperature above the room temperature, we have built a glass cell heater without magnetic components, using only paramagnetic and diamagnetic materials. The render of the glass cell heater and the photograph of the heater inside the mu-metal shield is presented in Fig. 5.9.

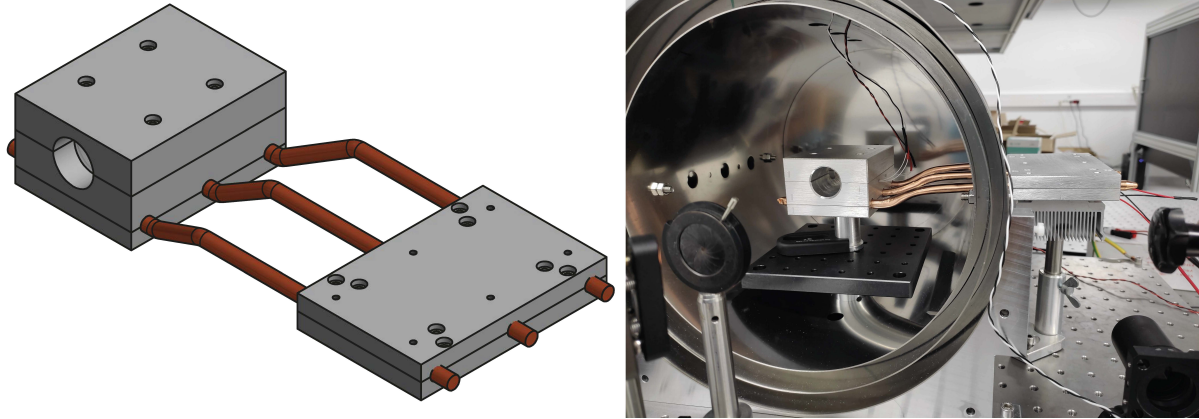


Figure 5.9: Home-built glass cell heater without magnetic parts. Glass cell heater is constructed of two units, the outside unit that is heated with two Peltier elements, and the inside unit, where the glass cell is placed. Transfer of the heat from the outside unit to the inside unit is achieved with three copper heat pipes. Temperature is stabilized using a temperature PID controller.

The heater is constructed using two aluminum blocks, connected with copper heat pipes. The outside unit is heated using two Peltier modules. Heatpipes are very efficient guides of the heat, and heat is transferred from the outside unit to the inside unit. Glass cell is placed in the inside aluminum block, where the top part of the block is easily removed so the glass cells can be changed. To increase the performance of the heater, we use additional heat tape glued to the outside aluminum block.

Temperature is measured using several thermistors, where thermistors placed inside the mu-metal are built from non-magnetic materials. The temperature of the inside unit is stabilized using a Wavelength electronics MPT2500 temperature controller. Temperatures of the inside and outside units, and the set and actual temperature for the temperature controller are monitored using a LabJack T7 data acquisition card, and the InfluxDB database. Details about the database can be found in [78].

### 5.3 Measurement of the ground state decoherence

EIT resonances are measured by fixing the frequency of the control beam on resonance with the  $|F = 3\rangle \rightarrow |F' = 3\rangle$  transition. The probe beam is scanned around the resonance of the  $|F = 2\rangle \rightarrow |F' = 3\rangle$  transition, so the two-photon detuning is  $\delta = 0$  when the probe beam is resonant with the respective transition, and the EIT condition is satisfied. The control and the probe beam are fine-tuned using AOMs operated by the MogLabs XRF RF synthesizer. This device and the timing sequence of the experiment are controlled using Python code and the manufacturer's software. The start of the measurement is triggered using a Syncray digital pulse generator, which is also used to trigger the oscilloscope to obtain the EIT scan trace.

EIT signal is obtained by taking the probe transmission trace on the Teledyne LeCroy WaveSurfer 4104HD oscilloscope. EIT signal is calculated from three transmission measurements, the measurement of the EIT transmission signal, locking the probe beam to the +1 sideband of the filtering cavity, the measurement of the reference beam, locking the probe beam to the -1 sideband, and a background measurement when the probe beam is switched off. Background measurement is required due to the small leak of the control beam through the polarizer. Each of these traces is recorded 30 times, and then averaged to increase the signal-to-noise ratio. Averaged examples of recorded traces are presented in Fig. 5.10(a).

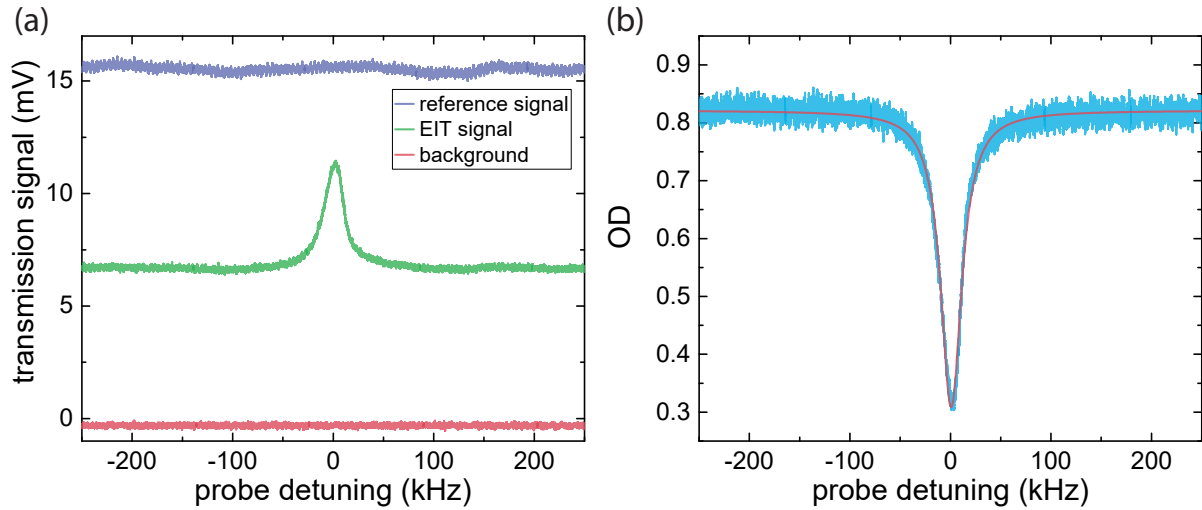


Figure 5.10: (a) An example of transmission signals for the calculation of (b) the EIT absorption signal. EIT absorption signal is calculated using the Beer-Lambert law. The red line is marks the Lorentzian fit.

To calculate the EIT absorption spectrum from transmission signals, we use the Beer-

Lambert law:

$$kL = \ln \left[ \frac{I_{reference} - I_{background}}{I_{signal} - I_{background}} \right], \quad (5.15)$$

where  $k$  is the absorption coefficient and  $L$  is the length of the cell. The product  $kL$  is often called the optical depth (OD) of the medium. The calculated EIT absorption spectrum from transmission signals is presented in Fig. 5.10(b) as well as the Lorentzian fit to the data. From the figure, we calculate two parameters, EIT linewidth and EIT contrast. The linewidth of the EIT signal from the figure is around  $2\pi \cdot 25$  kHz and the contrast is around 62 %. Due to the laser stabilization method, it is challenging to exactly fine-tune the frequency of the control beams in resonance with the respective transition. The EIT signal is a little skewed due to the small detuning of the control beam from the atomic transmission, so we developed a Python code to calculate the EIT linewidth as the FWHM of the EIT signal and the contrast from signals. Details about the code can be found in [79].

First, we investigated the EIT phenomenon in the cell without coating. This is required to understand the effects of the coatings and filling in other cells on the ground state decoherence. In the cell without coating, the dominant effect of the ground state decoherence is the transient-time broadening. EIT linewidth is broadened due to the atom moving through finite size beams [80]. When atoms leave beams they collide with the cell walls, they lose their ground state coherence. Another effect that is broadening the EIT resonance is residual Doppler broadening, due to the difference in probe beam and control beams wavevectors.

Measured EIT width does not change by varying the pump beam intensity, as it is given by the transit-time broadening. The measured ground state decoherence for the cell without coating is  $2\pi \cdot (121 \pm 7)$  kHz. To eliminate the effects of the residual Doppler broadening, we measured the EIT width as a function of the control beam angle, as presented in Fig. 5.11. Power of the probe beam is  $2.5 \mu\text{W}$ , and the intensity is  $20 \mu\text{W}/\text{cm}^2$ . For each angle of the control beam, we measured EIT width as a function of control beam power in the range 2 – 17 mW. By fitting the Eq. (5.7) to data, we plotted  $2\gamma_{12}$  as a function of the control beam angle. As is expected, the change of the angle of the control beam increases the ground state decoherence rate, and thus the EIT width. The intersection of two lines in the figure marks the control beam angle that minimizes the residual Doppler broadening and it is equal to  $2\pi \cdot (249 \pm 2)$  kHz, so the minimum ground state decoherence is  $2\pi \cdot (125 \pm 1)$  kHz. It is important to mention that for this hyperfine EIT scheme residual Doppler broadening contribution to the ground state decoherence for  $^{85}\text{Rb}$  is at least  $\gamma_{12} = v_{th}|\mathbf{k}_c - \mathbf{k}_p| = 2\pi \cdot 1.7$  kHz [32], due to the difference in the magnitude of wavevectors of the probe and the control beam (two wavevectors correspond to different

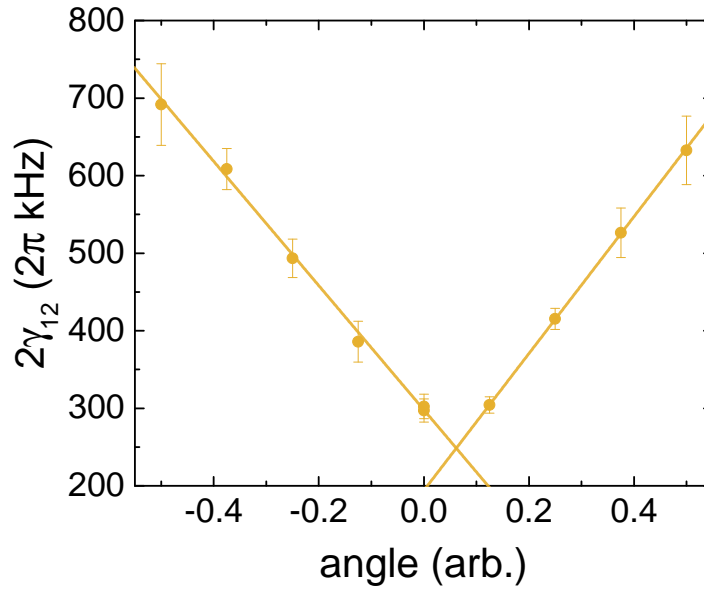


Figure 5.11: Ground state decoherence rate as function of the angle between the probe and the control beam. Crossing of lines marks the minimum intercept, where residual Doppler broadening effect is minimal.

hyperfine transitions with slightly different transition frequencies). Here  $v_{th} = \sqrt{k_B T / m}$  is the 1D RMS velocity of the atoms in the cell ( $T$  is the temperature and  $m$  is the mass of the atom) and  $\mathbf{k}_{c(p)}$  is the control (probe) beam wavevector.

Since all other broadening mechanisms are either eliminated (residual Doppler broadening, broadening due to the magnetic fields) or are negligible (ground state decoherence rate for Rb-Rb collisions is  $\gamma_{12} = 2\pi \cdot 0.8$  Hz at 295 K [81]), we conclude that in the cell without coating the major broadening mechanism is transit-time broadening. Another evidence that the transit-time broadening mechanism is dominant is the cusp lineshape of the EIT resonance [80]. An example of the EIT lineshape from in cell with no coating is presented in Fig. 5.12.

The purpose of the glass cell coating is to preserve the ground state coherence when the atom collides with walls. After the collision, the atom is again inside the laser beams, and the interaction time with lasers is extended, i.e. transit-time is increased, and transit-time broadening is reduced. Another way of increasing the transit-time of the atoms is by filling the vapor cell with an inert gas. Due to the collisions with inert gas, the mean free path of atoms is reduced, and transit-time is increased. In this work, we compare different coatings and fillings, and their effect on the ground state decoherence. In Fig. 5.12 we present the EIT resonances for three different vapor cells, a cell without coating, a cell with paraffin coating and cell with

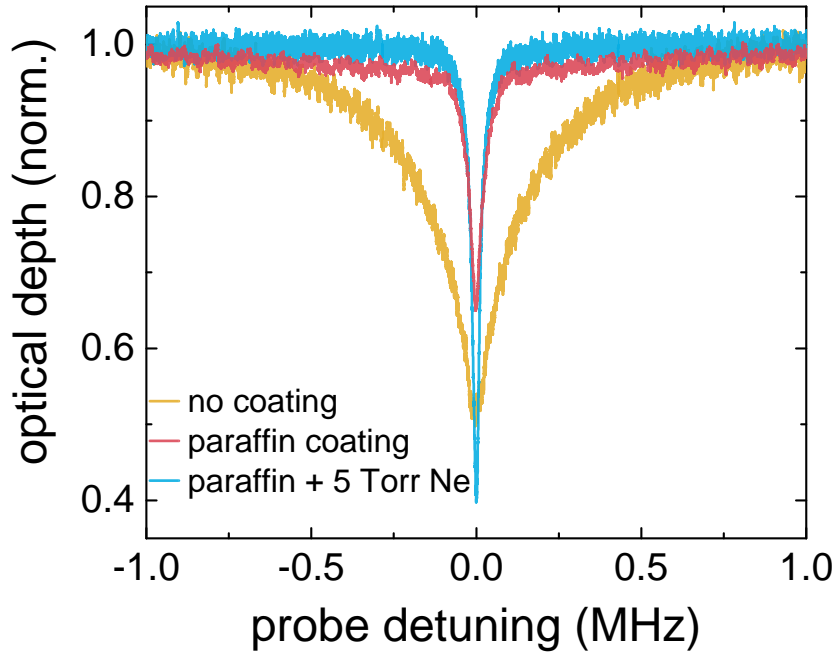


Figure 5.12: EIT lineshapes for the uncoated cell (orange), cell with paraffin coating (red) and cell with paraffin coating filled with 5 Torr of Ne (blue). Power of the probe beam is  $2.5 \mu\text{W}$ , and the power of the control beam is 5 mW for all three cells.

paraffin coating, and 5 Torr of Neon gas. There is a great difference in EIT width in cells without coating and cells with coatings and fillings. Experimental conditions were the same for these measurements, the power of the probe beam is  $2.5 \mu\text{W}$  and the power of the control beam is 5 mW. EIT width is reduced as a result of the ground state decoherence reduction for cells with coatings and fillings.

We characterized the ground state decoherence for three vapor cells with different coatings and fillings. Between measurements, we only replaced vapor cells so beam geometry remains the same, and thus the residual Doppler broadening minimal. We measured EIT width as a function of the power, i.e. the intensity of the control beam. The power of the probe beam was  $2.5 \mu\text{W}$ , i.e. the intensity was  $20 \mu\text{W}/\text{cm}^2$ . Results of the measurements are presented in Fig. 5.13.

For all three glass cells, the EIT linewidth increases linearly with the control beam intensity, as is expected from the theory. By fitting the Eq. (5.7) to the measured data we retrieved the ground state decoherence for all three glass cells. Ground state decoherence for glass cell with paraffin coating is  $\gamma_{12} = 2\pi \cdot (16.0 \pm 0.4) \text{ kHz}$ , and for the alkene coated cell  $\gamma_{12} =$

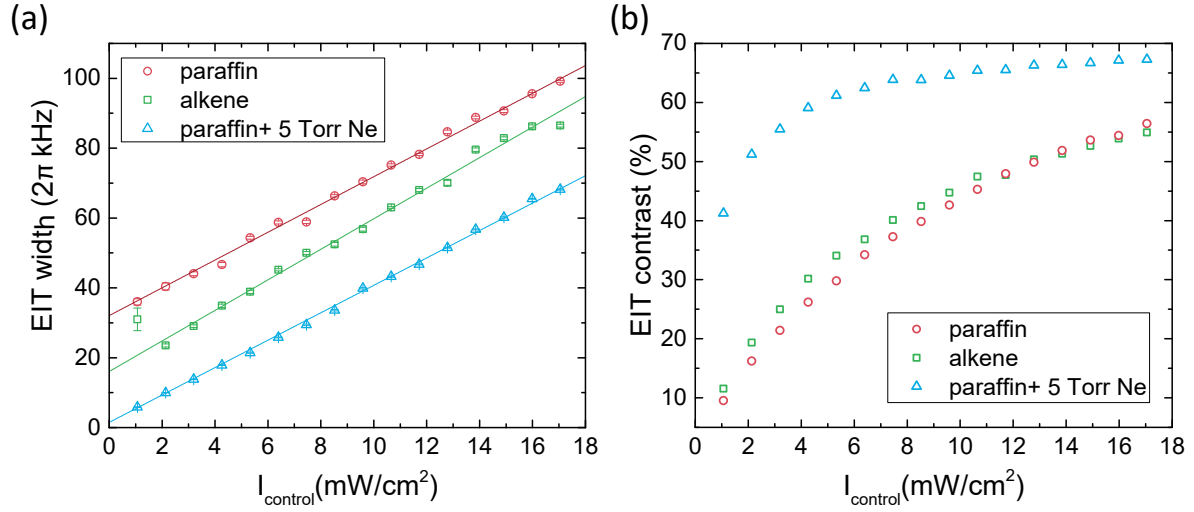


Figure 5.13: (a) EIT linewidth and (b) contrast as functions of control beam intensity. From the linear fit of the EIT linewidth to the Eq. (5.7), the ground state decoherence is calculated. Ground state decoherence for paraffin coated cell (red circles) is  $2\pi \cdot (16.0 \pm 0.4)$  kHz, for alkene coated cell (green squares) is  $2\pi \cdot (8.0 \pm 0.5)$  kHz, and for paraffin coated cell with 5 Torr of Ne (blue triangles) is  $2\pi \cdot (0.74 \pm 0.08)$  kHz. Error bars are shown in the figure but are typically smaller than the symbols.

$2\pi \cdot (8.0 \pm 0.5)$  kHz. Our measurements are in line with data in the literature, where alkene coating is expected to perform better than the paraffin coating [66, 22]. This means that the alkene coating is preserving the ground state coherence better than the paraffin coating when atoms are collide with the cell walls. The smallest ground state decoherence is measured for the cell with paraffin coating and filled with 5 Torr of neon,  $\gamma_{12} = 2\pi \cdot (0.74 \pm 0.08)$  kHz.

In the right panel of Fig. 5.13 we present the EIT contrast measurement as a function of control beam intensity. The highest contrast is achieved for the cell with paraffin coating and filled with 5 Torr of neon buffer gas, as is expected from the definition of the EIT contrast. For the other two cells, the EIT contrast is significantly smaller due to the higher ground state decoherence rate. From the figure, we can see that the maximum EIT contrast is close to 70 %. This means that the probe beam is still partially absorbed by the medium, despite being in the EIT state. This is due to the Rb level structure, where there is an additional excited state within the Doppler broadened profile, which absorbs a portion of the probe and control beam.

Comparing these results and the results for the cell without coating, a major reduction of the ground state decoherence is clearly evident. Still, it is important to understand what are the limitations of the coatings and fillings. To check the residual Doppler broadening we measured the EIT width for the cell with paraffin coating and 5 Torr of Ne buffer gas as a function of the control beam angle, see Fig. 5.14. Comparing this figure with Fig. 5.11 we see that

the  $2\gamma_{12}$  is a quadratic function of the angle between the control and the probe beam. This is a signature of the well-known EIT phenomenon in vapor cells with buffer gas called Dicke narrowing [73]. In the Dicke narrowing regime, due to the collisions with inert gas the system is no longer sensitive to residual Doppler broadening for small angles between the control and the probe beam, as well as increased transit-time of atoms. It is clear from the measurement that we have managed to minimize the residual Doppler broadening.

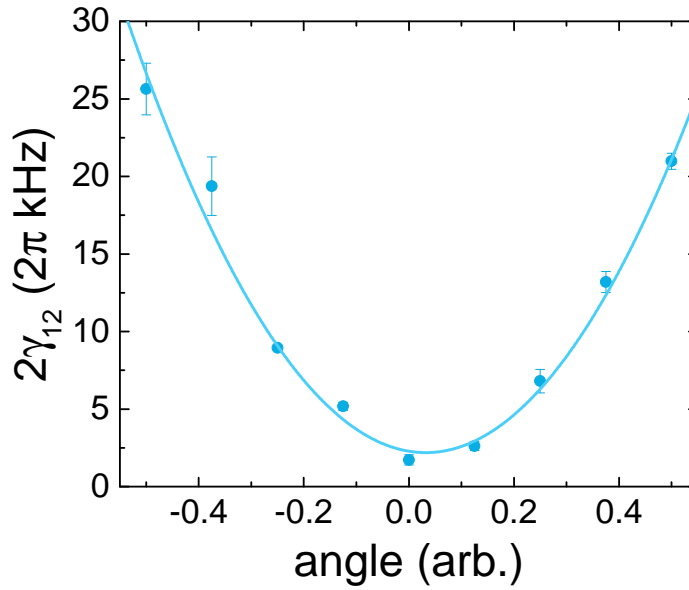


Figure 5.14: Ground state decoherence rate as function of the angle between the probe and the control beam for the cell with the paraffin coating and 5 Torr Ne buffer gas. Parabola minimum marks the minimum  $\gamma_{12}$ , where residual Doppler broadening effect is minimal. Minimum measured ground state decoherence rate is  $\gamma_{12} = 2\pi \cdot (0.9 \pm 0.2)$  kHz, while minimum from the fit is  $\gamma_{12} = 2\pi \cdot (1.1 \pm 0.2)$  kHz, which agrees well with measurement presented in Fig. 5.13.

From these measurements, we can now determine major contributions to the ground state decoherence. For the cells with the paraffin coating and the alkene coating, we have minimized residual Doppler broadening by ensuring that the probe beam and the control beam are overlapped. This is verified by measurements of the dependence of the EIT linewidth on the control beam angle, Figs. 5.11 and 5.14, where in between measurements beam geometry is not changed. For the hyperfine level scheme, we calculated that the minimum contribution of the residual Doppler broadening is  $2\pi \cdot 1.7$  kHz. Since all other contributions are eliminated or are negligible, we can conclude that the major contribution to the ground state decoherence is transit-time broadening. For the cell with paraffin coating and 5 Torr of Ne buffer gas, the conclusion is not straightforward. Since Rb atoms are moving diffusely through the buffer gas, con-

tributions of the broadening mechanisms are different than for the vapor cells without buffer gas. Predicted contribution of the residual Doppler broadening is  $\gamma_{RD} = 2D|\mathbf{k}_c - \mathbf{k}_p| = 2\pi \cdot 0.65$  kHz and the transit-time broadening contribution is  $\gamma_{TT} = 2D/w_0^2 = 2\pi \cdot 0.14$  kHz [80]. In these predictions  $D = 32$  cm<sup>2</sup>/s is the diffusion constant for Rb atoms in 5 Torr of Ne buffer gas,  $\mathbf{v}_{c(p)}$  is the wavevector of control (probe) beam and  $w_0 = 2.75$  mm is  $1/e^2$  radius of probe beam. These predictions are in line with our measurement, Fig. 5.13, of the ground state decoherence for the vapor cell with paraffin coating and 5 Torr of Ne buffer gas. Therefore, in this cell, we are limited by the combined effect of the residual Doppler broadening and the transit-time broadening.

## 5.4 QM storage time and efficiency

In quantum memories, the probe pulse is stored inside the EIT medium for a time  $t_{storage}$ , before it is released from the medium by switching on the control beam. To achieve that, the probe and the control beams have to be in the EIT condition, i.e. two-photon detuning must be zero.

The XRF device which we use to drive the AOMs is capable to store the timing sequence for the two beams (two XRF channels) into the device buffer. Two channels can run separately or they can be synchronized. To use a very precise timing sequence, where the sequence can change in 16 ns intervals, only one parameter in the sequence can change. In the experiment, we shape our sequence by changing the power output of the XRF to the AOMs, which then are changing the power of the beams or switching beams rapidly. The timing sequence is controlled with Python code and the manufacturer's program.

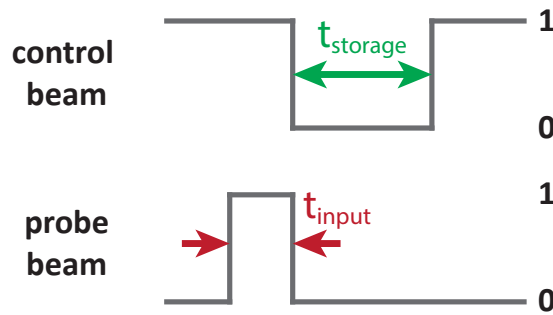


Figure 5.15: Measurement protocol of the quantum memories experiment. The control beam is switched on at the beginning. At some time probe beam pulse of duration  $t_{input}$  is switched on. At the time when the probe pulse is over, the control beam is also switched off. This is the writing stage of quantum memory. Both beams are switched off for time  $t_{storage}$ , after which the control beam is switched on, and the information stored in the medium is released in the form of a light pulse.

The experimental sequence is presented in Fig. 5.15. The experiment begins with the control beam switched on. This beam prepares the medium for the probe beam of duration  $t_{input}$ . At the time the probe beam pulse is over, the control beam is switched off, and the information is stored inside the medium. The control beam is switched off for the time  $t_{storage}$ . After storage time, the control beam is switched on to release information stored inside the medium. Released information, i.e. output from the medium, is a light pulse of the probe beam frequency. QM traces are averaged 1000 times with a built-in function of the oscilloscope to improve the signal-to-noise ratio. An example of the input pulse and output pulse is presented in Fig. 5.16

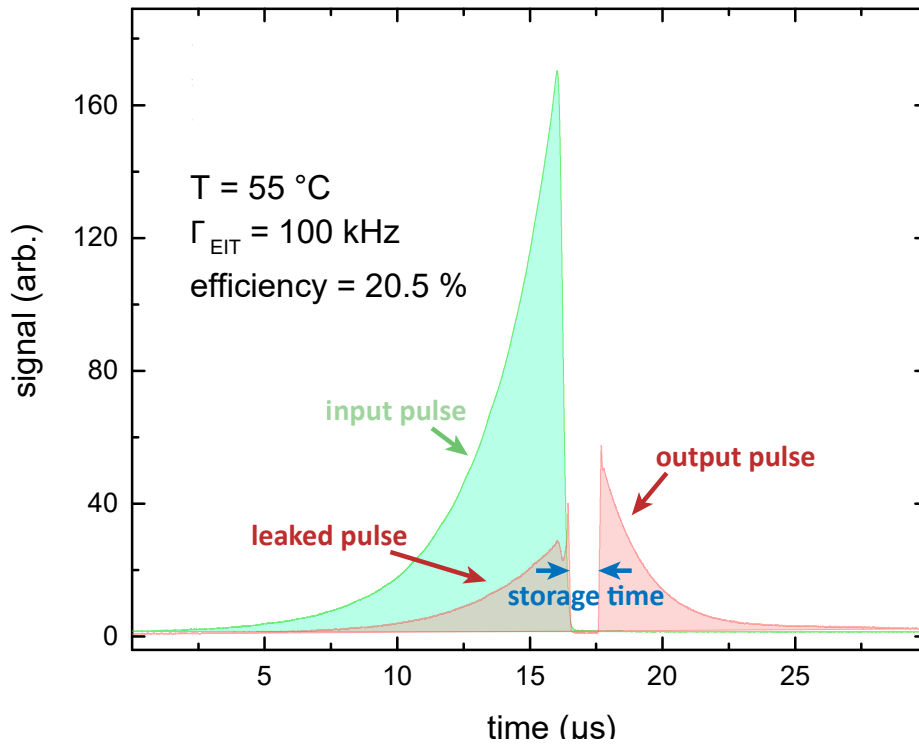


Figure 5.16: An example of the signals in QM experiment. Input probe pulse is presented in green color. Pink color presents the output pulse (after storage time  $t_{storage}$ ), and the leaked pulse (a fraction of the input pulse that leaks through the medium, i.e. that is not stored in the medium). Measured efficiency is 20.5 %, the best efficiency measured for our QM system. Adapted from [79].

Input probe pulse is presented in green color in the figure. This is a reference probe pulse measured with the filtering cavity being locked to the  $-1$  sideband. Pink color presents the trace of the output pulse, measured when the filtering cavity is locked to  $+1$  sideband, i.e. in the EIT conditions. In the first part of the trace, we see a leaked pulse from the medium. Pulse leakage is a consequence of sub-optimal experimental conditions in the system. Input pulse is stored in the medium for  $1\text{ }\mu\text{s}$  in this example. The output pulse is released after the storage time by switching

on the control beam. An important property of quantum memory is the efficiency of pulse retrieval. It is defined as the ratio between the trace area under the output pulse and the trace area under the input pulse [22]. In Fig. 5.16 we present our best achieved efficiency of 20.5 %. It has been achieved for the EIT linewidth of 100 kHz, at  $T = 55^\circ\text{C}$ . Optimization procedure has been performed, following the procedure described in [64], to achieve the optimal efficiency. In simple terms, the shape of the probe pulse is optimized using an iterative procedure. The initial probe pulse is of an arbitrary shape (usually a half gaussian shape). Generally, we use a pulse with a half-gaussian profile. From this first input pulse, we take the shape of the output pulse and shape the next iteration of the input pulse to match the output pulse profile. Doing this procedure several times, we quickly converge to the condition where input and output pulses have the same shape, which is also a condition when the QM efficiency is maximum.

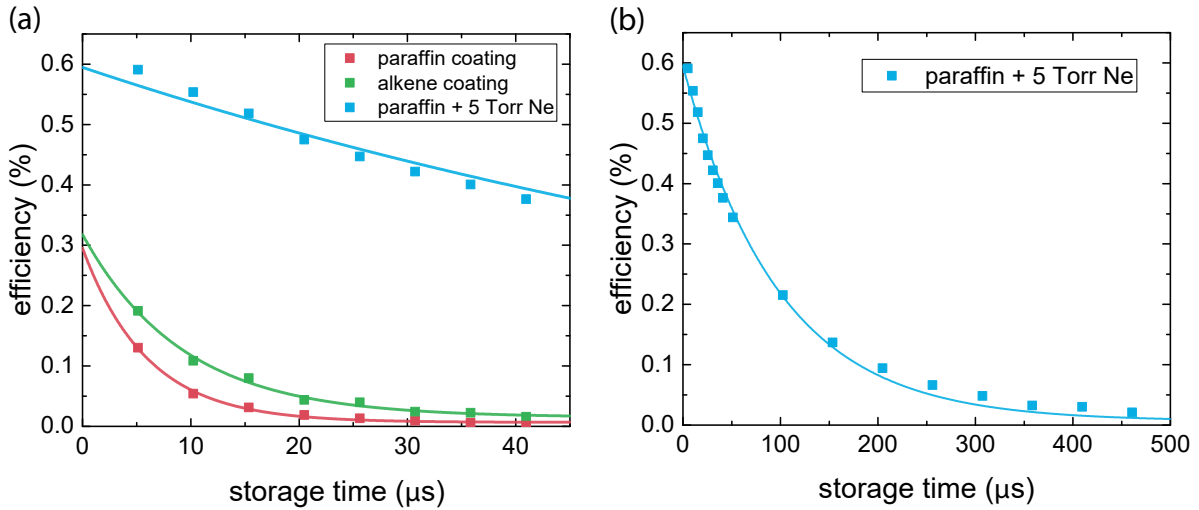


Figure 5.17: Quantum memory efficiency as a function of storage time (left panel). Different glass cells have different maximum storage times due to the different ground state decoherence rates. Exponential parameter that characterizes the decay of the QM efficiency is obtained by fitting the exponential decay function to the measured data. Decay parameters: paraffin coated cell:  $(6.0 \pm 0.5) \mu\text{s}$ , alkene coated cell:  $(9.3 \pm 0.9) \mu\text{s}$ , paraffin coated cell with 5 Torr of Ne:  $(98 \pm 4) \mu\text{s}$ . The right panel shows the measurement for the paraffin coated cell with 5 Torr of Ne for longer storage times.

We measured the QM efficiency as a function of storage time at room temperature for our three glass cells with different ground state decoherence rates. The results are presented in Fig. 5.17. Measurement conditions are  $T = 22^\circ\text{C}$  and EIT linewidth of 100 kHz for all cells. QM efficiency decreases exponentially as the storage time is increased, which is a consequence of the exponential decay of the ground state coherence. There is a big difference in maximum achievable storage time between the cells, as expected from the ground state decoherence mea-

measurements, Fig. 5.13. Longest storage times are achieved in the paraffin cell with 5 Torr of neon buffer gas, as is expected. In this measurement the lowest measurable efficiency is limited by the signal-to-noise ratio, and the longest storage time of about  $460 \mu\text{s}$  was measured. QM is characterized by the exponential decay parameter, which we obtained by fitting the data to the exponential decay function. For our three cells of interest, they are  $(6.0 \pm 0.5) \mu\text{s}$  for paraffin coated cell,  $(9.3 \pm 0.9) \mu\text{s}$  for alkene coated cell, and  $(98 \pm 4) \mu\text{s}$  for paraffin coated cell with 5 Torr of Ne.

The efficiency of our memory is quite low due to the very low optical depth at room temperature. From theory, we expect that the QM efficiency rises with the increase of the optical depth (OD). In the experiment, by increasing the OD by heating the glass cell, and thus increasing the Rb concentration, we achieved higher efficiency of the memory, while the decay parameter stays the same. An example of the measurement at  $55^\circ\text{C}$  is presented in Fig. 5.16, while the measurements presented in Fig. 5.17 are performed at room temperature.

From here on, we will work only with the vapor cell with Paraffin coating and 5 Torr of neon buffer gas, since it is performing best out of the three cells. In order to maximize the QM parameters, we conducted a series of measurements where we changed the parameters of the input pulse. In Fig. 5.18 we present results of the QM decay parameter for different shapes of the input pulse. We shaped the input pulse using QRF while keeping the pulse FWHM and area constant. Fig. 5.18(a) presents six different pulse shapes we used in measurements. As expected, the QM decay parameter does not change for different input pulse shapes. On the other hand, QM efficiency does change when different input pulse shapes are used (see top panel of Fig. 5.18(b)). For this particular pulse area and pulse FWHM, the best efficiency of around 0.75 % is achieved for triangle, square and half gaussian pulses, followed by the 3/4 gaussian pulse with 0.64 %, exponential pulse with 0.55 %, and full gaussian pulse with efficiency of 0.24 %. In general, changing the pulse area and FWHM of input pulses changes the QM efficiency, whereas the QM decay parameter remains constant. As already mentioned, an input pulse optimization algorithm can be used to maximize the QM efficiency [64].

Another way of increasing the QM efficiency is by increasing the temperature of the vapor cell, i.e. by increasing the Rb atom concentration. Indeed, for a fixed pulse shape, there is an optimal temperature where efficiency is maximum. For an exponential pulse of  $6.1 \mu\text{s}$  FWHM and the EIT width of 100 kHz, the best efficiency of around 2 % is achieved at  $41.2^\circ\text{C}$ . Efficiency is also highly affected by the EIT contrast as the input pulse is partially absorbed by the medium. Absorption of the input pulse can be reduced by detuning the probe and control beam from the atomic resonance. In Fig. 5.19 we present EIT signals and QM efficiency for resonant and off-resonant excitation. We present three cases, resonant EIT with the probe and the con-

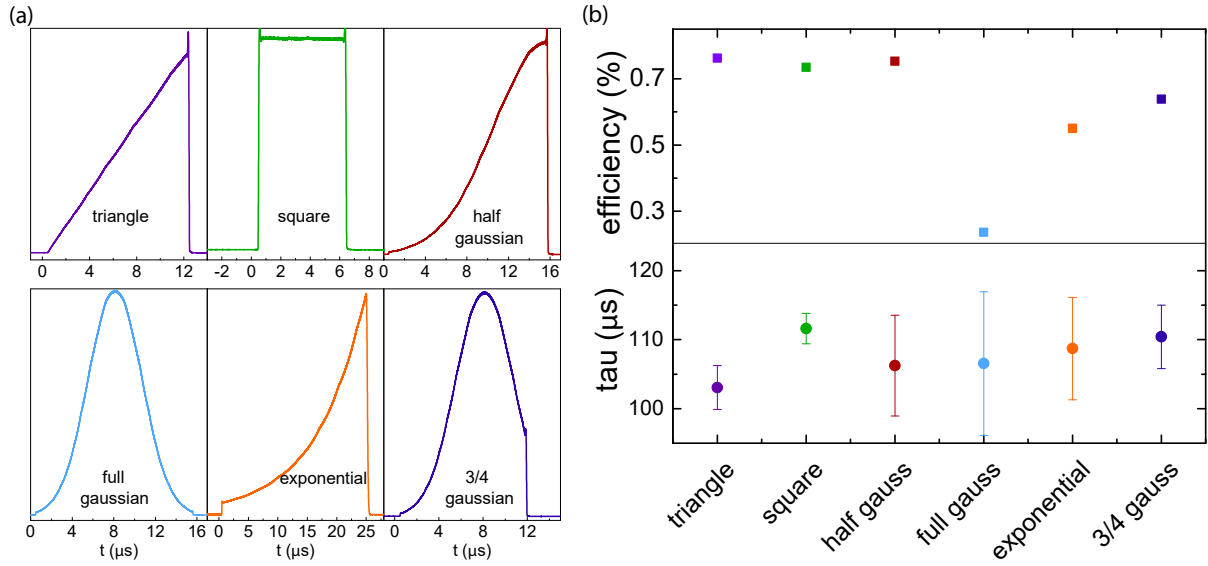


Figure 5.18: QM efficiency (top) and decay parameter (bottom) (b) measured for different input pulse shapes (a).

trol beam being resonant with  $|F = 2\rangle \rightarrow |F' = 3\rangle$  and  $|F = 3\rangle \rightarrow |F' = 3\rangle$  transitions, the case where the probe and the control beams are 500 MHz blue detuned from these transitions and when beams are 500 MHz red detuned from transitions. The EIT signal for off-resonant excitation can be described using the generalized Lorentzian function [80], but its transparency window is still achieved when the two-photon detuning of the probe and the control beam is satisfied. From Fig. 5.19 (b) we see that the efficiency is larger for blue detuned beams than for the red detuned beams, which is a consequence of lower absorption for blue detuned beams.

We optimized the input pulse shape efficiency for the blue detuned case, following the procedure described in [64]. This is presented in Fig. 5.19(b), with open red squares. As we can see by changing the input pulse from an arbitrary shape (solid squares, half gaussian pulse with  $5.3 \mu\text{s}$  FWHM), we maximized the QM efficiency, while keeping the QM decay parameter constant. The optimized input pulse is the exponential pulse with the FWHM of  $2.5 \mu\text{s}$ . The efficiency for the initial pulse shape is around 8 %, and for the optimized pulse shape is around 13 %.

We have achieved even higher QM efficiency of 20.5 % as presented in Fig. 5.16. In this case we tuned the temperature to  $55^\circ\text{C}$ , optimized the input pulse and adjusted the probe and control frequencies 580 MHz blue detuned from  $|F = 2\rangle \rightarrow |F' = 3\rangle$  and  $|F = 3\rangle \rightarrow |F' = 3\rangle$  transitions. For these parameters, we measured up to 1.2 ms of storage time, which is our best achieved efficiency and storage time in this experiment.

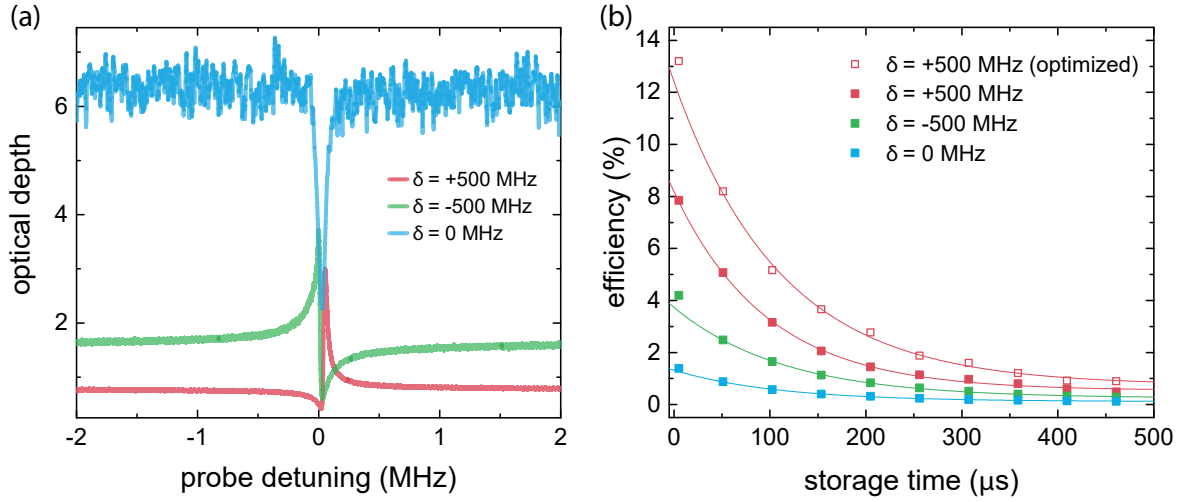


Figure 5.19: (a) EIT signal for resonant and offresonant excitation at elevated temperature of  $41.2^\circ$  C. (b) QM efficiency for resonant and offresonant excitation, and optimized input pulse shape. EIT width is 100 kHz. Data for resonant excitation is smoothed due to high optical depth in EIT wings (division of two near zero numbers).

## 5.5 Conclusion

We have demonstrated the electromagnetically induced transparency effect in the Rb vapor. We measured the EIT width for the vapor cell without coating and filling, and three different vapor cells with different coatings and filling, to characterize the ground state decoherence rate. Measured ground state decoherence rates are:

$$\gamma_{12} = (16.0 \pm 0.4) \text{ kHz} \quad \text{for} \quad \text{Paraffin coating} \quad (5.16a)$$

$$\gamma_{12} = (8.0 \pm 0.5) \text{ kHz} \quad \text{for} \quad \text{Alkene coating} \quad (5.16b)$$

$$\gamma_{12} = (0.74 \pm 0.08) \text{ kHz} \quad \text{for} \quad \text{Paraffin coating with 5 Torr Ne} \quad (5.16c)$$

Based on the analysis of different contributions to the ground state decoherence rate, we conclude that the main limitation to the ground state coherence for the paraffin and alkene coated cells is transit-time broadening, while for the cell with paraffin coating and 5 Torr Ne buffer gas the main limitation comes from transit-time broadening and residual Doppler broadening. Transit-time broadening and residual Doppler broadening reduce the EIT contrast, together with the existence of another excited state that is absorbing parts of the control and probe beams.

We have measured and characterized the EIT and QM using the alkene-coated Rb vapor cell. As predicted [66], this cell outperforms the paraffin coated cell when EIT width and QM storage time is considered.

We have demonstrated up to 1.2 ms QM storage times in Rb atomic vapor. The storage time is directly related to the ground state decoherence rate, hence the largest storage time is obtained for the paraffin coated cell with buffer gas.

We demonstrated that the QM decay parameter is independent of the input parameters, as opposed to the QM efficiency. QM efficiency increases as temperature (i.e. Rb atoms concentration) is increased, as well as the detuning of the probe and control beams (while still fulfilling the EIT condition). The best achieved quantum memory efficiency in this experiment is 20.5 %.

We believe that these results presented in this work could help in the design and implementation of new quantum memories that will be used as parts of the quantum repeaters in quantum communications.

# Chapter 6

## Thesis summary

In the thesis, I presented the results of my research at the Institute of physics. During my doctoral research, I was a member of the Quantum technology group from the institute. The main research of the group is based on the laser cooling and trapping of rubidium atoms and the frequency comb interaction with cold atoms. Recently, groups' focus expanded to the precision measurements and optical atomic clocks based on the strontium atoms, and the research in the field of quantum communications, i.e. the research of the quantum memories in rubidium vapor.

I presented the results of the theoretical model that describes the interaction of two counter-propagating pulse trains with six-level atoms in 1D. The process of the frequency comb laser cooling is very sensitive to the comb parameters, repetition frequency, and offset frequency. We presented three sets of comb parameters that are presenting three different cases of the atom-comb interaction. The first case is the case of optimal laser cooling with a frequency comb, where one comb mode interacts with the cooling transition and the other with the repumping transition. The temperature of atoms for interaction with these comb parameters is close to the Doppler temperature as is expected. The other two sets of comb parameters are not optimal for laser cooling. In one case comb interaction lead to the optical pumping of the atomic population into the dark state for the mode responsible for cooling. In the last case, only one comb mode interacted with atoms so the population is partially lost from the cooling cycle. This model can be used for any other atom with a similar energy level structure.

In the experiment, the choice of frequency comb parameters is very limited. FC source I used was tuned to the repetition frequency of 80.495 MHz. This repetition frequency enables us to simultaneously cool two rubidium isotopes,  $^{85}\text{Rb}$  and  $^{87}\text{Rb}$ . We developed a two isotope magneto-optical trap, where we loaded clouds of two Rb isotopes simultaneously using continuous-wave lasers. We measured simultaneous the radiation pressure force exerted on two Rb isotopes. By tuning the FC parameters, we successfully demonstrated simultaneous cooling

of two atomic species using a single frequency comb source. The measured temperatures are Doppler limited due to the low power per comb mode of our laser source. To the best of our knowledge, this is the first demonstration of simultaneous cooling using a frequency comb laser.

Finally, I presented the results of the quantum memory experiment. We have demonstrated that different glass cell coatings and fillings have different ground state decoherence rates, which is the limiting factor for the quantum memory efficiency and storage time. The lowest measured decoherence rate was for the cell with the paraffin coating filled with 5 Torr of neon buffer gas. We demonstrated that the lower decoherence rate enables a longer storage time for the probe pulses. By increasing the temperature of vapor, and exciting the EIT of-resonant, we achieved a quantum memory with efficiency up to 20.5 %, and storage time of 1.2 ms.

# References

- [1] A. L. Schawlow and C. H. Townes. Infrared and Optical Masers. *Phys. Rev.*, 112:1940, Dec 1958.
- [2] A. D. Cronin, J. Schmiedmayer, and D. E. Pritchard. Optics and interferometry with atoms and molecules. *Rev. Mod. Phys.*, 81:1051, Jul 2009.
- [3] B. J. Bloom, T. L. Nicholson, J. R. Williams, S. L. Campbell, M. Bishof, X. Zhang, W. Zhang, S. L. Bromley, and J. Ye. An optical lattice clock with accuracy and stability at the  $10^{-18}$  level. *Nature*, 506:71–75, Jan 2014.
- [4] S. Ospelkaus, K.-K. Ni, D. Wang, M. H. G. de Miranda, B. Neyenhuis, G. Quémener, P. S. Julienne, J. L. Bohn, D. S. Jin, and J. Ye. Quantum-State Controlled Chemical Reactions of Ultracold Potassium-Rubidium Molecules. *Science*, 327:853–857, Feb 2010.
- [5] F Schäfer, T. Fukuhara, S. Sugawa, Y. Takasu, and Y. Takahashi. Tools for quantum simulation with ultracold atoms in optical lattices. *Nat. Rev. Phys.*, 2:411–425, Jul 2020.
- [6] J. J. McClelland, A. V. Steele, B. Knuffman, K. A. Twedt, A. Schwarzkopf, and T. M. Wilson. Bright focused ion beam sources based on laser-cooled atoms. *Applied Physics Reviews*, 3:011302, Mar 2016.
- [7] N. Šantić. Synthetic Lorentz force for neutral cold atoms, 2018. PhD thesis, University of Zagreb.
- [8] J. Ye, H. Schnatz, and L. W. Hollberg. Optical frequency combs: from frequency metrology to optical phase control. *IEEE J. Sel. Top. Quantum Electron*, 9:1041, Dec 2003.
- [9] B.G. Whitford. Phase-locked frequency chains to 130 thz at nrc. In A. De Marchi, editor, *Frequency Standards and Metrology*, pages 187–190. Springer, Berlin, Heidelberg, 1989.
- [10] J. L. Hall and T. W. Hänsch. The Nobel prize in physics 2005. <https://www.nobelprize.org/prizes/physics/2005/summary/>.
- [11] D. Kielpinski. Laser cooling of atoms and molecules with ultrafast pulses. *Phys. Rev. A*, 73:063407, Jun 2006.
- [12] J. Davila-Rodriguez, A. Ozawa, T. W. Hänsch, and T. Udem. Doppler Cooling Trapped Ions with a UV Frequency Comb. *Phys. Rev. Lett.*, 116:043002, Jan 2016.
- [13] M. Ip, A. Ransford, A. M. Jayich, X. Long, C. Roman, and W. C. Campbell. Phonon Lasing from Optical Frequency Comb Illumination of Trapped Ions. *Phys. Rev. Lett.*, 121:043201, Jul 2018.
- [14] N. B. Vilas, C. Hallas, L. Anderegg, P. Robichaud, A. Winnicki, D. Mitra, and J. M. Doyle. Magneto-optical trapping and sub-Doppler cooling of a polyatomic molecule. *Nature*, 606:70–74, Jun 2022.
- [15] D. Aumiler and T. Ban. Simultaneous laser cooling of multiple atomic species using an optical frequency comb. *Phys. Rev. A*, 85:063412, Jun 2012.
- [16] A. Bonnin, C. Diboune, N. Zahzam, Y. Bidel, M. Cadoret, and A. Bresson. New concepts of inertial measurements with multi-species atom interferometry. *Appl. Phys. B*, 124:181, Aug 2018.
- [17] J. Williams, S.-w. Chiow, N. Yu, and Müller. H. Quantum test of the equivalence principle and space-time aboard the International Space Station. *New J. Phys.*, 18:025018, Feb 2016.
- [18] L. D. Carr, D. DeMille, R. V. Krems, and J. Ye. Cold and ultracold molecules: science, technology and applications. *New J. Phys.*, 11:055049, May 2009.
- [19] G. Modugno, M. Modugno, F. Riboli, G. Roati, and Inguscio M. Two Atomic Species Superfluid. *Phys. Rev. Lett.*, 89:190404, Oct 2002.

- [20] H.-J. Briegel, W. Dür, J. I. Cirac, and P. Zoller. Quantum Repeaters: The Role of Imperfect Local Operations in Quantum Communication. *Phys. Rev. Lett.*, 81:5932, Dec 1998.
- [21] M. Żukowski, A. Zeilinger, M. A. Horne, and A. K. Ekert. Event-ready-detectors Bell experiment via entanglement swapping. *Phys. Rev. Lett.*, 71:4287, Dec 1993.
- [22] I. Novikova, R. L. Walsworth, and Y. Xiao. Electromagnetically induced transparency-based slow and stored light in warm atoms. *Laser & Photon. Rev.*, 6:333–353, May 2012.
- [23] Y. O. Dudin, L. Li, and A. Kuzmich. Light storage on the time scale of a minute. *Phys. Rev. A*, 87:031801(R), Mar 2013.
- [24] D.G. England, K. A. G. Fisher, J.-P. W. MacLean, P. J. Bustard, R. Lausten, K. J. Resch, and B. J. Sussman. Storage and Retrieval of THz-Bandwidth Single Photons Using a Room-Temperature Diamond Quantum Memory. *Phys. Rev. Lett.*, 114:053602, Feb 2015.
- [25] M. Hosseini, B. M. Sparkes, G. Campbell, P. K. Lam, and B. C. Buchler. High efficiency coherent optical memory with warm rubidium vapour. *Nat. Comm.*, 2:174, Feb 2011.
- [26] K. F. Reim, P. Michelberger, K. C. Lee, J. Nunn, N. K. Langford, and I. A. Walmsley. Single-Photon-Level Quantum Memory at Room Temperature. *Phys. Rev. Lett.*, 107:053603, Jul 2011.
- [27] D. Main, S. Hird, T. M. and Gao, I. A. Walmsley, and P. M. Ledingham. Room temperature atomic frequency comb storage for light. *Opt. Lett.*, 46:2960–2963, Jun 2021.
- [28] P. Jobez, C. Laplane, N. Timoney, N. Gisin, A. Ferrier, P. Goldner, and M. Afzelius. Coherent Spin Control at the Quantum Level in an Ensemble-Based Optical Memory. *Phys. Rev. Lett.*, 114:230502, Jun 2015.
- [29] O. Katz and O. Fistenberg. Light storage for one second in room-temperature alkali vapor. *Nat. Comm.*, 9:2074, May 2018.
- [30] M. Fleischhauer, A. Imamoglu, and J. P. Marangos. Electromagnetically induced transparency: Optics in coherent media. *Rev. Mod. Phys.*, 77:633, Jul 2005.
- [31] K.-J. Boller, A. Imamoglu, and S. E. Harris. Observation of electromagnetically induced transparency. *Phys. Rev. Lett.*, 66:2593, May 1991.
- [32] K. DeRose, K. Jiang, J. Li, L. Zhuo, H. Cai, and S. Bali. Producing slow light in warm alkali vapor using electromagnetically induced transparency. <https://arxiv.org/abs/2011.09229>.
- [33] H. J. Metcalf and P. van der Straten. *Laser Cooling and Trapping*. Springer, New York, 1999.
- [34] H. Perrin. Lecture 1, Light forces , 2012. Les Houches lectures on laser cooling and trapping, [http://www-lpl.univ-paris13.fr/bec/bec/Teaching/lecture1\\_2012.pdf](http://www-lpl.univ-paris13.fr/bec/bec/Teaching/lecture1_2012.pdf).
- [35] H. Perrin. Lecture 2, Doppler cooling and magneto-optical trapping, 2012. Les Houches lectures on laser cooling and trapping, [http://www-lpl.univ-paris13.fr/bec/bec/Teaching/lecture2\\_2012.pdf](http://www-lpl.univ-paris13.fr/bec/bec/Teaching/lecture2_2012.pdf).
- [36] M. Wollenhaupt, A. Assion, and T. Baumert. Short and ultrashort laser pulses. In F. Träger, editor, *Springer Handbook of Lasers and Optics*, chapter 12, pages 1047–1094. Springer, New York, 2007.
- [37] D. Aumiler. Resonant interaction of atoms and molecules with the femtosecond frequency comb, 2006. PhD thesis, University of Zagreb.
- [38] D. A. Steck. Rubidium 85 D Line Data. Available online at <http://steck.us/alkalidata> (revision 2.2.3, 9 July 2021).
- [39] D. A. Steck. Rubidium 87 D Line Data. Available online at <http://steck.us/alkalidata> (revision 2.2.2, 9 July 2021).
- [40] P. D. Lett, R. N. Watts, C. I. Westbrook, W. D. Phillips, P. L. Gould, and H. J. Metcalf. Observation of Atoms Laser Cooled below the Doppler Limit. *Phys. Rev. Lett.*, 61:169–173, Jul 1988.
- [41] J. Dalibard and C. Cohen-Tannoudji. Laser cooling below the Doppler limit by polarization gradients: simple theoretical models. *J. Opt. Soc. Am. B*, 6:2023–2045, Nov 1989.
- [42] E. L. Raab, M. Prentiss, A. Cable, S. Chu, and D. E. Pritchard. Trapping of Neutral Sodium Atoms with Radiation Pressure. *Phys. Rev. Lett.*, 59:2631–2634, Dec 1987.
- [43] J.-C. Diels and W. Rudolph. *Ultrashort Laser Pulse Phenomena*. Academic Press, San Diego, 2006.

- [44] J. Ye and S. T. Cundiff. *Femtosecond Optical Frequency Comb: Principle, Operation and Applications*. Springer, New York, 2005.
- [45] N. Šantić, D. Buhin, D. Kovačić, I. Krešić, D. Aumiler, and T. Ban. Cooling of atoms using an optical frequency comb. *Sci. Rep.*, 9:2510, Feb 2019.
- [46] A. M. Jayich, X. Long, and W. C. Campbell. Direct Frequency Comb Laser Cooling and Trapping. *Phys. Rev. X*, 6:041004, Oct 2016.
- [47] E. Ilinova, M. Ahmad, and A. Derevianko. Doppler cooling with coherent trains of laser pulses and a tunable velocity comb. *Phys. Rev. A*, 84:033421, Sep 2011.
- [48] D. Felinto, C. A. C. Bosco, L. H. Acioli, and S. S. Vianna. Coherent accumulation in two-level atoms excited by a train of ultrashort pulses. *Opt. Comm.*, 215:69–73, Jan 2003.
- [49] T. Ban, D. Aumiler, H. Skenderović, and G. Pichler. Mapping of the optical frequency comb to the atom-velocity comb. *Phys. Rev. A*, 73:043407, Apr 2006.
- [50] B. B. Blinov, R. N. Kohn Jr., M. J. Madsen, P. Maunz, D. L. Moehring, and C. Monroe. Broadband laser cooling of trapped atoms with ultrafast pulses. *J. Opt. Soc. Am. B*, 23:1170–1173, Jun 2006.
- [51] C. P. Pearman, C. S. Adams, S. G. Cox, P. F. Griffin, D. A. Smith, and I. G. Hughes. Polarization spectroscopy of a closed atomic transition: applications to laser frequency locking. *J. Phys. B: At. Mol. Opt. Phys.*, 35:5141–5151, Dec 2002.
- [52] G. Hadley. Injection locking of diode lasers. *IEEE Journal of Quantum Electronics*, 22(3):419–426, Mar 1986.
- [53] C. J. H. Pagett, P. H. Moriya, R. Celistrino Teixeira, R. F. Shiozaki, M. Hemmerling, and Ph. W. Courteille. Injection locking of a low cost high power laser diode at 461 nm. *Rev. Sci. Instrum.*, 87:053105, May 2016.
- [54] M. Hofer, M. E. Fermann, F. Haberl, M. H. Ober, and A. J. Schmidt. Mode locking with cross-phase and self-phase modulation. *Opt. Lett.*, 16:502–504, Apr 1991.
- [55] H. A. Haus, E. P. Ippen, and K. Tamura. Additive-pulse modelocking in fiber lasers. *IEEE Journal of Quantum Electronics*, 30:200–208, Jan 1994.
- [56] H. R. Telle, G. Steinmeyer, A. E. Dunlop, J. Stenger, D. H. Sutter, and U. Keller. Carrier-envelope offset phase control: A novel concept for absolute optical frequency measurement and ultrashort pulse generation. *App. Phys. B*, 69:327–332, Sep 1999.
- [57] D. Buhin. Femtosecond laser optomechanics in cold atoms, 2017. Master’s thesis, University of Zagreb.
- [58] D. Buhin, D. Kovačić, F. Schmid, M. Kruljac, V. Vulić, T. Ban, and Aumiler D. Simultaneous dual-species laser cooling using an optical frequency comb. *Phys. Rev. A*, 102:021101(R), Aug 2020.
- [59] W. Süptitz, G. Wokurka, F. Strauch, P. Kohns, and W. Ertmer. Simultaneous cooling and trapping of  $^{85}\text{Rb}$  and  $^{87}\text{Rb}$  in a magneto-optical trap. *Opt. Lett.*, 19:1571–1573, Oct 1994.
- [60] T. M. Brzozowski, M. Maczynska, M. Zawada, J. Zachorowski, and W. Gawlik. Time-of-flight measurement of the temperature of cold atoms for short trap-probe beam distances. *J. Opt. B: Quantum Semiclass. Opt.*, 4:62, Jan 2002.
- [61] I. Yavin, M. Weel, A. Andreyuk, and A. Kumarakrishnan. A calculation of the time-of-flight distribution of trapped atoms. *Am. J. Phys.*, 70:149, Jan 2002.
- [62] M. Kruljac, D. Buhin, D. Kovačić, V. Vulić, D. Aumiler, and T. Ban. Frequency-comb-induced radiation pressure force in dense atomic clouds. *JOSA B*, 39:1411–1418, Apr 2022.
- [63] J. Dalibard and Y. Castin. Laser cooling from the semi-classical to the quantum regime. <https://pro.college-de-france.fr/jean.dalibard/publi2/varenna1992.pdf>.
- [64] N. B. Phillips, A. V. Gorshkov, and I. Novikova. Optimal light storage in atomic vapor. *Phys. Rev. A*, 78:023801, Aug 2008.
- [65] Y.-W. Cho, G. T. Campbell, J. L. Everett, J. Bernu, D. B. Higginbottom, M. T. Cao, J. Geng, N. P. Robins, P. K. Lam, and B. C. Buchler. Highly efficient optical quantum memory with long coherence time in cold atoms. *Optica*, 3:100–107, Jan 2016.
- [66] M. Lijun, O. Slattery, and X. Tang. Optical quantum memory based on electromagnetically induced transparency. *J. Opt.*, 19:043001, Feb 2017.

- [67] A. Kasapi, Maneesh Jain, G. Y. Yin, and S. E. Harris. Electromagnetically Induced Transparency: Propagation Dynamics. *Phys. Rev. Lett.*, 74:2447, Mar 1995.
- [68] M. Kruljac. Coherent effects in a cold atomic gas, 2018. Master's thesis, University of Zagreb.
- [69] P. W. Milonni and J. H. Eberly. *Laser Physics*. Wiley, New Jersey, 2010.
- [70] M. D. Lukin, M. Fleischhauer, A. S. Zibrov, H. G. Robinson, V. L. Velichansky, L. Hollberg, and M. O. Scully. Spectroscopy in Dense Coherent Media: Line Narrowing and Interference Effects. *Phys. Rev. Lett.*, 79:2959, Oct 1997.
- [71] M. Fleischhauer and M. D. Lukin. Quantum memory for photons: Dark-state polaritons. *Phys. Rev. A*, 65:022314, Jan 2002.
- [72] W. Nagourney. *Quantum Electronics for Atomic Physics and Telecommunication: Second Edition*. Oxford University Press, New York, 2014.
- [73] K. DeRose. Observation of slow light, stored light, and Dicke narrowing in warm alkali vapor, 2019. PhD thesis, Miami University.
- [74] E. Arimondo. Relaxation processes in coherent-population trapping. *Phys. Rev. A*, 54:2216, Sep 1996.
- [75] M. Klein, M. Hohensee, Y. Xiao, R. Kalra, D. F. Phillips, and R. L. Walsworth. Slow-light dynamics from electromagnetically-induced-transparency spectra. *Phys. Rev. A*, 79:053833, May 2009.
- [76] M. Klein, M. Hohensee, D. F. Phillips, and R. L. Walsworth. Electromagnetically induced transparency in paraffin-coated vapor cells. *Phys. Rev. A*, 83:013826, Jan 2011.
- [77] M. V. Balabas, T. Karaivanov, M. P. Ledbetter, and D. Budker. Polarized Alkali-Metal Vapor with Minute-Long Transverse Spin-Relaxation Time. *Phys. Rev. Lett.*, 105:070801, Aug 2010.
- [78] T. Pakasin. Automation of data acquisition in the laboratory, 2022. Master's thesis, University of Zagreb.
- [79] M. Đujić. Effects of decoherence on the properties of optical quantum memories, 2022. Master's thesis, University of Zagreb.
- [80] R. Finkelstein, S. Bali, O. Firstenberg, and I. Novikova. A practical guide to electromagnetically induced transparency in atomic vapor. <https://arxiv.org/pdf/2205.10959.pdf>.
- [81] J. Vanier, A. Godone, and F. Levi. Coherent population trapping in cesium: Dark lines and coherent microwave emission. *Phys. Rev. A*, 58:2345, Sep 1998.

# Curriculum vitae

Danijel Buhin was born in Varaždin, Croatia on the 31st of August, 1993. From 2008.-2012. he attended First Gymnasium in Varaždin. In 2012. he enrolled integrated undergraduate and graduate study of physics at the Faculty of Science in Zagreb, Croatia. He graduated in 2017, with a master's degree thesis titled "Femtosecond laser optomechanics in cold atoms", under the supervision of dr. sc. Ticijana Ban. As of 2017 he is employed at the Institute of Physics as an assistant. In the same year, he enrolled in a doctoral study of Atomic, molecular and optical physics at the Faculty of Science in Zagreb. During his doctoral study, he was a teaching assistant at the faculty for Physics lab 1 and 2 courses.

## Refereed publications

### Published

- 3 Kruljac, M., **Buhin, D.**, Kovačić, D., Vulić, V., Aumiler, D., Ban, T., *Frequency-comb-induced radiation pressure force in dense atomic clouds.*, JOSA B 39, 1411-1418 (2022), <https://doi.org/10.1364/JOSAB.449798>
- 2 **Buhin, D.**, Kovačić, D, Schmid, F., Kruljac, M., Vulić, V., Ban, T., Aumiler, D., *Simultaneous dual-species laser cooling using an optical frequency comb.*, Phys. Rev. A 102, 021101(R) (2020). <https://doi.org/10.1103/PhysRevA.102.021101>
- 1 Šantić, N., **Buhin, D.**, Kovačić, D., Krešić I., Aumiler, D., Ban, T., *Cooling of atoms using an optical frequency comb.* Sci Rep 9, 2510 (2019). <https://doi.org/10.1038/s41598-018-38319-3>